DIE BONDING OF DIODE LASERS

By

MARK A. FRITZ, B.Eng. Mgmt.

A Thesis

Submitted to the School of Graduate Studies

in Partial Fulfilment of the Requirements

for the Degree

Doctor of Philosophy

McMaster University

© Copyright by Mark A. Fritz, 2004

DOCTOR OF PHILOSOPHY (2004)
(Engineering Physics)

McMaster University
Hamilton, Ontario

TITLE: Die Bonding of Diode Lasers

AUTHOR: Mark A. Fritz, B.Eng.Mgmt. (McMaster University)

SUPERVISOR: Professor Daniel T. Cassidy

NUMBER OF PAGES: xii, 129

ABSTRACT

An examination of the die bonding of semiconductor diode lasers is presented. The effects of changing a number of bonding parameters such as reflow time, reflow temperature, and cooling rate on InP-based diode laser chips are investigated. Lasers bonded with both preform solder and pre-deposited solder are explored. It is also observed that stress relaxation occurs in die bonds of diode lasers after a time period of hundreds of hours.

A finite element method model that iteratively fits to degree of polarization of photoluminescence data is presented. It is shown how this model is used to determine components of stress and strain owing to die bonding at the facet of diode lasers. The model is shown to be capable of helping to characterize die bonds.

The effect of die bonding induced strain on the spectra of distributed feedback diode lasers is also investigated. Bonding strain affects the *in situ* grating in distributed feedback lasers which manifests as changes in the modes of the output spectrum and the stopband width. As well, it is observed that the lasing mode can flip from one side of the stopband to the other upon bonding and this effect is successfully modelled using a DFB laser model.

ACKNOWLEDGEMENTS

I would like to thank first of all Dr. Daniel T. Cassidy, who has been my professor at McMaster for a number of years and has provided me with expert technical guidance throughout. You are an excellent supervisor and you have shown that you believe in your students and have always held the highest standards of professionalism in your work. I have benefited greatly from working with you and I hope to collaborate with you in the future. I would also like to thank the other members of my supervisory committee, Dr. Paul Jessop and Dr. Peter Mascher, for taking the time with this thesis and for being great professors during my long time in the Department. In addition, Dr. Spencer Smith from the Department of Computing and Software was giving of his time in helping me develop my understanding of the finite element method. Dr. Gord Morrison was very helpful to me in the work of Chapter 9.

The work in this thesis would not have been possible without the help of my fellow student Samuel Lam, with whom I have shared the lab since being in graduate school. We have had many important discussions that have helped both of us along the way. Dr. Doug Bruce has also helped me out in many ways and it has been a pleasure getting to know you. There is a long list of friends and acquaintances who have made my stay at McMaster enjoyable. Although not exhaustive, it would include: Andrzej Borowiec, Sean Woodworth, Josej Czaban, David DeForge, Philip Waldron, Aaron Vandermeer, Edward Irving, Huiling Wang, and Jingcong Wang. I wish to thank Dr. Michael Hamp for letting me stay at his place in Ottawa for several months and for originating *Feynman Night.*

I would also like to acknowledge some members of the staff in the Department with whom I have enjoyed chatting over the years: Glen Leinweber, Fran Allen, Tina Stewart, and Elvira Evangelista. I believe that Glen has contributed significantly to my understanding of a whole range of issues and I thank you for it.

My parents deserve a tip of the hat too for their unwavering support of me. To this list I would like to add my sister and her family as well as my in-laws. My dog Missy has kept me healthy with thrice-daily walks and, despite her manic personality, has had an important calming effect during stressful Ph.D. work.

Lastly I wish to thank my beautiful wife, Jana, who has provided me with a wonderful life. You let me quit a good job and return to school to learn some more because you knew that is what I wanted. You also allowed me to lead a relatively normal life whilst being a student, including some memorable trips. I love you and thank you.

TABLE OF CONTENTS

CHAPTER 1 - INTRODUCTION 1

CHAPTER 2 - STRAIN MEASUREMENT IN DIODE LASERS

2.1 Introduction 5
2.2 General Elasticity 5
2.3 Degree of Polarization of Photoluminescence 7
2.4 DOP Apparatus 9
2.5 Summary 12

CHAPTER 3 - DIODE LASER BONDING

3.1 Introduction 13
3.2 Die Bonding 13
3.3 Adhesion 14
3.4 Solder Bonding 16
3.4.1 Wetting 16
3.4.2 Alloy Selection 16
3.4.3 Solder Forms 19
3.4.4 Metallizations 19
3.4.5 Chip Carriers and Sub-Mounts 21
3.5 Epoxy Bonding 21
3.6 Materials 22
3.7 Summary 24

CHAPTER 4 - COOLING RATE IN DIODE LASER DIE BONDS

4.1 Introduction 25
4.2 Experiment 25
4.2.1 Strain 27
4.2.2 Thermal Impedance 28
4.2.3 Surface Structure 29
4.2.4 Cross Sectional Structure 29
4.2.5 Cross Sectional Composition 30
4.2.6 Bond Strength 30
4.3 Results 30
4.3.1 Strain 30
4.3.2 Thermal Impedance 32
4.3.3 Surface Structure 33
4.3.4 Cross Sectional Structure 34
4.3.5 Cross Sectional Composition 35
4.3.6 Bond Strength 36
4.4 Discussion 37
4.5 Summary 39

CHAPTER 5 - PRE-DEPOSITED SOLDER

5.1 Introduction 41
5.2 Reflow Time and Temperature 41

5.2.1 Experiment 41
5.2.2 Results 45
5.2.3 Discussion 49
5.3 Carrier Metallization 51
5.3.1 Experiment 51
5.3.2 Results 52
5.3.3 Discussion 54
5.4 Summary 54

CHAPTER 6 - STRESS RELAXATION IN DIE BONDS

6.1 Introduction 55
6.2 Procedure 55
6.3 Results 55
6.4 Discussion 59
6.5 Summary 54

CHAPTER 7 - FINITE ELEMENT METHOD FITTING

7.1 Introduction 63
7.2 Motivation for FEM Code 63
7.3 Finite Element Method 64
7.3.1 Overview 64
7.3.2 Elasticity Problems 65
7.3.3 Meshing 65
7.3.4 Interpolation Functions 66
7.3.5 Minimum Potential Energy Principle 69
7.3.6 Convergence 72
7.4 Fitting to Degree of Polarization Data 73
7.5 Efficiency Improvements 76
7.5 Summary 78

CHAPTER 8 - APPLICATIONS OF FEM FITTING

8.1 Introduction 79
8.2 Example Fit to Bonded Device 79
8.3 FEM Fits of Chips on Pre-Deposited Carriers 81
8.4 Photoelastic Effect Owing to Die Bonding 90
8.4.1 Experimental Procedure 90
8.4.2 Results and Discussion 92
8.4.2.1 Waveguide Mode 92
8.4.2.2 Far Field 95
8.4.2.3 Photoelastic Effect in Diode Lasers 98
8.5 Detection Voids in Die Bonding 98
8.6 Summary 101

CHAPTER 9 - DIE BONDING OF DISTRIBUTED FEEDBACK LASERS

9.1 Introduction 102
9.2 Experimental Procedure 102
9.2.1 Die Bonding 102
9.2.2 Spectral Measurements 103
9.3 Results 103
9.3.1 Stopband Width 104

9.3.2 Modes....106
9.3.3 Lasing Mode Flipping....111
9.4 Discussion....111
9.4.1 Bonding Strain....111
9.4.2 Strained Grating....112
9.4.3 Multiple Phase-Shifted Lasers....114
9.4.4 Mode Flipping....115
9.5 Summary....119

CHAPTER 10 - CONCLUSION

10.1 Introduction....120
10.2 Review of Work....120
10.2 Suggestions for Future Work....121
10.3 Summary....123

REFERENCES....124

INDEX....128

LIST OF FIGURES

Fig. 2.1 Orientation of chip for DOP and ROP measurements. 9
Fig. 2.2 Experimental setup used for DOP and ROP measurements. 11

Fig. 3.1 Schematic showing example diode laser die bond. 14
Fig. 3.2 Diagram to define the wetting angle φ of a liquid on the surface of a solid 15
Fig. 3.3 Binary phase diagram for Pb-Sn 17
Fig. 3.4 Binary phase diagram for Au-Sn 18

Fig. 4.1 Cooling profile for fast and slow cooling processes 26
Fig. 4.2 False colour maps of DOP (top) and ROP (bottom) on facet of unbonded diode laser 28
Fig. 4.3 False colour maps of DOP (top) and ROP (bottom) on facet of rapidly cooled diode laser 28
Fig. 4.4 False colour maps of DOP (top) and ROP (bottom) on facet of slowly cooled diode laser 28
Fig. 4.5 Area of averaging for DOP and zoomed in section of ridge and trenches with illustrative spot drawn to show approximately where light is generated in the laser (dimensions in µm) 31
Fig. 4.6 DOP data for rapidly cooled, slowly cooled, and unbonded chips. The mean values for each are marked by an × to the right of each set of data 32
Fig. 4.7 Wavelength shift owing to temperature change for range of applied currents for slow cooled and fast cooled device. The slopes of these best fit lines are used as relative measures of the thermal impedance 32
Fig. 4.8 AFM images of the surface of exposed solder on the chip carriers. (a) rapidly cooled sample (b) slowly cooled sample (image dimensions are 150 µm × 150 µm) 33
Fig. 4.9 SEM image of bonding interface away from the ridge 34
Fig. 4.10 AES line scan across bond interface for slowly cooled device. (a) location of scan (b) AES results along scan line 35
Fig. 4.11 AES line scan across bond interface for rapidly cooled device. (a) location of scan (b) AES results along scan line 35

Fig. 5.1 Typical temperature profile over time during die bonding with automated machine, measured on a strip-chart recorder. The reflow temperature is designated by "×" and the reflow time is designated by "+" in the figure 42
Fig. 5.2 Map of DOP scan (top) for the facet of an unbonded chip aligned with a diagram (bottom) that is representative of the matching metallization pattern on the bottom of the chip 43
Fig. 5.3 DOP (left column) and ROP (right column) maps from the reflow temperature experiment. Two pairs of maps for each of the reflow temperatures: 300° C (top), 350° C (middle), and 400° C (bottom) 47
Fig. 5.4 DOP (left column) and ROP (right column) maps from the reflow time experiment. Two pairs of maps for each of the reflow times: 0 s (top), 5 s (middle), and 10 s (bottom) 48
Fig. 5.5 DOP (left column) and ROP (right column) maps from the carrier metallization experiment. Two pairs of maps for each of the three carrier types: A (top), B (middle), and C (bottom) 53

Fig. 6.1 Full facet DOP (left column) and ROP (right column) maps of a single device for each time, indicated on the left in hours, during the accelerated aging of the laser 57
Fig. 6.2 The decrease in average DOP for the device in Fig. 6.1 over the aging time....... 58

Fig. 7.1 Schematic of tetrahedral element 65
Fig. 7.2 Diagram of general steps in iterative fitting of FEM model to DOP and ROP data....... 76

Fig. 8.1 False colour maps of measured DOP (left) and ROP (right) of the facet of a chip bonded to a copper carrier....... 80
Fig. 8.2 False colour maps of modelled DOP (left) and ROP (right) from the chip shown in Fig, 8.1 80
Fig. 8.3 Strain data extracted from the FEM model. (a), ε_{xx}, and (b), ε_{yy}, are along horizontal lines taken 5 μm from the bottom of the chip. (c), ε_{xx}, is along a horizontal line taken 20 μm from the top of the chip 81
Fig. 8.4 Strain data extracted from the FEM model of an unbonded chip. It is ε_{xx} strain along a horizontal line 20 μm from the bottom of the chip 82
Fig. 8.5 False colour images of measured (left) and modelled (right) maps for the DOP (top) and the ROP (bottom) of a bonded chip....... 82
Fig. 8.6 Strain data extracted from the FEM model of the chip in Fig. 8.5. It is ε_{xx} strain along a horizontal line 20 μm from the bottom of the chip 83
Fig. 8.7 False colour images of measured (left) and modelled (right) maps for the DOP (top) and the ROP (bottom) of a bonded chip....... 84
Fig. 8.8 Strain data extracted from the FEM model of the chip in Fig. 8.7. It is ε_{xx} strain along a horizontal line 20 μm from the bottom of the chip 85
Fig. 8.9 Strain data extracted from the FEM model of the chip in Fig. 8.7 to show how the strain changes at different positions on the facet. On the left side are ε_{xx} strain plots taken at: (a) 10 μm, (c) 30μm, (e) 50 μm, (g) 70 μm, (i) 90 μm, and (k) 110 μm. On the right side are ε_{yy} strain plots taken along the same lines at: (b) 10 μm, (d) 30μm, (f) 50 μm, (h) 70 μm, (j) 90 μm, and (l) 110 μm....... 86
Fig. 8.10 False colour images of measured (left) and modelled (right) maps for the DOP (top) and the ROP (bottom) of a bonded chip....... 87
Fig. 8.11 Strain data plots extracted from the FEM model of the chip in Fig. 8.10. In (a) is ε_{xx} strain along a horizontal line 20 μm from the bottom of the chip. In (b) are ε_{yy} strain plots along *vertical* lines 100 μm to the left of the centre of the chip (solid line) and 100 μm to the right of the centre of the chip (dashed line)....... 88
Fig. 8.12 False colour images of measured (left) and modelled (right) maps for the DOP (top) and the ROP (bottom) of a bonded chip....... 89
Fig. 8.13 Strain data extracted from the FEM model of the chip in Fig. 8.12. It is ε_{xx} strain along a horizontal line 20 μm from the bottom of the chip 89
Fig. 8.14 Waveguide structure used in mode solving software. Dimensions are in μm 91
Fig. 8.15 Photoelastic effect in TE polarization along horizontal line at the facet, 5 μm from bottom of chip....... 92
Fig. 8.16 Lateral mode profile along active region for an unstrained waveguide....... 93
Fig. 8.17 Transverse mode profile near edge of ridge for an unstrained waveguide 93
Fig. 8.18 Lateral mode profile along active region for waveguide with altered refractive indices owing to the die bonding....... 94
Fig. 8.19 Transverse mode profile near edge of ridge for waveguide with altered refractive indices owing to the die bonding....... 94
Fig. 8.20 Far field amplitude of laser output for unstrained laser structure. The axes are

the angles from center and they range from - 45° to + 45° parallel and perpendicular, respectively, to the junction plane. The amplitude is normalized (unitless) 95
Fig. 8.21 Far field amplitude of laser output for the laser structure with altered refractive indices. The axes are the angles from center and range from - 45° to + 45° parallel and perpendicular, respectively, to the junction plane. The amplitude is normalized (unitless) 96
Fig. 8.22 Far field amplitude profile parallel to the junction plane 97
Fig. 8.23 Far field amplitude profile perpendicular to the junction plane 97
Fig. 8.24 Finite element method model of strain owing to die bonding in die bond that is free of voids. (a) Diagram of chip with coefficient of thermal expansion CTE_1 bonded to chip carrier with CTE_2. (b) Plot of strain in the chip along line 5 μm from the bonding interface 99
Fig. 8.25 Finite element method model of strain owing to die bonding in die bond with a void. (a) Diagram of chip with coefficient of thermal expansion CTE_1 bonded to chip carrier with CTE_2. (b) Plot of strain in the chip along line 5 μm from the bonding interface. Note the dip in the strain profile along the width of the chip due to the void 99
Fig. 8.26 False colour images of measured (left) and modelled (right) maps for the DOP (top) and the ROP (bottom) of a bonded chip 100
Fig. 8.27 Strain data extracted from the FEM model of the chip in Fig. 8.26. It is ε_{xx} strain along a horizontal line 10 μm from the bottom of the chip 101

Fig. 9.1 Unbonded (dashed) and bonded (solid) spectra of a p-up mounted diode laser at 21.5 mA. The bonded spectrum was shifted in order to align with the unbonded spectrum for comparison 104
Fig. 9.2 Unbonded (dashed) and bonded (solid) spectra of a p-down mounted diode laser at 20 mA. (a) Wide view of the spectra. (b) Expanded view of the modes below the stopband. (c) Expanded view of the modes above the stopband. The reference numbers in (b) and (c) help to identify the modes. The bonded spectrum was shifted in order to align with the unbonded spectrum for comparison 105
Fig. 9.3 Unbonded (dashed) and bonded (solid) spectra of a p-down mounted diode laser at 20 mA. (a) Wide view of the spectra. (b) Expanded view of the modes below the stopband. The reference numbers in (b) help to identify the modes. The bonded spectrum was shifted in order to align with the unbonded spectrum for comparison 107
Fig. 9.4 Unbonded (dashed) and bonded (solid) spectra of a p-down mounted diode laser at 20 mA. (a) Wide view of the spectra. (b) Expanded view of the modes below the stopband. (c) Expanded view of the modes above the stopband. The reference numbers in (b) and (c) help to identify the modes. The bonded spectrum was shifted in order to align with the unbonded spectrum for comparison 108
Fig. 9.5 Unbonded (dashed) and bonded (solid) spectra of a p-up mounted diode laser at 20 mA. (a) Wide view of the spectra. (b) Expanded view of the modes below the stopband. The reference numbers in (b) help to identify the modes. The bonded spectrum was shifted in order to align with the unbonded spectrum for comparison 109
Fig. 9.6 Scatter plot to show the percentage change before and after bonding in the separation between the first and second modes below the stopband for each device. 110

Fig. 9.7 Unbonded (dashed) and bonded (solid) spectra of a p-down mounted diode laser at 20 mA. The lasing mode is below the stopband in the unbonded spectrum and above the stopband in the bonded spectrum. The bonded spectrum was shifted in order to align with the unbonded spectrum for comparison 111
Fig. 9.8 Unbonded (solid) and bonded (dashed) spectra of a p-up mounted diode laser at 21.5 mA. The lasing mode is above the stopband in the unbonded spectrum and below the stopband in the bonded spectrum. The bonded spectrum was shifted in order to align with the unbonded spectrum for comparison 116
Fig. 9.9 Results of fitting the laser spectra from the device in Fig. 9.8 with the probability-amplitude transfer-matrix distributed feedback laser model. The measured (dashed) and modelled (solid) below threshold spectra are shown for the front (a) and back (b) facet spectra 117
Fig. 9.10 The ε_{zz} strain along the length of the grating owing to die bonding, determined using a finite element method model 118
Fig. 9.11 Modelled front facet spectra near threshold for the cases with (dashed) and without (solid) an imposed perturbation of the grating that simulated the effects of bonding. Without a change in the grating spacing, the lasing mode was above the stopband, like the unbonded spectrum in Fig. 9.8. With the perturbation the lasing mode flipped to below the stopband, like the bonded spectrum in Fig. 9.8 119

LIST OF TABLES

Table 2.1 Components used in the DOP measurement apparatus 11
Table 3.1 Some properties of materials relevant to die bonding 23
Table 4.1 Degree of polarization values 31
Table 4.2 Physical properties of Au-Sn metals and phases 38
Table 5.1 Breakdown of number of devices in each experiments 43
Table 5.2 Average DOP measurements and shear test data of bonded chips 45
Table 5.3 Carriers designed for use in carrier metallization experiment 51
Table 5.4 Average degree of polarization values for the three carriers 52
Table 6.1 Averaged DOP values for all devices 58
Table 8.1 Comparison of unstrained versus strained waveguide structure 97

CHAPTER 1 - INTRODUCTION

The concept of concurrent engineering is that all aspects of a design should be considered during the design phase of a product or device. That is, not only the details of the inner workings of a device but also things like manufacturability and testability should be defined and analyzed during design. The packaging of electronics and optoelectronics needs to be addressed in the earliest stages of a device's design so that appropriate specifications for packaging related details can be set. For example, diode lasers, which are temperature sensitive devices, have requirements for the removal of heat that need to be established early in the device design so that appropriate packaging decisions can be made. In devices that are to be modulated at high speed, the demands on the package must be specified to take into account the high frequency drive electronics. As well, the device designer must set specifications and tolerances on the allowable stresses that can be imposed on the device by the packaging.[1]

Among the various steps in fabricating semiconductor diode lasers, packaging remains a tedious part of the construction of a functioning optoelectronic device. The attachment of chips to carriers, wires to bonding pads, and alignment with lenses and fibres is a part of the design of diode lasers that often is viewed as not being as interesting or important as the device design itself. The engineering of optoelectronic packages is, however, a crucial part of the device since the package is what holds the device in place, provides electrical current for operation, a thermal path for heat removal, and an optical path for light output. It can also make up a significant portion of the cost of a completed diode laser module. One part of the packaging of diode lasers is die bonding.

Die bonding (also called die mounting or die attachment) is the act of attaching the laser die (also called a chip) to a submount or chip carrier. The purpose of the bond is to hold mechanically the die, and to provide electrical and thermal contact with the chip carrier. In high power diode lasers and diode laser bars the heat generated from devices producing 100's of mW of optical power can be quite significant and this heat needs to be removed. Peak heat flux densities in the kW/cm^2 range are experienced in high power diode lasers.[2] To ameliorate the ability of the laser package to remove heat generated in the active region, diode lasers are sometimes packaged p-side down.[3]

The procedure of die bonding a diode laser can result in strain in the laser chip. This is a consequence of thermal stress owing to the differences in thermal expansion coefficients of the materials and the elevated temperatures involved in the procedure. The effect of strain on diode lasers has been studied extensively and its effect on device reliability has been well documented. Strain has been shown to accelerate degradation in optoelectronic devices.[4][5][6][7] Strain can perturb the equilibrium concentration of point defects and their migration throughout crystalline material. This can have a deleterious effect on the reliability of diode lasers. Also, strain in the active region of a diode laser can

affect the threshold current, wavelength, and polarization of emitted light.[8][9] In p-down bonding the strain from bonding is particularly important since the active region is so close to the interface. Strain near the active region could have an impact on the optical guidance, the gain, and any grating providing feedback as part of the laser.[10][11]

The purpose of this thesis is to explore the die bonding of diode lasers, with particular attention to the stress and strain that result. It will be shown that die bonds can result in different strain patterns in diode laser chips. This strain can affect the performance of diode lasers and this will be investigated as well. Using the degree of polarization (DOP) of photoluminescence it is possible to ascertain information related to strain in diode laser material.[12] To carry this further, an iterative finite element method model was developed that fits to DOP data to determine components of stress and strain owing to die bonding. Also included is work on the effect of varying a number of parameters in the die bonding procedure. Following the literature on the progression of research into diode laser packaging a number of modes of failure related to die bonding were identified early by others and have since been corrected.[13]

This document is organized into ten chapters. The first is this introductory chapter to give an overview of the research conducted. The second chapter gives definitions of stress and strain as well as a synopsis of the method of strain measurement using the degree of polarization of photoluminescence. The chapter goes over general elasticity relationships and a conceptual sketch of DOP measurements and details of the system to make such measurements. The third chapter provides a summary of the die bonding of diode lasers. It explains the principle of adhesion and the important materials and techniques used in die bonding. In addition, at the end of the chapter is a table that lists a number of material properties of key materials used in diode laser bonding.

The fourth chapter is a study on the effect of the cooling rate on diode laser die bonds.[14] The chapter will outline an experiment conducted on the cooling rate and the results of a number of measurements made with respect to the diode lasers and materials. In the fifth chapter there is a description of a set of experiments dealing with pre-deposited solder on chip carriers. The first experiments look into the effect of reflow time and reflow temperature on die bonds. There is then an experiment detailed that examines the effect of the metallization scheme used on the carrier. The sixth chapter is a study that explores stress relaxation in diode laser die bonds. This study uses data from a larger accelerated aging investigation to measure how thermal stress changes over the lifetime of a die bond.

The seventh and eighth chapters deal with a finite element method (FEM) model that was written to extract detailed information from DOP measurements. In the seventh chapter there is a summary of the finite element method and a derivation of the elasticity model used in the code. In addition, there is an explanation of how the FEM model fits to DOP data taken from the facet of

bonded laser chips.[15] The eighth chapter provides examples of fits made using the code described in the seventh chapter. There are comparisons of modelled and measured false colour maps to demonstrate how well the model is able to reproduce the details from the measurements. Also, there is an examination of the effect of bonding strain on the guiding of a ridge waveguide bonded p-side down.[16] The final part of that chapter shows how the fitting model can be used to detect voids in the bonds of diode lasers.

The ninth chapter explores the effect of die bonding on the spectrum of distributed feedback lasers. In that chapter, a number of distributed feedback lasers had their spectra measured before and after bonding to see if there were changes owing to the strain induced by die bonding. The tenth chapter is a closing chapter to summarize the work in this thesis and provide some concluding remarks as well as suggestions for future work.

CHAPTER 2 - STRESS AND STRAIN IN DIODE LASERS

2.1 Introduction

A number of procedures in semiconductor device manufacturing are stress inducing. In epitaxy, stress can be created owing to the lattice mismatch of layers of grown semiconductor material. During the deposition of thin films, stress can be created owing to the elevated temperatures and the differences in the thermal expansion coefficients of the materials. In die bonding, thermal stresses are induced for the same reason. Thermal stress is caused by the difference in the coefficients of thermal expansion (CTE) of the laser chip, the adhesive, and the chip carrier and the difference in the processing and operating temperatures of the device. This chapter is an introduction to stress and strain, and how they are measured in diode laser materials. Section 2.2 gives definitions of stress and strain and their relationship. Section 2.3 describes how stress and strain are related to the polarization of photoluminescence. Section 2.4 is an overview of the experimental system used to make degree of polarization measurements.

2.2 Elasticity

Since much of this thesis deals with stress and strain in diode lasers, this section will define these concepts. In the simplest sense stress is a force per unit area. At a point, the stress is defined as the limiting value of the average force applied per unit area as the area approaches zero: [17]

$$\sigma = \lim_{\Delta A \to 0} \frac{\Delta F}{\Delta A} = \frac{dF}{dA} \tag{2.1}$$

The force dF is not, in general, applied orthogonal to the surface area dA. It can be decomposed into components parallel and perpendicular to any given plane. The general three dimensional state of stress at a point is determined by nine stress components, of which six are independent. There are three normal stresses, which act perpendicular to the plane of interest and three shear stresses which act in the plane. The nine stress components form a second rank tensor, the stress tensor σ_{ij}. In column matrix form the six components of the stress tensor can be written as:

$$\begin{bmatrix} \sigma_{xx} \\ \sigma_{yy} \\ \sigma_{zz} \\ \sigma_{xy} \\ \sigma_{xz} \\ \sigma_{yz} \end{bmatrix} \tag{2.2}$$

where σ_{xx}, σ_{yy}, and σ_{zz} are the normal stresses and σ_{xy}, σ_{xz}, and σ_{yz} are the shear stresses using Cartesian notation.

Strain quantifies the deformation of a material. It specifies the change in the relative positions of points in a body. In the simplest one-dimensional case, the strain is the unit change in length, $\varepsilon = \frac{du}{dx}$ where the strain ε represents the proportional displacement of the infinitesimal du in the x direction. The state of strain at a point is, in general, represented by nine strain components, of which six are independent. There are three normal strains and three shear strains. The components of strain form a second rank tensor, ε_{kl}. The six independent components can be written in a column matrix form as

$$\begin{bmatrix} \varepsilon_{xx} \\ \varepsilon_{yy} \\ \varepsilon_{zz} \\ \varepsilon_{xy} \\ \varepsilon_{xz} \\ \varepsilon_{yz} \end{bmatrix} \tag{2.3}$$

where ε_{xx}, ε_{yy}, and ε_{zz} are the normal strains and ε_{xy}, ε_{xz}, and ε_{yz} are the shear strains using Cartesian notation. The normal strains are defined as the per unit elongation in the Cartesian directions:

$$\varepsilon_{xx} = \frac{\partial u}{\partial x} \qquad \varepsilon_{yy} = \frac{\partial v}{\partial y} \qquad \varepsilon_{zz} = \frac{\partial w}{\partial z} \tag{2.4}$$

where u, v, and w are the displacements in the x, y, and z directions respectively. The mathematical shear strains are defined as:

$$\varepsilon_{xy} = \frac{1}{2}\left(\frac{\partial u}{\partial y} + \frac{\partial v}{\partial x}\right) \qquad \varepsilon_{xz} = \frac{1}{2}\left(\frac{\partial u}{\partial z} + \frac{\partial w}{\partial x}\right) \qquad \varepsilon_{yz} = \frac{1}{2}\left(\frac{\partial v}{\partial z} + \frac{\partial w}{\partial y}\right) \tag{2.5}$$

Frequently, engineering shear strains are used in elasticity analysis. These are twice the mathematical shear strains:

$$\gamma_{xy} = 2\varepsilon_{xy} \qquad \gamma_{xz} = 2\varepsilon_{xz} \qquad \gamma_{yz} = 2\varepsilon_{yz} \tag{2.6}$$

The engineering shear strains, γ, are approximately equal to the change in the original right angle between two axes, as measured in radians. Engineering shear strains are often used because they can be computed simply using matrix arithmetic. However, they do not form a tensor in a strict mathematical sense. In a wide range of engineering problems, the engineering shear strain is used because of its relative ease of use.[17]

In the case of linear materials, the second rank stress and strain tensors are related by another tensor, C_{ijkl}, the modulus tensor:

$$\sigma_{ij} = C_{ijkl}\varepsilon_{kl} \tag{2.7}$$

This fourth rank tensor has 81 components but by symmetry there are actually a maximum of 36 independent components. The tensor relation, expressed in condensed indicial notation in (2.7), can be written out in a matrix form as:

$$\begin{bmatrix} \sigma_{xx} \\ \sigma_{yy} \\ \sigma_{zz} \\ \sigma_{xy} \\ \sigma_{xz} \\ \sigma_{yz} \end{bmatrix} = \begin{bmatrix} C_{11} & C_{12} & C_{13} & C_{14} & C_{15} & C_{16} \\ C_{21} & C_{22} & C_{23} & C_{24} & C_{25} & C_{25} \\ C_{31} & C_{32} & C_{33} & C_{34} & C_{35} & C_{36} \\ C_{41} & C_{42} & C_{43} & C_{44} & C_{45} & C_{46} \\ C_{51} & C_{52} & C_{53} & C_{54} & C_{55} & C_{56} \\ C_{61} & C_{62} & C_{63} & C_{64} & C_{65} & C_{66} \end{bmatrix} \begin{bmatrix} \varepsilon_{xx} \\ \varepsilon_{yy} \\ \varepsilon_{zz} \\ 2\varepsilon_{xy} \\ 2\varepsilon_{xz} \\ 2\varepsilon_{yz} \end{bmatrix} \quad (2.8)$$

Notice that in this equality, written in matrix form, the engineering shear strains are used. It puts the tensor equation in a matrix form which is convenient for computation. The 6×6 matrix is known as the modulus matrix and it contains the stiffness constants for the material (in units of force per unit area). The inverse proportionality quantities are known as the compliance constants and they form the compliance tensor, S_{ijkl} (in units of area per unit force).[18] These relations are approximate but hold on the assumption of small deformations. A more exact description would involve higher order terms.

The tensor equality is a generalized form of the well-known Hooke's law: $\sigma = E\varepsilon$, which expresses that a stress is proportional to a strain via Young's modulus. Another quantity in elasticity is Poisson's ratio which expresses the relationship between the strain in one direction owing to the stresses in the other directions. For a homogeneous, isotropic material, Young's modulus and Poisson's ratio completely describe the elastic properties of the material. InP is an orthotropic material which has three independent stiffness components: C_{11}, C_{12} and C_{44}.

2.3 Degree of Polarization of Photoluminescence

The effect of stress and strain on the photoluminescence of III-V materials has been well researched.[19] It is established that strain alters the symmetry of III-V materials and causes splitting of the heavy-hole and light-hole bands in the band structure of the deformed crystal.[20] This modifies the probability of emission in different polarizations.[12] The degree of polarization is defined here as the difference over the sum of orthogonal polarizations of luminescence. Referring to the orientation in Fig. 2.1 the degree of polarization (DOP) is:

$$\mathrm{DOP} = \frac{L_x - L_y}{L_x + L_y} \quad (2.9)$$

where L_x and L_y are the measured intensities polarized according to the figure. In this case, "x" and "y" are the directions in the plane of the material; in the (110)

plane for cleaved facets of III-V material. The "z" direction is out of the plane. It has been shown that in an isotropic material the degree of polarization is proportional to the difference of normal strains or the difference of normal stresses in the plane:

$$\mathrm{DOP} = -K_{\varepsilon}\left(\varepsilon_{xx} - \varepsilon_{yy}\right) = -K_{\sigma}\left(\sigma_{xx} - \sigma_{yy}\right) \qquad (2.10)$$

where σ_{xx} and σ_{yy} are the normal stresses, ε_{xx} and ε_{yy} are the normal strains, K_{σ} and K_{ε} are experimentally determined proportionality constants. For an orthotropic material such as InP, it is not true in general that the DOP is proportional to both the difference of stresses and the difference of strains. In recent calibration work with InP it has been found that the difference of strains resulted in a better fit to simulation.[21] In that work, InP bars with V-grooves etched into them were subjected to external loads and the measured DOP patterns were fitted to simulated DOP patterns. It makes sense physically that the difference of strains should be more accurate since it is the actual shifting of the positions of atoms in the crystal that result in band structure changes that manifest as different luminescent intensities along opposite polarizations. However, in this thesis, both the difference of strains and stresses are used. This is because some of the early work was done under the isotropic assumption before the recent calibration results were known. For example, the finite element method fitting that is described later in the thesis was done using the difference of stresses with the calibration constant as determine by Colbourne.[22]

A related quantity to the DOP is the rotated degree of polarization (ROP). It is defined as the DOP rotated by 45° about the z-axis (in Fig 2.1). That is, the ROP is equal to the difference over the sum of orthogonal polarizations:

$$\mathrm{ROP} = \frac{L_{x'} - L_{y'}}{L_{x'} + L_{y'}} = \frac{L_{x'} - L_{y'}}{L_{x} + L_{y}} \qquad (2.11)$$

where $L_{x'}$ and $L_{y'}$ are the measured intensities polarized according to Fig. 2.1. The second equality holds since the denominator is a time-averaged quantity equal to the total intensity of the photoluminescence. It has been shown, see [22], for isotropic material that the ROP is equal to the shear strain or shear stress in the plane:

$$\mathrm{ROP} = 2K_{\varepsilon}\varepsilon_{xy} = 2K_{\sigma}\sigma_{xy} \qquad (2.12)$$

where σ_{xy} is the shear stress and ε_{xy} is the shear strain. For an orthotropic material, (2.10) and (2.12) do not hold for both stresses and strains. However, as it was shown in [21] there is not a striking difference between using stresses versus strains in these relations. For the majority of the time that the research for this thesis was being conducted, the DOP and ROP were assumed to be proportional to stresses and this is what had been done in previously in [4], [11], and [12]. Only towards the end of the research detailed in this thesis was it shown

that the DOP and ROP were better described as being proportional to strains. Since many time consuming iterative fits, as in Chapter 8, had been completed by the time that this was known conclusively it was decided to continue using the approximation that the DOP and ROP were proportional to stresses. The fitting code was altered to test whether using stresses or strains mattered in the iterative fits and it was found that by using strains in (2.10) and (2.12) there was a slight improvement in the quality of the fits, as measured by the minimum of the error of the model versus the measurements as explained in Chapter 7. This was not noticeable in the false colour images created for comparison between the measurements and the models assuming stresses and the models assuming strains. For this reason, although both equalities in (2.10) and (2.12) do not hold rigorously for orthotropic materials, it has been found experimentally that the difference is small and so stresses were used throughout this thesis.

It is therefore possible to determine stress and strain related information by measuring the DOP and ROP of photoluminescence from III-V material. To do this it is necessary to make polarization-resolved measurements of the photoluminescence of the material, as is described in the following section. Only InP-based devices were investigated for this thesis. For InP, the calibration constants were determined to be $K_\varepsilon = -65 \pm 10$ (unitless) and $K_\sigma = -(9.4 \pm 1.0) \times 10^{-11}$ (cm^2/dyn).[21][22]

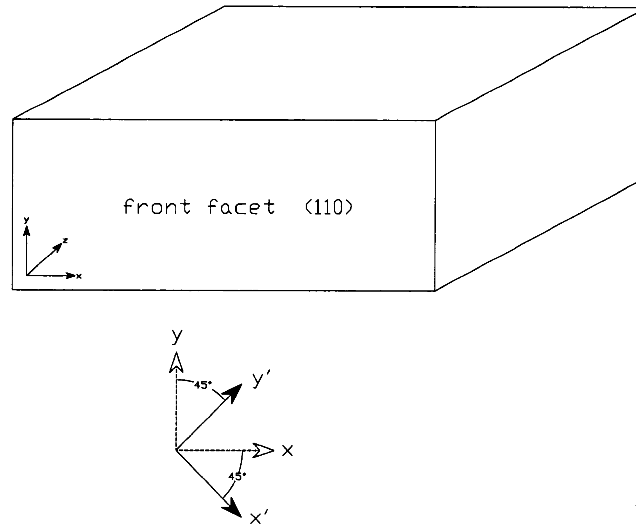

Fig. 2.1 Orientation of chip for DOP and ROP measurements.

2.4 DOP Apparatus

To determine the degree of polarization (DOP) and the rotated degree of polarization (ROP) at a point in III-V material it is necessary to measure the sum and difference of the orthogonal polarization intensities at the point. The system

used in this work to measure the degree of polarization of photoluminescence is a computer controlled apparatus that optically excites a semiconductor sample and measures the polarization components of the resulting luminescence. Figure 2.2 is a schematic diagram showing the principal components of the system. Details of the components used in the system are shown in Table 2.1. A HeNe laser is used as the pump source. Emission from this laser goes through an optical isolator to limit any feedback noise and then through some neutral density filters to adjust the pump intensity. The light is mechanically chopped using a crystal stabilized optical chopper operating at 1120 Hz. It was found that this frequency resulted in the lowest system noise and that drifting of this frequency by less than 1% caused noticeable noise in the DOP and ROP maps. For this reason a high precision optical chopper that is phase-locked to an internal frequency synthesizer has been adopted in the apparatus. The frequency is stable to within 1 Hz.

The chopped pump beam is reflected by a mirror through a lens and then a cold mirror towards a microscope objective. The lens adjusts the beam so that the microscope objective focusing the beam is compensated for chromatic aberration due to the difference in the pump light and the photoluminescence wavelengths. The objective is used in a confocal arrangement such that the pump light is focused on the sample and the photoluminescence is collected along the same path. The cold mirror at the other end of the system rejects the majority of the pump light and a second filter eliminates the remainder, permitting the photoluminescence to pass. The photoluminescence then passes through a rotating polarizer and is detected by a stationary detector with a 200 μm pinhole entrance. The polarizer rotates at 200 Hz. The rotating linear polarizer, through phase sensitive detection electronics, permits the time-averaged measurement of the in-phase (L_x - L_y) and quadrature ($L_{x'}$ - $L_{y'}$) luminescence components and the total luminescence ($L_x + L_y$) simultaneously.

The lock-in amplifiers used in the detection system output their digitized signals to the computer and the DOP and ROP are computed and recorded for each point on the sample. The whole apparatus is fixed except for the motorized stage on which the diode laser sample is mounted. This stage is used to step the sample so that a raster scan map of the DOP and ROP can be created using measurements at different points on the sample. The stage is capable of sub-micrometre positioning but for the work in this thesis larger step-sizes were used. For most of the DOP and ROP maps displayed in this work, the scans took about 45 minutes each. The pump light is absorbed within a short distance of the surface being scanned so the DOP and ROP data at each point correspond to strains near the surface.

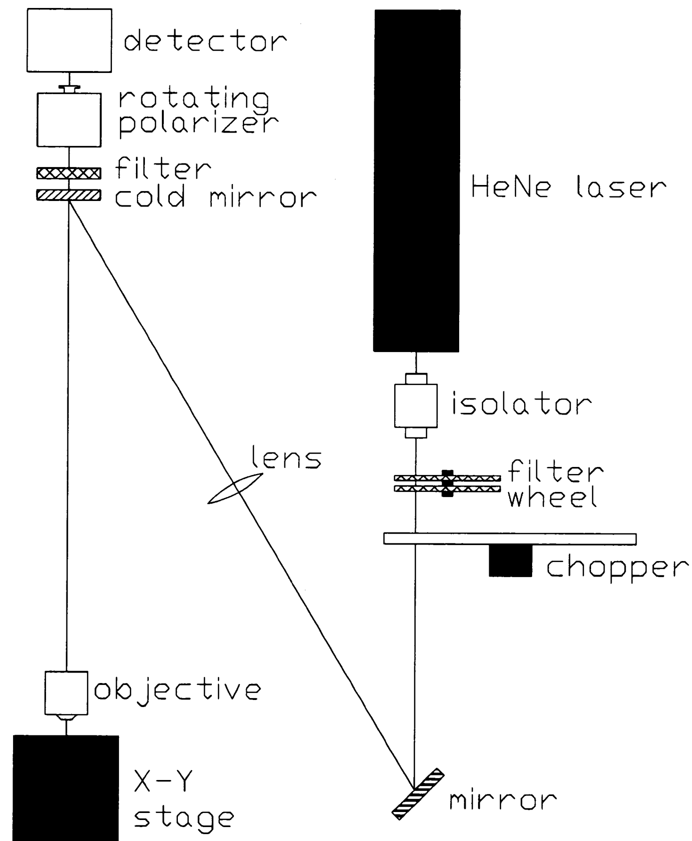

Fig. 2.2 Experimental setup used for DOP and ROP measurements.

Table 2.1 Components used in the DOP measurement apparatus.

COMPONENT	PART NUMBER
detector	EG&G silicon C30807E
rotating polarizer	Polarcor optical glass polarizer 900HC
cold mirror	Melles Griot 03MCS005
objective	Melles Griot 10× N.A.: 0.30
XY-stage	Melles Griot Nanomotion II Positioning Actuator System
chopper	New Focus 3501 Optical Chopper
filter wheel	New Focus 5215 0.08-3.0 Dual Neutral Density Filter Wheel
isolator	Optics For Research IO-3-633-LP Narrowband Adjustable Isolator
laser	Uniphase 632.8 nm HeNe laser

2.5 Conclusion

This chapter was an introduction to stress and strain measurement in diode lasers. Section 2.2 defined stress and strain and explained the relationship between the two for a general tensor case. It was explained that there exist mathematical shear strains and engineering shear strains and that these differ by a factor of two. Only mathematical shear strains are part of the strain tensor, according to the mathematical definition of a tensor. Section 2.3 specified how luminescence is related to strain in material. Section 2.4 illustrated and explained the experimental system used to make degree of polarization measurements. This chapter was meant to provide a basis for understanding the DOP measurements that are depicted throughout the thesis.

CHAPTER 3 - DIODE LASER BONDING

3.1 Introduction

In designing the packaging for semiconductor lasers, there are many choices that have to be made. These include the materials and procedures used in mounting laser chips. This chapter explains some details of die bonding and some of the materials and procedures available to packaging engineers. It is preliminary information to define terms that are used in the remainder of the thesis. Section 3.2 explains what a die bond is and shows an example diagram of a typical die bond. Section 3.3 deals with adhesion in general and its relevance to packaging. In Section 3.4 there is a description of the use of soldering for the attachment of diode laser chips. It is explained there why solder wetting is important, what forms of solder exist for optoelectronic packages, and what is involved in alloy selection. Section 3.5 discusses the use of epoxies for bonding diode laser chips. The chip carriers and submounts used in die bonding are detailed in Section 3.6. Finally in Section 3.7 a collection of the materials and some of their properties pertinent that are to bonding is presented.

3.2 Die Bonding

Die bonding of diode lasers is the process of attaching a laser die (also called a chip) to a submount or chip carrier. The attachment has to fulfill each of the following: to be a robust mechanical junction, to act as a low thermal impedance path to remove heat, and to provide a high quality ohmic contact. The adhesive used must balance each of these issues and not reduce the performance of the device. A typical diode laser chip has dimensions on the order of a few hundred microns. This is significantly smaller than most electronic devices, making diode laser die attachments relatively difficult. In addition, diode lasers are very temperature sensitive so their thermal management requirements can be quite strict. These issues make it challenging to choose the appropriate type of materials and the procedures for packaging.

A typical die bond consists of a semiconductor chip attached on top of a chip carrier by way of an adhesive such as solder or epoxy. The semiconductor chip may be a single laser chip or a number of lasers as an array. The chip carrier is what holds the semiconductor chip, conducts heat away from the laser, and is usually the platform for wire bonding to the chip. In solder bonding, a chip is brought into contact with a metal alloy which is contacting a chip carrier. With the temporary application of heat, the temperature of the ensemble is raised above the melting point of the solder alloy. The liquid solder adheres to both chip and carrier and upon cooling a solid joint is formed between the chip and carrier. The bond is held by way of metallic bonding. Because of the small dimensions of diode laser chips and the tight tolerances for alignment, precise machines are used to bond laser chips. Such machines place chips and carriers with vacuum pick-up

tools and provide a heat source to melt the solder. Diode lasers can be bonded with active region side up (p-up bond) or with the active region side down (p-down bond).

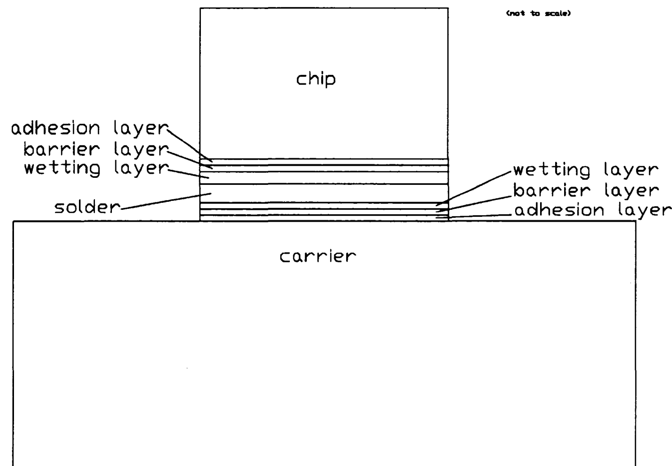

Fig. 3.1 Schematic showing example diode laser die bond.

Figure 3.1 is a schematic of a typical die bond of a diode laser. The laser chip is attached to the chip carrier with solder. There are a number of metallic thin films on the chip and carrier serving several purposes to be discussed later in this chapter. The combined thermal impedance of the materials limits the ability of the package to remove heat created in the junction of the laser. This impedance owes to the properties inherent of the materials as well as to non-uniformities in the materials, such as voids. Electrical contact is usually made to a laser chip from the die bond below and a wire bond attached above.

3.3 Adhesion

The binding of diode lasers to chip carriers can be accomplished using a number of methods. In general, the material used to attach two components together is known as an adhesive while the two components being attached are known as adherends.[23] To understand how materials adhere to each other, and ultimately how diode laser die bonds are formed it is necessary to consider the details of the surfaces. This knowledge helps in understanding some of the issues that arise practically in die bonding.

The concept of surface tension is important in comprehending how materials adhere.[24] Surface tension describes the tendency of a surface, as a result of intermolecular forces near the surface, to resist deformation by foreign materials. Surface tension defines the increase in free energy of a system that is

described by two interfacial phases when the interfacial area is increased by one unit at constant temperature and pressure. Surface tension has units of energy per unit area.[25] The surface of a liquid or solid is actually an interface in equilibrium with another phase (solid, liquid, or gas). The definition of a surface, for example a liquid-gas interface, is given by the surface tension, such as a liquid-gas surface tension.[25] To maintain a stable surface a positive value of surface tension is required, otherwise there would be unlimited expansion of the surface. Since surface tension γ is an energy per unit area, a positive work is required to extend a surface, $W = \gamma\, dA$. As an example, a liquid droplet with a positive surface tension, in the absence of other forces, will tend to form a sphere to minimize its surface area.

The impetus for adhesion is principally thermodynamic. That is, two bodies will adhere if their total free energy is lowered by being united. For a liquid to adhere to a solid and lower the total free energy of the system, wetting is required. Wetting is the limited spreading of a liquid on a solid surface. The wettability is measured by the wetting angle, the contact angle between a drop of liquid on a flat solid surface.[23] The wetting angle φ is expressed in the Young relation:

$$\gamma_{SV} - \gamma_{SL} = \gamma_{LV} \cos(\varphi) \qquad (3.1)$$

where γ_{SV} is the solid-vapour tension, γ_{LV} is the liquid-vapour tension, and γ_{SL} is the liquid-solid tension. The wetting angle is a quantitative means of assessing the adhesion of a material with a given adhesive. When the wetting angle is less than 90° the liquid is said to wet the surface of the solid as shown in Fig.3.2

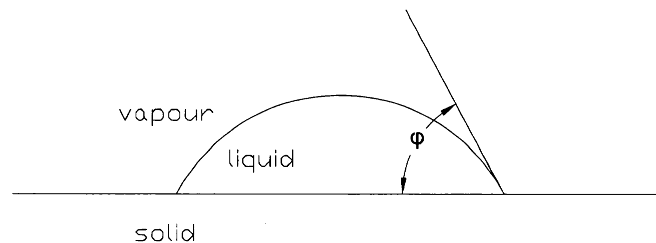

Fig. 3.2 Diagram to define the wetting angle φ of a liquid on the surface of a solid.

A liquid must wet the surface of the solid in to be able to adhere to it. When a liquid does not wet a surface well the contact area is small and there is little adhesive strength. In a situation of poor wetting the adhesive is said to "ball" up, forming balls of the adhesive on the surface of the adherend. The adhesive is then minimizing its contact area with the adherend, which is highly undesirable. To achieve wetting, the difference of the solid-vapour and solid-liquid surface tensions should be maximized.[25]

The forces responsible for the adhesion depend on the materials used and may be owing to hydrogen bonding or metallic bonding, as examples. In electronic packaging the wettability of a component with respect to an adhesive is an important criterion in selecting the adhesive. The surface properties, i.e. the surface tensions, of the component and the adhesive must be compatible to allow for good adhesion. Contamination of surfaces by foreign substances such as oxides alters these properties and, hence, the adhesion. Surface preparation, such as the use of a flux or forming gas in solder bonding, is an integral part of a die bonding procedure. The choice of contact metallizations and alloys in solder die bonding is motivated by the need to have compatible materials for adhesion.

3.4 Solder Bonding

In a solder joint a metallurgical bond is formed between the adherends and the adhesive; i.e., when the solder freezes the joint is held together by metallic bonding.[25] In an ideal joint the solder and the base metal form a continuous connection via metallic bonding. That is, the liquid solder melts a small part of the base metal and mixes with it so that when cooled there is a continuum of metal through the joint. The choice of alloy for use as a solder is influenced by a number of factors such as compatibility with the base metal, freezing point of the molten alloy, and mechanical properties of the solder material.

3.4.1 Wetting

To form a good bond, the solder must wet the surface of the base metal. Poor wetting can cause the formation of voids. The wetting angle must be minimized and this is accomplished with the help of a reducing agent. Contaminants and oxide layers, even in thin layers, must be removed to achieve proper wetting and a good bond. To accomplish this, a flux is used. There are a number of types of fluxes; solid, liquid, and gaseous. There are rosin-based fluxes, organic fluxes, inorganic fluxes, and synthetically activated fluxes. They all serve the same purpose, although with differing degrees of corrosiveness and chemical activity. The principal purpose is to remove tarnishing films from the bonding surface and prevent oxidation during soldering thereby lowering the surface tension of the solder.[25] In diode laser die bonding usually a gaseous flux is used and is called forming gas. It is composed of some reducing chemical such as hydrogen mixed with an inert gas like nitrogen. This form of flux is used with optoelectronic components because it is clean compared with liquid fluxes and does not require any post-bonding cleaning bath to remove excess flux.

3.4.2 Alloy Selection

The choice of material to use as a solder has to do with material compatibility with the adherends and the desired properties of the solder joint.[26]

It is possible to use a pure metal as a solder, although more frequently alloys are used. The reason for this is that the physical properties of the solder can be tailored with alloy selection. The strength, hardness, melting point, thermal and electrical conductivity of an alloyed joint depend on the composition of the alloy. A commonly used alloy in electronics is lead-tin. The eutectic point is the composition for which the melting point is the lowest for an alloy. For lead-tin the eutectic point is near 63 (weight percent) Sn. This can be seen in the phase diagram for the Pb-Sn system in Fig 3.3. At the eutectic point the liquidus, above which material is entirely liquid, and the solidus, below which material is entirely solid, coincide. For both pure lead or pure tin at either end of the diagram, the melting points are higher. There are regions in which there are solid and liquid phases in equilibrium (L+α, L+β) and solid phases in equilibrium, (α+β). The mechanical properties of an alloy vary across the range of its composition.[27] The Pb-Sn alloy is a relatively simple binary system and it has a simple eutectic point.

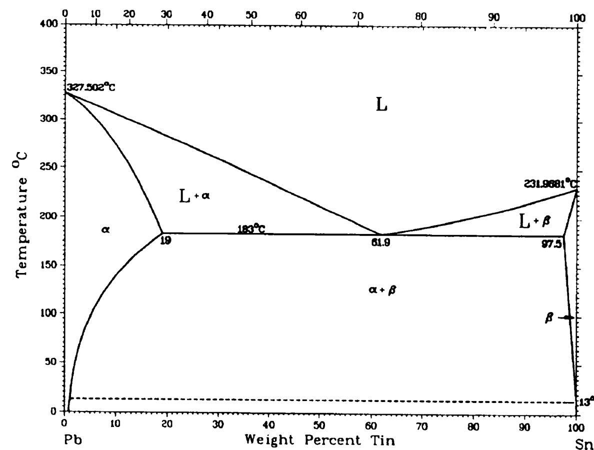

Fig. 3.3 Binary phase diagram for Pb-Sn.[28]

Solders can be roughly classified as soft or hard depending on their physical properties. Hard solders are mechanically stiff and have high melting points whereas soft solders show the opposite characteristics. Examples of hard solders are Au/Sn, Au/Ge, and Au/Si. Since hard solders freeze at higher temperatures they induce greater stress in diode lasers. In addition to this their higher stiffness makes hard solders less compliant and less able to provide strain relief to bonded laser chips. Soft solders are compliant and do give strain relief to the chip, however over time the solder can deform sufficiently that the joint weakens and degrades or the chip even becomes misaligned in the package. Au/Sn has the lowest eutectic point of widely used hard alloys and for this reason it has become a very popular material for die bonding. Compared with other binary alloys the Au/Sn alloy system is relatively complicated with many phases.

For Au/Sn the melting point of the eutectic composition is significantly lower than that of pure gold. The melting point of pure gold is over 1000° C but with the addition of only 20% (weight) tin it drops to only 280° C, as is visible in the Au/Sn phase diagram in Fig. 3.4.[29]

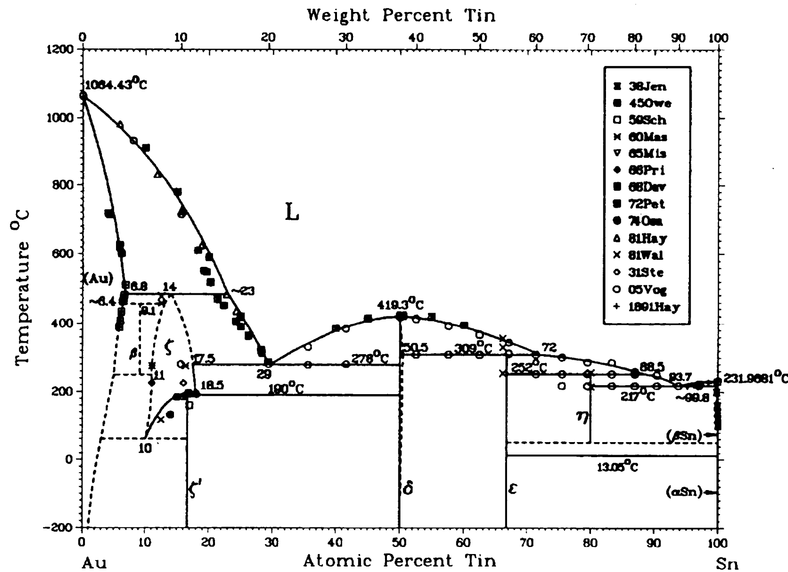

Fig. 3.4 Binary phase diagram for Au-Sn.[28]

In early diode laser packages pure indium was used as a solder since it had a low melting point. It was found, however, that since it was soft the indium joint degraded with time and usage. This was the result of gold from the contact metallization on the chip diffusing into the solder and forming brittle intermetallic compounds and from indium migrating out from the bond. The intermetallic compounds reduced the thermal conductivity of the joints and made them mechanically weak.[30] This also occurred with lead-tin solders. Intermetallic compounds are special phases of alloys where stoichiometric proportions are the same over a small range of composition in the phase diagram. Intermetallic compounds have a narrow range of homogeneity, have simple stoichiometric proportions, and have atoms of identical species at identical sites in the lattice.[26] In addition the structure of intermetallic compounds are typically more complicated than pure metals or solid solutions. Tin and gold can form a number of intermetallic compounds which have undesirable properties such as being brittle and thermally resistant. Examples of these intermetallics of Au/Sn are: AuSn (δ phase), Au_5Sn (ζ' phase), $AuSn_4$ (η phase) and $Au_{10}Sn$ (β phase). Hard solders have shown better long term reliability in mechanical joints. It has been found that gold alloys produce hard solders with long lasting, reliable die bonds. While they too suffer from the embrittlement problem of gold from the

contact metallization being dissolved into the solder, steps have been taken in the metallization schemes used to help limit this by using diffusion barriers.

3.4.3 Solder Forms

Solder can come in a variety of physical forms. There exist *preforms* which are carefully manufactured slices of the solder metal (to specific dimensions and compositions). A preform is placed on top of a carrier and then the chip is placed on top of it with heat applied to melt it and form a bond. Another form of solder is *pre-deposited* solder and it has become quite popular in packaging optoelectronic materials since it enables a high degree of control. In this case the solder material is evaporated or electroplated onto the chip carrier or back side of the chip in advance of the die bonding. The solder layer can then be made thinner than with preforms. In bonding, the chip is placed on the carrier and heat is applied and the solder on the carrier melts and bonds the chip to it. This has been shown to be a method of die bonding that allows automation more easily and provides greater control over the die bonding process.

Precise deposition of solder onto chips and carriers has led to the development of a new method of solder bonding without the need for melting the materials. Essentially, carefully designed alloy layers are first deposited as films on the chip and the carrier. The chip and carrier are then brought into intimate contact with one another, under modest pressure, in an inert atmosphere at a temperature below the melting point of the materials. After a length of time solid state diffusion takes place between the layers of the deposited films and a bond is formed. This technique requires great care in the quality of the films and environment, but it has been shown to be successful in producing high quality die bonds.[31]

3.4.4 Metallizations

Metallization layers in diode lasers play an important role in packaging. Firstly, the metal contact layers on the n and p sides of a diode laser provide ohmic contacts to which wire bonds are attached and devices are bonded to chip carriers. Secondly, various metallization schemes are used to help control the soldering process in solder bonded devices. The metals used for these purposes and their thicknesses have to be chosen carefully to ensure compatibility with solders and the semiconductor material.

Ohmic contacts are essentially metal-semiconductor interfaces that serve as the electrical conduits through which current is delivered to the device. These are normally multiple layers of metals serving different purposes. Examples of these are adhesion layers, barrier layers, and capping, wetting, or contact layers. The contact or wetting layer is the external surface and is the metal that bonds with external connections. Gold is frequently used for this purpose since it is a noble metal. The barrier material is a layer which impedes the unwanted diffusion

or migration of atoms. The adhesion layer helps the other layers adhere properly to the semiconductor. The choice of these layers is based on their thermodynamic compatibility with each other and the materials to which they are deposited. This owes to their respective surface tensions and work functions.

The metallizations on chip carriers and submounts serve some important functions. Diffusion barriers help to prevent the migration of atoms into the solder which cause unwanted intermetallic compounds.[30] For example, tungsten has been used to prevent the diffusion of gold into indium solders and tin solders.[32] It is important to keep Au out of semiconductors since Au is a radiative poison that destroys light emitting devices quickly. Nickel, platinum, and chromium are other metals used as diffusion barriers. In addition, combinations of these metals have been used for this purpose. The barrier acts to keep the solder separated from metal which can adversely react with it and degrade its properties. In gold-tin solder it is desirable to limit the formation of intermetallic compounds. The barrier layer can therefore help to keep the composition of the solder as designed. For an InGaAsP-InP diode laser a common p-side metallization is Ti-Pt-Au and a common n-side metallization is Ni-Ge-Au.

For Au/Sn, 80/20 (weight percent) is a desirable composition for die bonding diode lasers. The steep liquidus on either side of this alloy makes it necessary to control the composition carefully as in Fig. 3.4. A depletion of tin or an excess of gold could cause premature freezing during die bonding. There is usually gold on the chip as a contact metallization layer and gold on the chip carrier for the same purpose to help solder wetting. This gold can melt into the solder and change the composition. A number of steps can be taken to attempt to keep the solder at the correct composition during bonding. The use of barrier metal layers (platinum, tungsten or nickel based for example) can control the unwanted spread of gold during die bonding. A barrier layer cannot halt gold spreading indefinitely but a carefully designed metallization can help to control it. By carefully selecting the solder composition of a binary alloy to be rich in the content of one metal with the expectation that it will dissolve the other metal from the chip a final eutectic composition will result. A typical example would be using a 73/27 gold/tin (weight percent) composition solder and bonding it to a chip that has a layer of gold on it. When the bonding temperature is raised to above the eutectic point the solder melts and as it starts to melt the gold from the chip melts into it. The resultant composition can then be made eutectic even if the starting composition of the solder was not. The outside contact metal must be able to wet well to provide a good die bond. Failure to have good wetting can result in poor adhesion and the formation of voids in the joint.

3.4.5 Chip Carriers and Submounts

Chip carriers and submounts serve a number of purposes. Chief among them is to simply hold the semiconductor diode laser in place. Since diode lasers are very small (on the order of hundreds of microns) carriers attached to them make their handling easier. It is also the platform on which the laser is operated. Part of holding onto the chip includes making electrical contact via the bottom and a wire bond on the top. This electrical connection may simply be a conductive path or be more complex electronics. For example, some carriers have specialized designs with inductors and resistors built into them to help match the diode laser reactance at high frequencies. The removal of heat from the diode laser is another function served by the carrier. Since semiconductor lasers are very temperature sensitive, the purging of heat generated in the active region is of paramount concern and must be dealt with efficiently. The materials that carriers of diode lasers are made from include silicon, diamond, copper, nickel, tungsten, aluminum nitride, and various composite materials or alloys. The choice of material is based on the thermal conductivity, the mechanical stiffness, and the coefficient of thermal expansion. Submounts are intermediate components that are bonded in between the chip and carrier. Submounts are sometimes used on top of chip carriers to help spread heat, to match thermal expansion coefficients, or to set the height to enable better coupling to a fibre.[30] Submounts are used, for example, in some high power diode lasers to spread the heat of lasers and conduct this heat to attached water-cooled copper heat sinks.

3.5 Epoxy Bonding

Epoxy adhesives are widely used in many industries for many purposes.[33] Their use in electronic and optoelectronic packaging is widespread as well. Epoxy adhesives work by way of hydrogen bonding. These adhesives come in the form of two components, the resin and the hardener, that must be mixed before curing. In addition to the resin and hardener, an epoxy can also contain filler material. This filler is used to tailor the properties of the epoxy and for electronic packaging the filler increases the epoxy's electrical and thermal conductivity. The typical filler for conductive adhesives is a metallic powder (copper, silver, gold, or nickel) embedded in the matrix of the epoxy material. Conductive adhesives are attractive for use in electronic packaging for a number of reasons, including ease of dispensing and being lead-free.[34]

In die bonding diode lasers, there are a number of differences between using conductive epoxies and solders. Epoxy is dispensed as a liquid and after the chip is attached it is cured at a medium heat. Solder must be heated higher than the melting point of the material which is considerably hotter than the temperature used for epoxy curing. In principle, solder joints can be reworked since the material can melt. This is opposite for epoxy which is normally permanently set once it is cured. Solder can be in a number of forms, such as pre-deposited

(metallized) or preforms. Pre-deposited solder can make for very precise die bonds. Epoxy cannot be pre-deposited in the same way and so it must be dispensed during bonding. Importantly, conductive epoxies typically have higher electrical and thermal resistances compared with solder material.

3.6 Materials

There are various materials used in die bonding diode lasers. In the following table are listed a number of them along with some pertinent properties. Some of this data will be used elsewhere in the thesis and it is amalgamated into one table here for reference. The elastic properties for the materials are assumed to be isotropic and are given as Young's modulus and Poisson's ratio, except for InP, which is orthotropic, and the three stiffness constants are given.

Table 3.1 Some properties of materials relevant to die bonding. [35][36][37][38][39][18][41]

MATERIAL	THERMAL CONDUCTIVITY ($W \cdot m^{-1} \cdot K^{-1}$)	ELECTRICAL RESISTIVITY $\times 10^{-6}$ ($\Omega \cdot cm$)	COEFFICIENT OF THERMAL EXPANSION $\times 10^{-6}$ (K^{-1})	YOUNG'S MODULUS (GPa)	POISSON'S RATIO (unitless)	MELTING POINT (°C)
SEMICONDUCTOR						
InP	68	--	4.56	$C_{11} = 10.11$ $C_{12} = 5.61$ $C_{44} = 4.56$	--	--
SOLDERS						
88Au 12Ge	43.9	30	14	72.7	--	361
80Au 20Sn	58.6	17.4	16.5	59.1	0.39	278
63Sn 37Pb	49.8	14.5	24	30.8	0.4	183
In	86	8.37	29	10.6	0.45	156
Sn	66.5	13.2	22.2	47.5	0.368	232
EPOXY						
EPO-TEK H20E	2	100-400	31	3.5 (est.)	0.3 (est.)	--
CARRIERS AND SUBMOUNTS						
Cu	398	--	16.2	132	0.339	--
AlN	170	--	4.5	345	0.22	--
Al_2O_3,	29.3	--	6.6	372	0.24	--
C diamond	2000	--	1.02	1048	0.104	--
SiC	193-250	--	4.9	480	0.19	--
Si,	148	--	2.62	162	0.222	--
SiO_2,	1.38	--	0.5	72.4	0.14	--
W	178	--	4.5	410	0.280	--
METALLIZATIONS						
Ni	90.7	6.84	13.3	199.5	0.312	--
Pt	71.6	10.6	9	170	0.39	--
Pd	71.8	10.8	11.2	121	0.39	--
Ti	21.9	42	8.35	120.2	0.361	--
Au	315	2.25	14.2	77.2	0.425	--

3.7 Summary

This chapter was an overview of diode laser die bonding. The chapter explained some aspects of die bonding that will be explored later. It introduced some terminology to be used in this thesis. The importance of wetting and its relevance to adhesion was discussed. In addition the metallizations of chips and carriers and the importance of alloy selection were stated. The purpose of carriers and submounts was explained and a review was given of solder bonding and the different forms of solder that exist. A section showing conductive adhesive epoxy was included as well. Finally, a table that collects a number of properties of materials relevant to diode laser bonding was presented.

CHAPTER 4 - COOLING RATE IN DIODE LASER DIE BONDS

4.1 Introduction

The cooling cycle in a soldering process is the time when the laser die and chip carrier cool after the solder has melted and refrozen. The rate of cooling may impact the die bond in diode laser packages in a number of ways and this section examines the effect of this bonding parameter. Diode lasers that were bonded using either a rapid cooling procedure or a slow cooling procedure were examined. In work by other researchers dealing with the cooling rate of die bonds it was found that GaAs dice sometimes resulted in chips physically cracking from the thermal stress of die bonding.[42] Such catastrophic failure was not observed in this experiment. The effects of cooling rate on InP chips were considered here. The fast and slow cooling cases were compared for mechanical strain, thermal impedance, bond metallurgy, bond strength, cross sectional composition and solder structure.

4.2 Experiment

Twenty-six diode lasers were die bonded in the experiment: nine via a rapid cooling procedure and seventeen via a slow cooling procedure. The number of samples of each were not equal because the chips and carriers were acquired from an industrial laboratory with an unknown supply. The experiment was carried out over several weeks without knowing the total numbers of materials that would be made available.

The diode laser samples were each bonded to AlN laser chip carriers with a Kulicke and Soffa hot spot manual die bonder using a fluxless procedure. The chip carriers were pre-deposited with Au-Sn solder. The diode lasers were InP based ridge waveguide devices and were bonded p-side down. On the p-side of each laser chip there was a 4 μm thick layer of Au. A stripe of nominal width 25 μm around the edge of the chip was left uncoated. The chip dimensions were 380 μm × 250 μm × 130 μm. The chip carriers were AlN ceramic with a 3.5 μm thick layer of 80/20 weight percent Au/Sn solder pre-deposited on top. This solder was laid on top of the gold, adhesion, and barrier layers on the chip carriers. The composition of these layers is proprietary.

The temperature of the workholder assembly (that which holds the chip carrier in place) was 261 ± 6 °C, which is around 20° C below the eutectic point of 278° C for the Au/Sn solder. The die collet temperature was slightly less than this (the die collet holds the laser chip in place via a vacuum). The die bonder works by preheating the chip and carrier via the die collet and workholder assembly, respectively, to a temperature below the melting point and then reflowing the solder by the temporary application of heat from an attached tungsten lamp. The estimated maximum temperature of the solder during reflow was 320 °C. The reflow time is the time during which the radiation from the tungsten lamp heats

the chip and carrier to above the melting point of the solder. This time was approximately 2.5 seconds; long enough for the solder to be liquid for a couple of seconds. The bonding force (the force that the die collet applies to the chip onto the carrier) was kept the same for all die bonds performed. Forming gas was used to reduce surface oxides for each die bond as well.

The die bonding procedure was similar for the slow cooling and rapid cooling experiments, except for the cooling time. The rapidly cooled samples after refreezing were immediately placed on an aluminum block at room temperature where they cooled to the ambient conditions in approximately one minute. The cooling rate for the rapid cooling process was approximately 300 °C/min. The slowly cooled samples after refreezing were transferred from the workholder assembly to an attached cooling bar. This cooling bar was a 38 cm long piece of aluminum, heated at one end to the temperature of the workholder assembly and unattached at the other end. The temperature profile along the length of the bar was a decreasing function of the distance from the hot end, the unattached end being at slightly above the room temperature. The slow cooled samples were moved along the bar over a period of 30 minutes. The samples were accelerated along the bar over that time such that they experienced a linear decrease in temperature to room temperature. The cooling rate for the slow cooling was approximately 10 °C/min, as in Fig. 4.1.

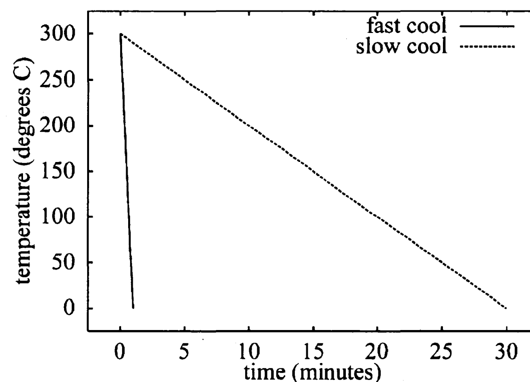

Fig. 4.1 Cooling profile for fast and slow cooling processes.

Once all of the lasers were die bonded p-side down, they were wire bonded on the n-side (facing up) to a metallized contact pad on the chip carrier. The die bonds were all relatively clean as observed with a microscope inspection. There were no solder balls protruding from the sides of the chips nor other visible problems with the die bonds. Pre-deposited solder on chip carriers tends to produce more consistent die bonds than using solder preforms.[43]

4.2.1 Strain

The strain on the facet of the diode lasers was measured using the degree of polarization of photoluminescence. The chips here were bonded to carriers with a solid solder layer, i.e. with no solder pattern. In the case of a semiconductor chip bonded uniformly in the x-z plane, $\varepsilon_{xx} > \varepsilon_{yy}$ (oriented as in Fig. 2.1). That is, the strain owing to die bonding and metallization in one direction results in strain in the orthogonal direction by general elasticity considerations. From the stiffness coefficients for InP, an infinite planar chip bonded to an infinite plane would result in ε_{yy} being approximately a third of ε_{xx}. For an actual chip and carrier the ratio of ε_{yy} to ε_{xx} would be less than this because of the boundary conditions on the finite sized chip. An approximation is then used that DOP $\approx -K_\varepsilon\varepsilon_{xx}$ and the measured DOP is approximately proportional to the x-direction strain for a uniformly bonded chip.

This experiment was primarily concerned with comparing the effect of cooling rates of the bonding procedure and not measuring absolute strain values. For this reason values of degree of polarization are compared as they are directly related to strain and so make for a valid comparison. The degree of polarization is a quantity that varies from -1 to $+1$. The measurements were made over the facet using a step size of 3.5 μm in both the horizontal and vertical directions.

Figure 4.2 shows false colour images of DOP (top) and ROP (bottom) data from an unbonded diode laser. Figures 4.3 and 4.4 show data for rapidly cooled and slowly cooled devices respectively. False colour images are used to map the DOP and ROP data to qualitatively display the information. In these images blue represents positive values, red are negative values, and green are neutral (zero) values of DOP and ROP. For the work in this thesis, all of the false colour maps are full-facet scans and so the images represent the full facet of a chip that was scanned using the DOP system. In other work using the system, small sections of laser material can be scanned at a high resolution but since die bonding induces strain that is widespread in a chip, the entire facets were scanned here.

These false colour images provide a view of the strain pattern owing to bonding, metallization, oxide layers, and crystal die damage from cleaving and handling. From the approximation that DOP $\approx -K_\varepsilon\varepsilon_{xx}$ and the false colour DOP images presented in Figs. 4.2-4.4, it is clear that there was a large compressive strain (blue) at the facet. This strain was caused by the die bonding procedure and also from the thick gold layer on the chip.

Fig. 4.3 False colour maps of DOP (top) and ROP (bottom) on facet of rapidly cooled diode laser.

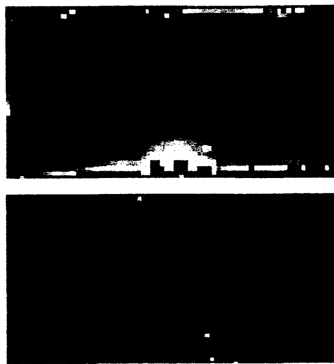

Fig. 4.4 False colour maps of DOP (top) and ROP (bottom) on facet of slowly cooled diode laser.

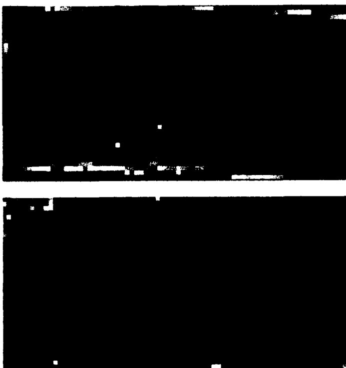

Fig. 4.2 False colour maps of DOP (top) and ROP (bottom) on facet of unbonded diode laser.

4.2.2 Thermal Impedance

The relative thermal impedance was measured using a simplified version of the method by Paoli.[44] This is a technique that measures the shift in wavelength due to a junction temperature change. The shift in wavelength due to the change in temperature in the active region was measured as a function of

applied current. A higher thermal impedance results in a higher active region temperature for increasing currents and that causes a greater wavelength shift. The output wavelengths of the bonded lasers were measured with an Agilent optical spectrum analyzer for each of a range of applied continuous wave currents. For each laser, optical output spectra were measured over a range of 100 mA of applied current, in 5 mA steps. From the compiled spectral information, the shift in wavelength as a function of applied current was calculated for each laser as a slope of peak wavelength versus current. This gives a relative measure of the thermal impedance. This is sufficient for comparing the two different bonding procedures, using lasers from the same wafer and like chip carriers. It does not give an absolute value of thermal impedance (in °C m^2W^{-1}) but it allows for a relative comparison of the thermal impedance of like semiconductor laser devices.

4.2.3 Surface Structure

To examine the difference in the surface of the exposed area of the solder, one carrier from each was scanned with an atomic force microscope (AFM). From these AFM scans the surface roughness was measured over a square area on the solder. The root mean square (rms) surface roughness over an area 150 × 150 μm^2 of the solder on the carriers was measured for each carrier.

4.2.4 Cross Sectional Structure

The solder material underneath the laser chips is what is important for the bonding properties of the lasers. To examine the bond underneath the chip, one sample each from the slowly and the rapidly cooled groups was cross sectioned. This was done to investigate the solder beneath the chip and away from the edge of the carrier. The two samples were mounted and encompassed in an adhesive compound and polished parallel to the facet using a fine grit diamond slurry. The resultant cross sections of the bonded lasers on the chip carriers were then analyzed. It would have been preferable to cross section a number of samples from each group but due to the difficulty of the procedure, it was only possible to get one sample cross sectioned from each group.

4.2.5 Cross Sectional Composition

The composition of the materials in the interface was determined with Auger electron spectroscopy (AES). The cross sectioned samples were briefly Ar ion sputtered to remove any oxides or other contaminants before AES analysis. AES line scans and selective area analyses were performed on the samples of the two bonding processes. The cross sectioning process and Ar ion sputtering left some artefacts on the sample since these processes are destructive.

4.2.6 Bond Strength

For examining the strength of the bonded chips, destructive shear tests were used. The lasers bonded onto chip carriers were placed in a shearing machine that exerts a measured force laterally on the chip while holding the carrier in place. A larger force indicates a stronger die attachment.

4.3 Results

In another study looking at cooling rates, various sized GaAs dice were bonded to diamond mounts using Au/Sn eutectic solder.[42] Some chips in that work were prone to cracking when cooled to room temperature in under one minute. Those which cracked were relatively large chips (from 2000 × 2000 × 410 to 10,000 × 10,000 × 410 (μm × μm × μm)) while chips smaller than these did not crack readily.[42] It may be that the high aspect ratio of the large chips resulted in a reduced fracture strength or perhaps the larger chips experienced greater thermal gradients as they were removed from heat. The chips in the experiment described here were considerably smaller, had a lower aspect ratio, and the carriers were better CTE matched. None of the lasers here showed any cracks upon cooling.

4.3.1 Strain

The degree of polarization, as defined in (2.10), is a quantity that can vary from -1 to $+1$. False colour image maps of DOP data help to show strain as a function of position. This makes it easier to visualize the strain and see the effects of the geometry and voids. Maps like in Figs. 4.2-4.4 provide a large amount of information which can make it difficult to compare one map to another. It is useful to have a figure of merit for comparison. One such figure of merit is an area average of DOP. This corresponds to strain over that region. In the course of handling diode laser chips before bonding, crystal damage can sometimes result which produces localized strain in the material. The strain fields and polarization effects in Figs. 4.2-4.4 near the edges are undesired in comparing the overall strain information. To prevent these from skewing the results of the different chips, the area shown in Fig. 4.5 was used to obtain a single average DOP value for each device. This sampling region was centred on the facet (over the ridge) and covered an area of $105 \times 70\ \mu m^2$. The DOP values for the rapidly cooled lasers, the slowly cooled lasers, and the unbonded lasers are shown in Fig. 4.6 and the mean values are given in Table 4.1. The standard deviations of the means are given in Table 4.1 for statistical comparison. From this aggregated data, the slow cooling bonding process seems to induce, on average, more strain than the rapid cooling process. Although there is a range of values for the DOP measurements for the rapid and slow cooled devices, the difference between them is statistically

significant. Using a one-tailed t-test it was found with more than 90% confidence that the slowly cooled samples were more strained than the rapidly cooled ones. The metallization on the bare laser chips caused a significant amount of strain in the chips. This is evident from the strain measurements of the unbonded samples. The slowly cooled process resulted, on average, in greater strain than the rapidly cooled process.

Table 4.1 Degree of polarization values.

TYPE OF BONDING	MEAN DOP	STANDARD DEVIATION OF MEAN
unbonded	0.00590	0.00052
rapidly cooled	0.00649	0.00065
slowly cooled	0.00750	0.00023

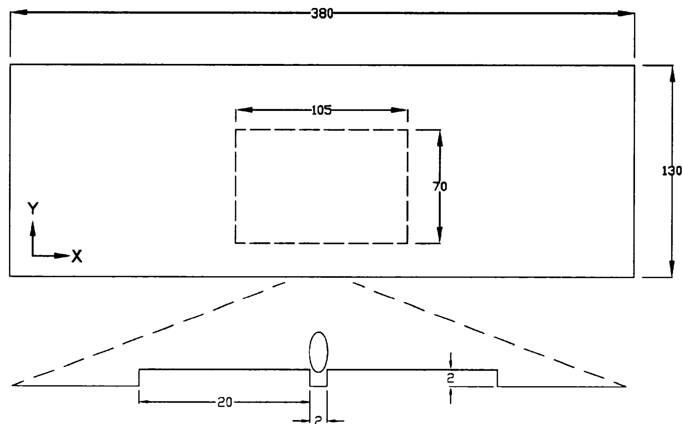

Fig. 4.5 Area of averaging for DOP and zoomed in section of ridge and trenches with illustrative spot drawn to show approximately where light is generated in the laser (dimensions in μm).

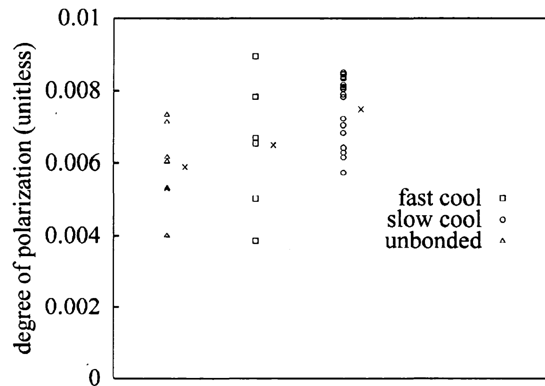

Fig. 4.6 DOP data for rapidly cooled, slowly cooled, and unbonded chips. The mean values for each are marked by an × to the right of each set of data.

4.3.2 Thermal Impedance

Using the modified Paoli method, there was a measurable difference in the thermal impedance between the slowly and rapidly cooled samples. In Fig. 4.7 there are data comparing the slopes of wavelength versus applied current for a slowly cooled and a rapidly cooled device. The larger slope for the slowly cooled device is an indicator of its relatively larger thermal impedance since the increase in junction temperature owing to a given applied current shifts the wavelength to a greater degree. For the slowly cooled devices the mean measure of the relative thermal impedance was 0.021 ± 0.001 (nm/mA, the unit of the slope of the wavelength versus applied current fit). In the case of the rapidly cooled devices, the mean measure of the relative thermal impedance was 0.018 ± 0.002 (nm/mA). Using a one-tailed t-test it was found with greater than 95% confidence that the slowly cooled samples had a higher relative thermal impedance than the rapidly cooled ones.

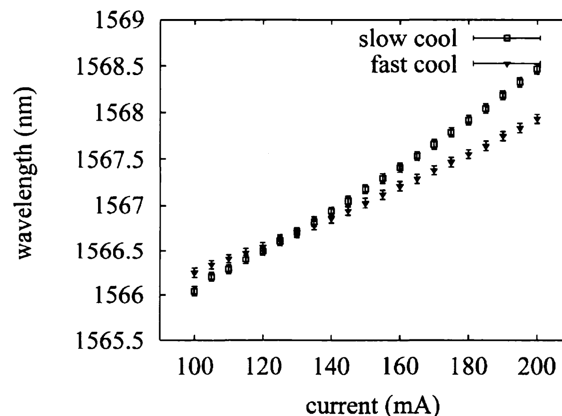

Fig. 4.7 Wavelength shift owing to temperature change for a range of applied currents for a slow cooled and fast cooled device. The slopes of these best fit lines are used as relative measures of the thermal impedance.

4.3.3 Surface Structure

The difference between the samples processed by the two cooling procedures was obvious even to the unaided eye when looking at the bonded chip carriers. The part of the solder strip that was exposed (not under the laser chip) was distinctly different in colour and texture. The rapidly cooled solder samples were shiny and white metallic coloured whereas the slowly cooled ones had a matte finish and were gold metallic coloured. From the AFM data the root mean square (rms) surface roughness was 250 nm for the rapidly cooled sample and 450 nm for the slowly cooled sample. The difference in the surface roughness of the solder can be seen in Fig. 4.8. These are AFM images that have been processed to show depth. The image (b) is the slowly cooled sample and it appears rougher than the rapidly cooled sample (a). There is clearly a difference in the surface structure of the solder for the two cooling procedures. The slowly cooled sample showed clumping of material into distinct islands. This may be due to metal migration while being cooled slowly. The rapidly cooled sample appeared more homogeneous, with less aggregation of material into surface bumps. This could be due to the smaller nucleation size and finer grains typical of rapid cooling. The gold colour on the slowly cooled solder surfaces indicates gold diffusion in the solder material and alloying due to the time and elevated temperature. This interdiffusion of the Au/Sn solder and Au layer on the chip has resulted in a different composition of the material on the carrier. The time and temperature have permitted larger grains to grow and amalgamate such that the surface is rougher.

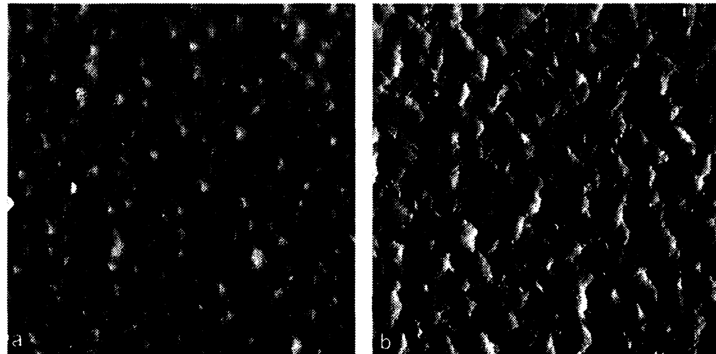

Fig. 4.8 AFM images of the surface of exposed solder on the chip carriers.
(a) rapidly cooled sample (b) slowly cooled sample
(image dimensions are 150 μm × 150 μm)

4.3.4 Cross Sectional Structure

Using an optical microscope and a scanning electron microscope (SEM), there appeared to be more voiding in the slowly cooled sample compared with the rapidly cooled sample. In the trenches around the ridge (see Fig. 4.5 for a schematic diagram) there were voids of around 2 μm in length in the rapidly cooled sample and up to 10 μm in length in the slowly cooled sample. Away from the ridge the bonding was better, as is visible in Fig. 4.9. The voids in the trenches are evident in Figs. 4.10 and 4.11. It is also apparent from Figs. 4.10 and 4.11 that the thick gold metallization on the laser chip conformed to the shape of the ridge and trenches. The gold acts as a heat spreader, an electrical conduit and to protect the ridge in a p-down bond. It is believed that during bonding, voids remained in the trenches as the solder did not contact well with the recessed metallization in the trenches. It is undesirable to have voids in the region near the ridge. In such a diode laser the current is channelled through the ridge to the active region where light is created within microns of the top of the ridge. Figure 4.5 shows where light is created in such a laser. Heat is also produced there and needs to be removed. Sometimes devices are bonded active region down to facilitate heat transfer away from the laser so voids there are particularly unwanted. These lasers were bonded in a production environment and the voids near the active region were an unfortunate result. This was the result using devices from a standardized production bonding process at a major optoelectronics manufacturer.

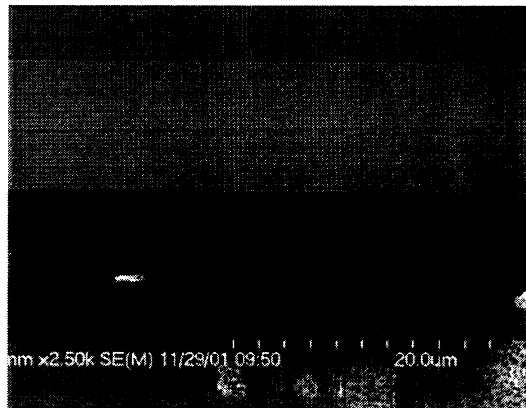

Fig. 4.9 SEM image of bonding interface away from the ridge.

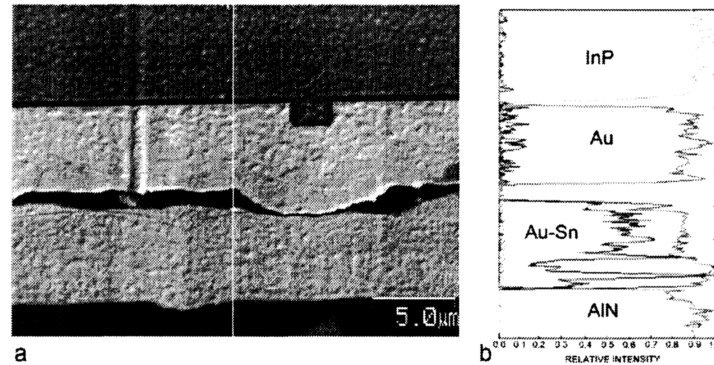

Fig. 4.10 AES line scan across bond interface for slowly cooled device.
(a) location of scan (b) AES results along scan line

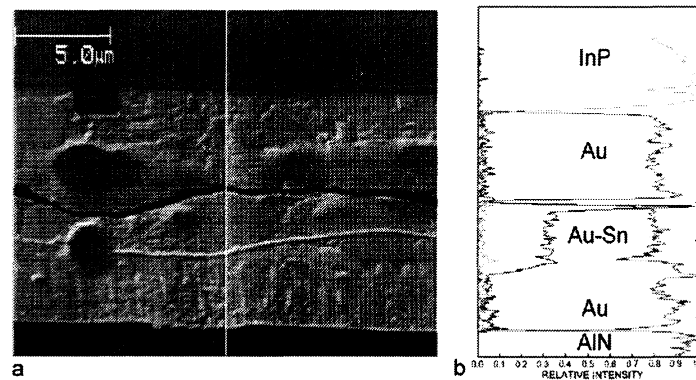

Fig. 4.11 AES line scan across bond interface for rapidly cooled device.
(a) location of scan (b) AES results along scan line

That the thermal impedance was greater for the slowly cooled sample is consistent with the voiding in the trenches. The sample with more voiding near the ridge would be expected to have a poorer thermal path, hence a larger thermal impedance. Since the current is driven through the ridge, bonding in this region is important. In the rapidly cooled device there was a microstructure visible in the solder with a clear separation of phases. This was not seen in the slowly cooled device where the solder and carrier metallization appear homogeneous. The optical microscope images of the cross sections across the entire chip showed that there were voids in the solder in the trenches around the ridge, but better bonding elsewhere. The bonding away from this region, that is, elsewhere across the rest of the width of the chip was with far fewer voids, as in Fig. 4.9. It is not understood how the cooling rate could affect the voiding in the solder since voids occur from poor wetting while the solder is liquid. From the experiment it was shown that

the thermal impedance was higher in the slowly cooled samples. Voids in the solder would explain this but it is uncertain why voids should be greater in the slow cooled sample. Since only two samples could be cross sectioned it is not known if voiding was, in general, greater in the slowly cooled devices.

4.3.5 Cross Sectional Composition

Figure 4.10 shows an AES line scan for a magnified area near the ridge of the slowly cooled sample. In (a) the vertical line in the centre shows where the scan was performed across the bonding interface on the slowly cooled sample. In (b) the corresponding AES relative composition intensities for this line scan are shown with the materials labelled. Figure 4.11 is an AES line scan for the rapidly cooled sample. The results of the AES analysis show that there is a difference in the distribution of material between the slowly and rapidly cooled samples. The Au/Sn solder appears to be more alloyed with the Au metallization of the carrier in the slowly cooled sample, as in Fig. 4.10.b. The Au from the carrier metallization has interdiffused with the solder material. From the selective area scans there also appears to be some penetration of Au into the AlN carrier material in the slowly cooled case. The rapidly cooled sample in Fig. 4.11 shows a more distinct separation of the layers and little alloying of the Au/Sn and Au layers. The slow cool process clearly had an effect on the metallurgy of the bond. It seems to have enhanced metallurgical processes such as solid state diffusion and alloying.

4.3.6 Bond Strength

The chips were sheared from the chip carriers and the shear values were fairly scattered. The mean force required to shear the slowly cooled devices was lower than the mean force for the rapidly cooled ones, on average. The shear test data was found to be correlated with the strain data. A linear correlation coefficient of 0.77 was calculated between the shear data and the strain data. For the number of sample points the probability of obtaining a larger correlation coefficient from random observations taken from an uncorrelated parent population is 0.0001.[45] That is to say, it is highly likely that the strain and shear measurements are correlated for the samples. This is an expected result.

Common to all of the devices was the remaining solder after shearing off the chip. The solder showed poor wetting near the ridge. Perhaps a larger bonding force or a longer reflow time is required for these p-down die bonds. The shape of the chip surface around the ridge and the conformal nature of the metallization might make it more difficult for wetting to occur in that region and might necessitate pressing it harder into the molten solder to achieve contact and better wetting there.

4.4 Discussion

The different cooling rates resulted in differences, on average, in a number of properties of the die bonds. The solder of the slowly cooled samples had a structure that was different than the solder of the rapidly cooled samples as seen in the AFM scans and cross sections. During the slow cooling process the solder and the metal layers on the laser chip and on the chip carrier were held at an elevated temperature for an extended time. Relative to the rapid cooling process this may have permitted more metallurgical processes such as alloying and solid state diffusion to occur. This 'annealing' might explain the surface roughness since the extra time and energy available to the slowly cooled samples might have allowed migration and diffusion processes to occur more readily.

From the AFM map of the rapidly cooled sample, it appeared to be more like it was frozen directly from a melted state. Its surface structure seemed to be much finer and smoother than that of the slowly cooled device. The microstructure of the rapidly cooled sample showed distinct phases in the solder. This is similar to the difference between fast and slow cooling of other solders such as Pb-Sn and Sn-Ag.[46] With Pb-Sn alloys it has been found that slow cooled samples result in a lamellar microstructure of alternate layers of lead-rich and tin-rich phases. In rapidly cooled samples, a much finer microstructure made of spheroidal phases exists. It is believed that the physical structure of the slowly cooled solder was the likely cause of the difference in thermal impedance. The pores and bumps of the slowly cooled solder and the resultant voiding correlated with the higher thermal impedance found in these samples. The relatively smooth solder in the rapidly cooled samples, with fewer and smaller voids, resulted in a better path to remove heat, hence a lower thermal impedance. It is not, however, understood how voiding of the solder underneath the chip could be related to the cooling rate. No mechanism that could explain how the cooling rate could affect voiding in the solder underneath the chip was found.

From the AES data, the time and elevated temperature seemed to cause alloying of Au from the carrier metallization into the Au-Sn solder in the slowly cooled case. The material in the rapidly cooled samples showed a more distinct line in the composition of the solder and the metallization layers. Since the chip and carrier metallizations showed little interdiffusion with the solder in the rapid cooling process, compared with the slow cooling process, it might be expected that there would be differences in the physical properties between the two cases. The physical properties of the materials depend on the composition of the alloys and the presence of any intermetallic compounds. There exist intermetallic compounds of Au and Sn that have significantly different properties than the eutectic alloy.[40]

The eutectic point for 80/20 weight percent Au/Sn solder is approximately 278 °C. In considering the phase diagram of the Au-Sn binary system, the slope of the liquidus on the Au-rich side of the eutectic point is quite steep.[47] When

heat is applied to melt the solder, gold from the carrier and the chip metallizations may partially melt and diffuse into the solder, changing its composition from 80/20 and raising the freezing point from the eutectic point. Any free Sn will melt first because of its lower melting point and dissolve available Au into it. The bonding procedure was equivalent for the two bonding processes until after freezing. At the point of freezing, the samples for the two processes should be identical. Any additional alloying or solid state diffusion of Au into the Au/Sn solder could alter the properties of the bond. Additional Au in the Au/Sn solder joint could have changed the coefficient of thermal expansion and elastic properties of the alloy.

Table 4.2 Physical Properties of Au-Sn Metals and Phases.[40][48]

MATERIAL	MODULUS OF ELASTICITY (GPa)	POISSON'S RATIO (no unit)	COEFFICIENT OF THERMAL EXPANSION ($\times 10^{-6} K^{-1}$)
Au	77	0.42	14.2
Sn	42	0.33	23.8
Au-Sn eutectic	68	0.405	16.2
Au-Sn zeta phase	58	0.41	17.8

Ideally the pre-deposited solder would melt and refreeze at its eutectic composition such that the freezing point would be at its lowest (278 °C). During the reflow time it is possible that some gold could dissolve into the solder, changing its composition. If the slow cool process facilitated more gold to enter into the solder, then phases other than the eutectic composition might have been created. The alloy of Au and Sn has a relatively complicated phase diagram for a binary system, with a number of intermetallic compounds. As seen in Table 4.2 the physical properties are different for different phases. The zeta phase, for example, has a higher gold content than the eutectic point and its coefficient of thermal expansion (CTE) is slightly higher as well. It is possible that some part of the solder that was gold enriched through the slow cool process in the slowly cooled samples had a higher CTE than the rapidly cooled samples. Since the CTE for the InP chip and the AlN carrier, are both around the same then any higher CTE value for the solder would induce thermal strain in them. This might explain why the slowly cooled samples were strained more than the rapidly cooled samples. However, the CTE mismatch could be offset somewhat if the gold rich material has a lower modulus of elasticity thus allowing some elastic strain relief.

4.5 Summary

It has been shown that there was a difference, on average, in the properties of die bonds of diode lasers owing to the cooling rate of the die bonding process. Rapidly cooled Au-Sn solder samples showed physical differences from slowly cooled samples. In the samples examined, the rapidly cooled solder was smoother in texture and showed less voiding than the slowly cooled solder. Since only a couple of samples were cross sectioned, the voiding observed is not necessarily representative of the rest of the samples. The slowly cooled samples were found, on average, to have a higher thermal impedance. In measurements of strain it was found, on average, that the slowly cooled lasers were more strained than the rapidly cooled ones. The extra time at an elevated temperature in the slowly cooled samples might have facilitated gold diffusion into the solder, changing its composition and altering its physical properties, including its coefficient of thermal expansion.

Although forming gas was used, consistent with standard die bonding procedures, the solder joints were weaker than desired for the bonding area of the chips. While this was not a welcome result, it did occur using chips and carriers die bonded in a production environment. Perhaps the use of a flux or larger bonding force would have shown different results. The profile of the chip's p-down bonding surface with the ridge and trenches appears to have made it difficult to achieve good wetting and prevent voids in that important region.

The procedure of die bonding is often neglected relative to the overall design of a diode laser, despite its importance in mechanical, electrical and thermal duties and the sizable portion of overall cost that packaging consumes. The choice of cooling rate could also have an influence on the design of the laser die and chip carrier metallizations, for example with any metallic barrier layers to be included to control or impede diffusion. The cooling rate is one variable in the die bonding process that should be considered carefully since it could have implications on the properties of the bond and potentially the laser design.

CHAPTER 5 - PRE-DEPOSITED SOLDER

5.1 Introduction

As part of the evolution of packaging optoelectronics, the introduction of pre-deposited solder on carriers or chips has yielded some significant improvements in the precision of diode laser die bonds. By depositing the solder as a film onto a carrier or chip it has become possible to design relatively complex die attachments. For example, it is now possible to deposit solder onto a small, designated area of a carrier and this can result in far more controlled die bonding than using other forms of solder. In addition, the composition of the bond can, in principle, be controlled quite carefully by the judicious choice of metallization layers around the deposited solder. The experiments in this chapter were an attempt to measure the effects of changing a few die bond parameters and die bonding procedures using the degree of polarization of photoluminescence. The carriers that were used in the experiments were pre-deposited with solder. In section 5.2 a pair of experiments describe on the effect of reflow time and of reflow temperature on die bonds. In section 5.3 an experiment is explained that explored the effect of carrier metallization on die bonding.

5.2 Reflow Time and Temperature

Two sets of experiments were undertaken to understand the effect of reflow parameters on the die bonding of diode lasers: the reflow time and the reflow temperature. It was desired to see if the effect of altering these parameters could be observed in DOP measurements of the bonded chips. The reflow time is defined here as the time that, after heat is applied to a chip and carrier, the solder is above its melting point. The reflow temperature is defined here as the maximum temperature reached by the die bonding assembly during reflow, as measured by a thermocouple near the heating element.

5.2.1 Experiment

The experiments were carried out using two separate automated robotic die bonding machines of the same model, Palomar Technologies 3500-II Automatic Bonders. The control of the temperature is achieved on these machines by the amount of current that is applied to a heating element and the length of time that it is on. Although two sets of experiments were conducted, one for reflow time and one for reflow temperature, the two parameters are not quite independent. To achieve a higher reflow temperature, more current is applied but also for a longer time to reach the higher temperature. A typical temperature profile over time from one of these bonding machines is shown in Fig. 5.1 as recorded on a strip-chart temperature recorder. In the figure it is clear that there is a time lag from when the current is applied to when the thermocouple

reaches the maximum temperature. There is also a time required for the assembly to cool once the current is removed. So if a higher reflow temperature is required, the assembly will be above the melting point of the solder for a longer time. The reflow time and reflow temperature are indicated on this plot as "+" and "×" respectively. Ideally, if the assembly could be heated and cooled instantaneously the time-temperature curve would form a square wave shape and the time and temperature could be de-coupled since the magnitude and length would be independent.

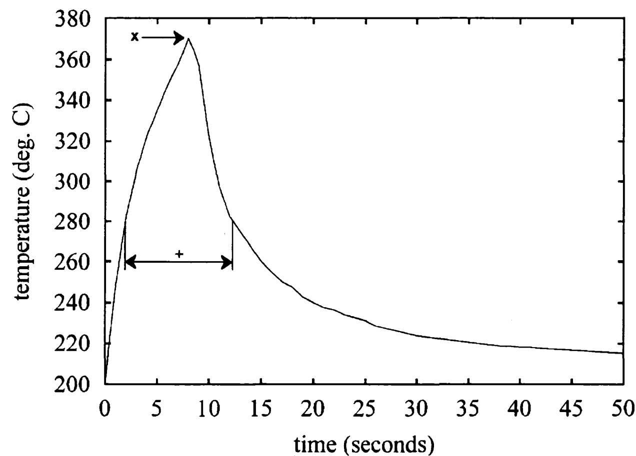

Fig. 5.1 Typical temperature profile over time during die bonding with automated machine, measured on a strip-chart recorder. The reflow temperature is designated by "×" and the reflow time is designated by "+" in the figure.

For these experiments, InP-based diode lasers were used for die bonding. They were bonded to silicon chip carriers with 80/20 Au/Sn solder, using forming gas. The solder was up to 3.5 μm thick, pre-deposited on top of a 0.2 μm Pd layer. The solder was patterned on each carrier such that there were pads for mechanical attachment on either side of a centre stripe that was for electrical contact with the device. This is seen in the representative diagram of the pattern in Fig. 5.2. The centre stripe is 40 μm wide and 284 μm long. The dimensions of the corner pads for mechanical attachment are 106 μm by 107 μm. The diode lasers had a contact metallization pattern, 2.5 μm thick, that essentially matched the pattern of the solder. The placement accuracy of the automated machine was rated to be ± 12.7 μm but the actual accuracy was found to be slightly better than this. The positioning resolution of the robotic arm and die tool was between 0.5 μm and 0.6 μm in the three direction axes while the repeatability was between ± 0.3 μm and ± 0.5 μm. Other factors involved in placement accuracy include the rotational precision of the pickup tool and the pattern recognition capabilities of the automated system. The contact mass of the arm and chip on the carrier was 35

grams. The workholder assembly on which the carrier is placed was held at 200 ° C as a pre-heat, so that the reflow essentially meant heating the assembly the rest of the way to above the melting point of the solder.

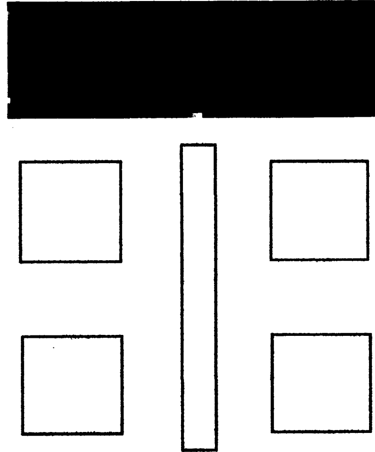

Fig. 5.2 Map of DOP scan (top) for the facet of an unbonded chip aligned with a diagram (bottom) that is representative of the matching metallization pattern on the bottom of the chip.

In the reflow time experiment three reflow times were used: 0 seconds, 5 seconds, and 10 seconds. These are the lengths of time that the chip and carrier assembly were held above 280 ° C. For the 0 second set, the temperature was just allowed to hit the maximum temperature momentarily. For the 5 and 10 second sets, the chip and carrier were above 280 ° C for 5 and 10 seconds respectively. Their reflow temperatures each went higher than 300 ° C. 49 devices were used for the experiment and the break-down is shown in Table 5.1.

Table 5.1 Breakdown of number of devices in each experiments.

REFLOW TIMES	NUMBER OF DEVICES
0 ± 1 s	15
5 ± 1 s	17
10 ± 1 s	17
REFLOW TEMPERATURES	
320 ± 10 ° C	10
360 ± 10 ° C	10
410 ± 10 ° C	8

The chips were die bonded p-side down on the carriers. The matching contact metallization of the chip and solder pattern of the carrier were aligned to the best accuracy possible of the machine. After die bonding, each of the bonded laser chips was scanned using the DOP setup to observe the strain induced in the chips

by the bonding. The facets were mapped using a step size of 5 μm in both directions. 12 chips were left unbonded and were scanned using the DOP system to determine the strain in unbonded chips.

For the reflow temperature experiment three reflow temperatures were planned: 300 ° C, 350 ° C, and 400 ° C. The actual temperatures were somewhat different from these owing to overshooting in the heating. 28 devices were bonded for this experiment and the breakdown of these is in Table 5.1. Similar silicon carriers and InP-based diode lasers were used as in the reflow time experiment. However, two different automated machines were used for the two experiments. Their specifications and stated tolerances were the same. After die bonding, the facet of each bonded laser chip was mapped using the DOP measurement setup. Following this, the chips of the reflow temperature experiment were sheared from their carriers using a die shear test machine (a destructive test). The machine used was a Dage Series 4000 Bondtest machine calibrated with a tolerance of ± 625 mg. This is a device used to test the strength of a die bond by applying a lateral force onto the bonded chip until it is sheared off the carrier. The force required to shear a chip gives a figure of merit for the strength of the bond. It is not an exact measure of the strength, however, since the modes of failure differ (a chip can shear off a carrier relatively cleanly if the failure is the bond or be shattered if the failure is in the chip itself). The chips in the reflow time experiment were not shear tested.

5.2.2 Results

The results of the DOP measurements showed a range of patterns for the chips owing to the die bonding strain. The unbonded chips that were mapped using the DOP system provided a control group for the bonding strain determination. These chips were found to be strained somewhat by the effects of the contact metallization. This is seen in Fig. 5.2. The four corner pads for mechanical attachment and single stripe for electrical and thermal contact correspond to the blue areas at the bottom of the facet in the DOP map.

The DOP and ROP maps of the bonded chips, both from the reflow time and reflow temperature experiments, revealed complex patterns with positive and negative lobes in different areas. Since the chips were not bonded uniformly in a plane, as in Section 4.2, it is not appropriate to use an approximation of the DOP being proportional to one component of strain as was done there. This is because the boundary conditions are more complicated on the chip because of the solder pattern. Because of these intricate patterns it was hard to compare them with one another and difficult to quantify the bonding strain overall. Using the DOP measurements, averages of DOP over the entire facet were computed for each device. These average DOP values are shown in Table 5.2. The data are scattered and there was no conclusive evidence of a difference between the three reflow times or between the three reflow temperatures. Area averages over smaller sections of the facets were computed and similarly no statistically significant differences were found. The shear test data for the reflow temperature experiment also did not demonstrate a clear difference between the three cases. Table 5.2 shows the mean shear values measured of these devices. There is not a statistically significant difference between the average shear values of the three reflow temperatures.

Table 5.2 Average DOP measurements and shear test data of bonded chips.

	MEAN DOP (%)	STANDARD DEVIATION OF MEAN DOP	MEAN SHEAR FORCE (g)	STANDARD DEVIATION OF MEAN SHEAR FORCE
0 s reflow time	-0.678	0.249	--	--
5 s reflow time	-0.411	0.264	--	--
10 s reflow time	-0.656	0.251	--	--
300 ° C reflow temperature	0.120	0.231	129.4	16.6
350 ° C reflow temperature	0.210	0.211	132.1	22.4
400 ° C reflow temperature	0.175	0.202	146.6	31.3

Examples of DOP and ROP maps for each case are shown in Figs. 5.3 and 5.4 for the reflow temperature and reflow time experiments, respectively. The

maps show features unique to each chip. There does not appear to be a distinguishable collective difference, between the three groups, within the two experiments. That is, for each experiment it was not possible to differentiate between the three groups. However, between the two experiments there was a definite difference in the DOP and ROP maps. Comparing the chips bonded in the reflow time experiment with the ones bonded in the reflow temperature experiment it is clear that the maps of the two experiments are different. The maps in Fig. 5.4 for the reflow time experiment show greater values of DOP and ROP, which are visible as larger lobes with grey sections indicating off-scale values in the false colour scheme.

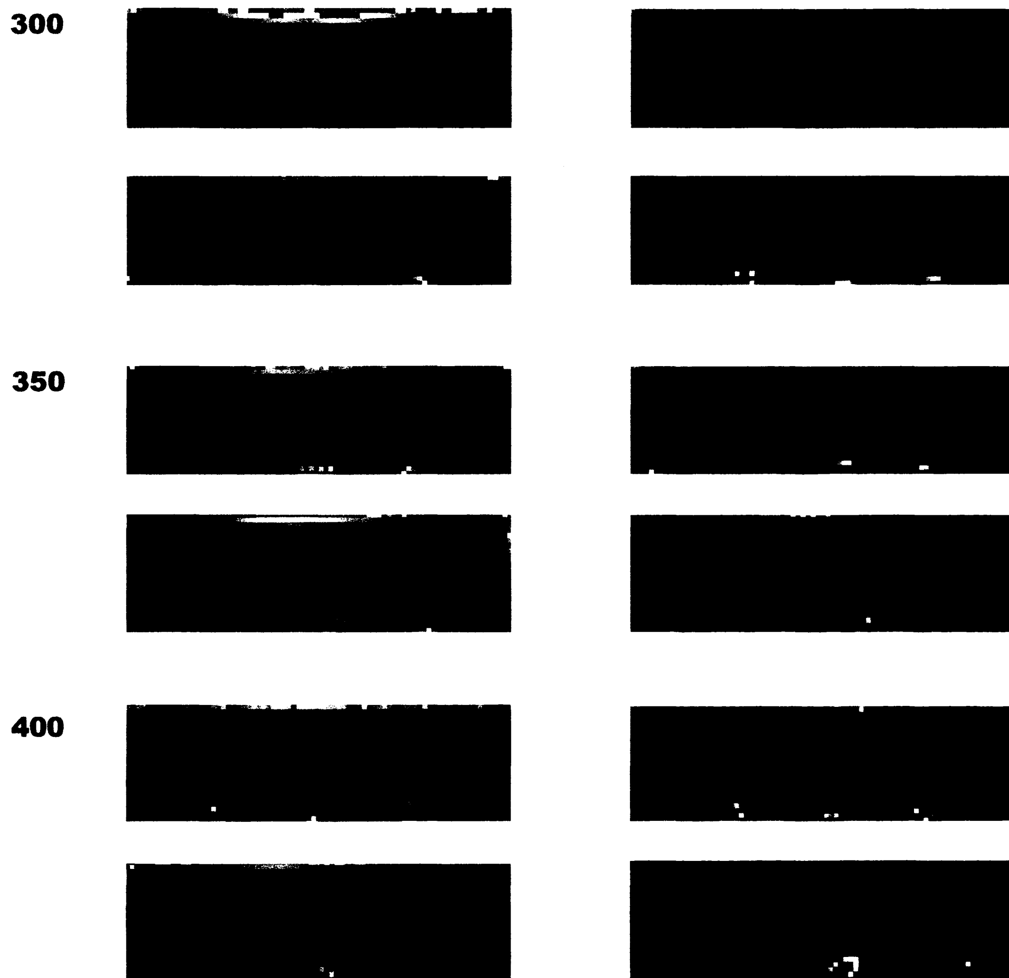

Fig. 5.3 DOP (left column) and ROP (right column) maps from the reflow temperature experiment. Two pairs of maps for each of the reflow temperatures: 300° C (top), 350° C (middle), and 400° C (bottom).

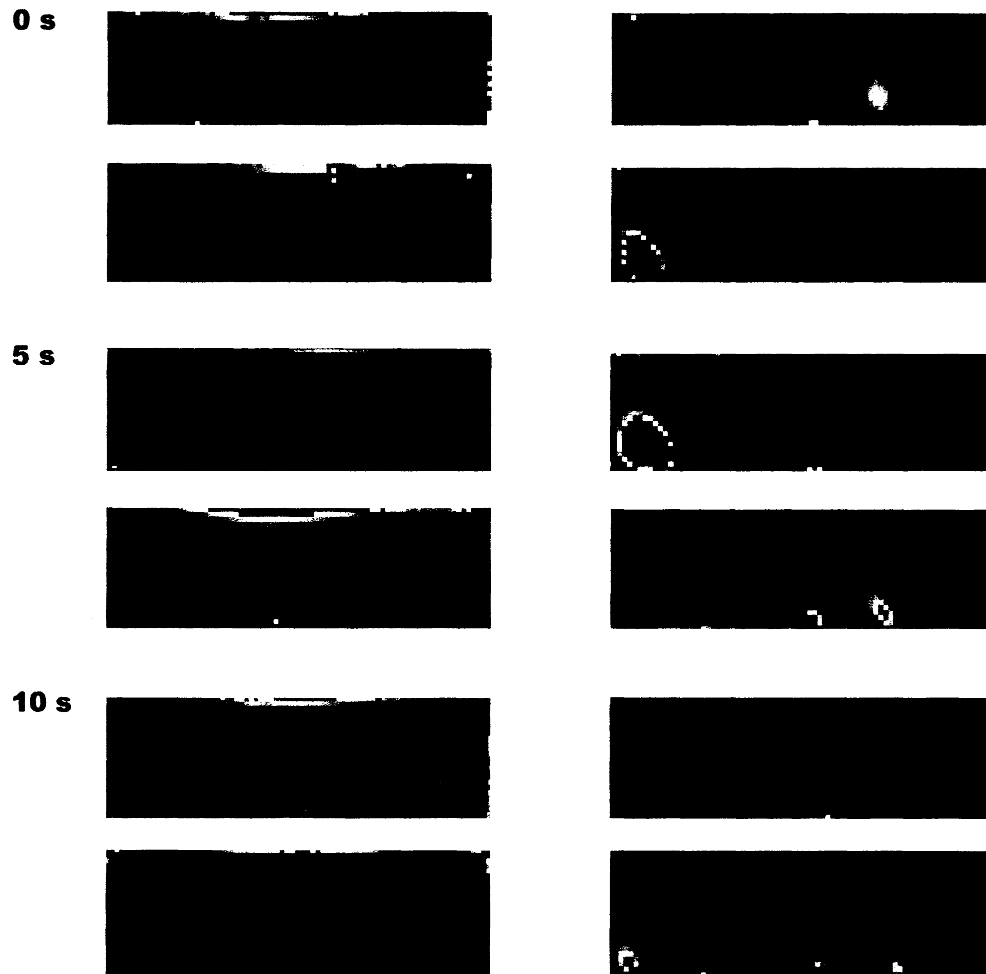

Fig. 5.4 DOP (left column) and ROP (right column) maps from the reflow time experiment. Two pairs of maps for each of the reflow times: 0 s (top), 5 s (middle), and 10 s (bottom).

5.2.3 Discussion

Despite the fact that there were not statistically significant differences found between the three reflow times and between the three reflow temperatures, there were differences found in the DOP maps in the chips of the two experiments. The magnitudes of the mean DOP values of the chips in the reflow time experiment are greater than those in the reflow temperature experiment as in Table 5.2. This is visible in the example chips in Figs. 5.3 and 5.4. It is believed that this difference owes to the different die bonding machines used for each experiment. The two experiments were carried out under similar conditions but with different die bonders of the same make and model.

Looking at the second and third DOP maps in Fig. 5.4 (second and third from the top in the left column) there are significant areas of negative DOP on the left sides of these maps. These are the large, dark grey lobes on the left sides (dark grey is the colour of negative off-scale values). There were many other maps in the reflow time experiment that showed this. The greater negative DOP on the left sides of these maps is indicative of better (stronger) bonding on that side compared with the right. This could be due to a misaligned vacuum pickup (the tool used to place the chip on the carrier during bonding). There seem to have been issues with the placement accuracy (arm placement or tool angle) in the machine used for the reflow time experiment. The chips and carriers for both experiments were picked from the same batch so there is no reason to suspect that they are the cause of the differences noticed. The only known difference between the experiments was the die bonder used. This shows how DOP and ROP measurements can be used to find differences in die bonds in characterizing die bonding procedures. Whereas the bonding conditions in the two experiments were thought to be the same, clearly there were differences in the bonds.

The variations in the DOP and ROP measurements of the bonded chips in these experiments has shown that reproducibility of this bonding was inconsistent. This is because of the solder pattern and the placement tolerances required. Since the placement accuracy of the bonding machine is approximately ± 10 μm and the width of the centre stripe is 40 μm there is the potential for problems with misalignment. It was found in a number of bonds that solder balls formed. Solder balls are approximately spherical protrusions of solder out from under a chip. They can block output light if they occur near the area of emission of a laser. Solder balls result from a lack of wetting of the solder onto the chip. Suppose the metallization pattern of a chip was misaligned sideways with the solder pattern of a carrier. There would then be an area of the solder without any surface to wet (the area of oxide on a chip is not wettable by solder since solder does not adhere to it). When pressure is applied to the chip and the temperature is raised, this solder will be repelled by the oxide area and be displaced out from under the chip. This displaced material would then form spherical outgrowths of excess solder. Solder balls were observed to occur in many of the bonds in the reflow time

experiment. Poor wetting could occur as well from oxidation on the surface of the solder, prior to bonding since surface oxidation reduces the wettability of the solder.

The solder used with these carriers was Au-Sn on a Pd layer. The expectation of the experiments was that there would be measurable differences in the DOP values between the three reflow times and between the three reflow temperatures. The hypothesis was that the extended time and temperature would result in gold from the chip metallization melting into the solder, changing its composition. The increased gold content would then cause premature freezing which would manifest itself as higher thermal strain upon cooling and greater measured DOP. The Pd layer may have limited this from happening to some extent. Pd, as a noble metal, can be used to protect solder from oxidation during bonding.[49] Here, Pd was used as a wetting layer beneath the solder to assist its wetting and adhesion to the carrier. Au and Pd are completely miscible in one another over all compositions and pure Pd has a higher melting point than pure Au, resulting in an increasing solidus with increasing Pd content in the binary phase diagram. However, Pd forms many intermetallic compounds with Sn and the Pd-Sn phase diagram is quite intricate.[47] If the Pd dissolved sufficiently quickly into the solder and diffused throughout, intermetallic compounds of Pd and Sn could have formed, and such material could have acted as a diffusion barrier to Au from the chip. This could have limited the diffusion of Au from the chip into the solder. It was found that the Pd did dissolve noticeably in the Au/Sn during reflow using AES analysis.[50] The dissolved Pd would have intermixed with the Au readily and formed intermetallics with the Sn. The composition of the ternary alloy was determined to be 24% : 37% : 37% (atomic percent) Pd:Au:Sn. There was also 2% oxygen.

That the average DOP values did not demonstrate a statistically significant difference between the reflow times and between the reflow temperatures perhaps indicates that there was not premature freezing from the Au of the chip, as had been expected. It may also be that premature freezing did occur but since it was only a shift of tens of degrees Celsius, it was not observed amidst the unevenness in the DOP and ROP maps.

5.3 Carrier Metallization

With pre-deposited solder on carriers, it is possible to tailor the solder composition for die bonding specific applications. This can include specifying the components of the solder layer as well as the metallization schemes below and on top of the solder. The purpose of this is to carefully control the composition of the solder so that it can be made closest to the eutectic point. The experiment detailed in this section was an attempt to use the DOP technique to measure differences in bonding strain owing to different metallization schemes. Three carrier designs were tested, with different solder composition and barrier metallizations.

5.3.1 Experiment

The experiment was carried out to see if strain measurements (using the DOP method) could detect the difference in carriers with different metallization schemes. Carriers with three solder and metallization designs were used, as in Table 5.3.

Table 5.3 Carriers designed for use in carrier metallization experiment.

	CARRIER A	CARRIER B	CARRIER C
solder	3.5 μm 80/20 Au/Sn	3.5 μm 80/20 Au/Sn	3.5 μm 70/30 Au/Sn
barrier layer	--	0.2 μm Pt	0.2 μm Pt
wetting layer	1.0 μm Au	1.0 μm Au	1.0 μm Au
adhesion and barrier layers	Pt/Ti	Pt/Ti	Pt/Ti
carrier	AlN	AlN	AlN

The Au/Sn solder layer was created by using a co-deposited technique (i.e. the Au and Sn are deposited at the same time rather than with alternating layers). The purpose of the bottom Au layer on the adhesion (Ti) and barrier (bottom Pt) layers was to facilitate wetting on the carrier by the solder. The composition of the solder, as deposited, would be expected to be altered by this Au during reflow. The 0.2 μm Pt barrier layer in the B and C carriers was meant to impede Au from the bottom of the carrier from melting into the Au/Sn solder and changing the composition during reflow. Higher Au content in the Au/Sn could result in premature freezing of the solder during reflow. If the solder froze sooner, i.e., at a higher temperature, then greater thermal strain would result and might be observable as higher DOP.

10 carriers from each of the A, B, and C carriers were die bonded using InP based diode lasers. An automated Palomar Technologies bonder was used for die bonding, with forming gas to limit oxidation of the materials. The carriers had a solder pattern similar to the one shown in the previous section. After bonding, the lasers were scanned with the degree of polarization of photoluminescence

system to produce DOP and ROP maps of the facets of each of the 30 chips bonded.

5.3.2 Results

The DOP and ROP maps showed patterns similar to those found in the reflow time and reflow temperature experiment. The uneven DOP and ROP patterns were due to the solder and metallization pattern, like in the previous chapter. The absolute magnitudes of the DOP values observed here were similar to those in the reflow temperature experiment and less than those of the reflow time experiment. DOP values, averaged over the whole facet for each carrier type, are shown in Table 5.4.

Table 5.4 Average degree of polarization values for the three carriers.

CARRIER	NUMBER OF CARRIERS	MEAN DOP (%)	STANDARD DEVIATION OF MEAN
A	10	0.198	0.067
B	10	0.227	0.114
C	10	0.205	0.086

From this information it is not possible to conclude any difference between the three cases. Within experimental error, the mean DOP values are equivalent. The DOP and ROP maps for all 30 devices measured seemed to be fairly consistent. There were not the myriad of patterns as seen in the previous section. In Fig. 5.5 there is a sampling of the DOP and ROP maps for two of each of the types of carriers used. They are quite similar.

Fig. 5.5 DOP (left column) and ROP (right column) maps from the carrier metallization experiment. Two pairs of maps for each of the three carrier types: A (top), B (middle), and C (bottom).

5.3.3 Discussion

The DOP and ROP data did not show a measurable difference between the three metallization schemes. Under the bonding conditions for this experiment the reflow temperature was estimated to be around 320° C (no strip chart recorder was used here). It may be that some Au did dissolve more readily in the A carriers than in the B and C carriers but this was not noticeable from the DOP and ROP data since the premature freezing might have only been by a few degrees C.

The C carriers were supposed to have a composition of 70/30 Au/Sn. The purpose of having a relatively higher Sn content was in the expectation of Au from the chip metallization melting into the solder and making the final composition nearly eutectic. Since no difference in DOP measurements was observed it may be that the composition of the solder on the three carriers was not as designed. Using Auger Electron Spectroscopy (AES) analysis, it was later found that carriers B and C both seemed to have compositions of 70/30 Au/Sn (as deposited and after reflow), which suggests that the B carriers were not manufactured to specification. Whether the method of using DOP to observe premature freezing is not sensitive enough or there were no differences to observe, this experiment resulted in no conclusion.

5.4 Summary

These experiments showed that there were differences between chips in die bonding, even with materials from the same source. It was not found that there were differences between the three reflow times and the three reflow temperatures as had been expected. As well, there were clear differences in the bonding between the two experiments because they were bonded with different automatic machines. The manifold variances in the DOP and ROP measurements provided motivation for other work, the finite element method fitting code. From the DOP and ROP maps alone it was not straightforward to understand what caused the shapes of the patterns observed. A tool was needed to understand and provide quantitative strain data using the available information. This is explained in Chapters 7 and 8 and features of some of the DOP and ROP maps from these experiments will be shown there.

In each of these experiments the DOP method was used to determine the strain in bonded diode lasers. As described the outcomes of all three experiments were null results as per the planned experiments and the hypotheses. However, the results showed other consequences not foreseen. The range of DOP and ROP patterns was quite large and this provided motivation for the development of other tools to get more out of the DOP and ROP data as will be explained later.

CHAPTER 6 - STRESS RELAXATION IN DIE BONDS

6.1 Introduction

Die bonding strain in a diode laser is the elastic deformation of the chip owing to the thermal stress in the bond. It is believed that the thermal stress that builds up in the solder joint as the bonded device is cooled from the solder melting point can result, after some time, in plastic deformation in the solder and relax the stress. If this is so then stress relaxation in diode laser die bonds could be observed by the resulting change in strain in the laser chips. The plastic deformation of the solder bonds owing to the thermal stress would lower the strain in the semiconductor chip and this could be observed by measuring the degree of polarization of photoluminescence in the chips. This was examined using lasers from a long term device reliability aging investigation (the diode laser aging study was conducted by Samuel K.K. Lam).

6.2 Procedure

The diode lasers measured in this study were part of a larger long term reliability experiment. A number of devices were driven at a raised current level and kept at an elevated temperature to accelerate the effects of aging on the devices; the diode lasers were operated at a temperature of 150° C and a current level of 150 mA. At various times of aging, the lasers were removed to perform tests on them. One of the tests was DOP scanning of the front facet and DOP maps were generated for each device in the study at each of a number of times during aging. The degree of polarization system shown in Fig. 2.2 was used for these measurements. DOP scanning was performed before the aging began and at each of the aging stoppages. The times of the measurements during the aging were: 0 hours, 22 hours, 44 hours, 132 hours, 447 hours, 1041 hours and 2074 hours. These lengths of time represent the duration since the beginning of the accelerated aging that the devices were at the elevated temperature and driven at the high current level. They do not include the time in between aging during which the devices were tested non-destructively in several ways, including DOP mapping. The total number of devices to survive aging to at least 1041 hours was 19. Of these, 15 survived aging to 2074 hours. The lasers were mounted p-side up with Au/Sn preform solder on a sub-mount which was affixed to an AlN carrier.

6.3 Results

Figure 6.1 shows the DOP and ROP maps for one particular device at each measuring time: 0, 22, 44, 132, 447, 1041, and 2074 hours. This device is representative of what was observed in the others during the study. The time "zero" for the experiment is the beginning of the accelerated aging study. It is

likely that initial relaxation of many days or weeks would have already occurred by the time the first DOP measurements were made at time "zero." To quantify the changes in these maps, an area of DOP was averaged for each map to get a value of DOP for comparison over the aging time. The area averaged was about 10% of the total area of the facet, and was centered horizontally and was below the center vertically to get an average of the DOP owing to die bonding only. From (2.10) the DOP is related to the difference in normal strains in the material. These die bonds were comparatively uniform and so the approximation of DOP $\approx K_{\varepsilon}\varepsilon_{xx}$ as explained previously is reasonable here. The average value of DOP is proportional to the bonding strain and is used as an indirect measure of it here.

The DOP measurements for the one device in Fig. 6.1 show changes over time. In general, the DOP values exhibited a decreasing trend over time for the areas averaged in each map. It is clear from the maps in Fig. 6.1 that the DOP diminished over time, particularly between 132 hours and 447 hours. These chips were die bonded with a solid solder layer and the DOP pattern shows this relatively uniform bonding strain. In these scans the red area (negative DOP) near the bottom and the slightly blue areas (positive DOP) at the top indicate that the device was in tension at the bottom and slightly compressed at the top. This was expected since the coefficient of thermal expansion for diamond is 1.02×10^{-6} K^{-1} which is less than a quarter of that of InP (4.56×10^{-6} K^{-1}). The DOP pattern around the ridge at the top centre of each map was mostly unchanged in these scans since this was due to the metallization and epitaxial layers in that region. The magnitude of the DOP values across the facet are seen to decrease slightly (colour changing from red and blue to green which represents neutral or zero DOP).

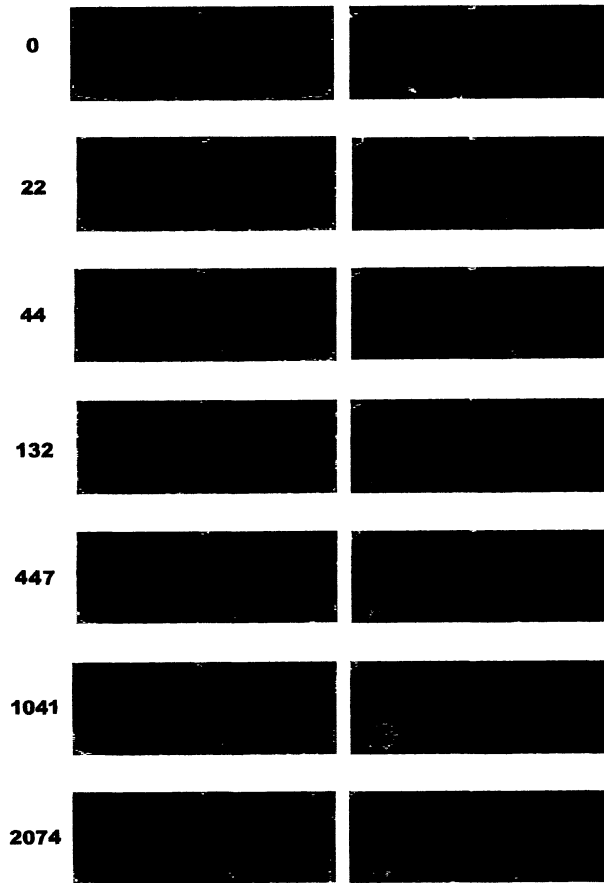

Fig. 6.1 Full facet DOP (left column) and ROP (right column) maps of a single device for each time, indicated on the left in hours, during the accelerated aging of the laser.

The data in Fig. 6.2 are area averages plotted against time for the particular device shown in Fig. 6.1. The average is from a rectangular area of the map centered horizontally and below the center vertically. The area is essentially in the center of the red area of the DOP map and is about a tenth of the total area of the facet. The plot is normalized by giving the data in percent remaining of the initial DOP at the various aging times from die bonding before aging. The averaged DOP values show, within experimental uncertainty, a decrease over time. The averaged DOP value at 2074 hours is 74 ± 10 percent of the averaged initial DOP value, i.e. at 0 hours of aging. The use of *'percent remaining of initial stress'* is a quantity that is often used in stress relaxation research since it normalizes the data for comparison. While a significant amount of DOP remains, it did decrease upon aging. The largest decrease seems to have occurred between 132 and 447 hours for this device.

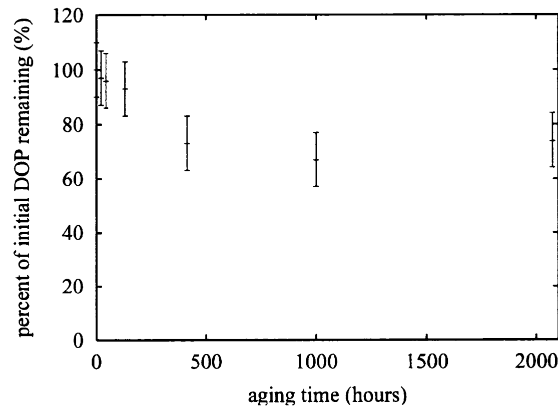

Fig. 6.2 The decrease in average DOP for the device in Fig. 6.1 over the aging time.

Individual devices showed a varied amount of DOP change and on average the aged devices had lower DOP values. This is shown in Table 6.1 which gives the percent of the average DOP values relative to the initial values for each device, averaged for all devices measured. That is, each datum is the average percent of the initial DOP remaining after aging to that point. Within experimental error, the average DOP values decreased with aging.

Table 6.1 Averaged DOP values for all devices.

TIME (hours)	PERCENT DOP RELATIVE TO INITIAL VALUE
0	100 ± 10
22	105 ± 10
44	105 ± 10
132	108 ± 10
447	68 ± 10
1041	64 ± 10
2074	75 ± 10

Overall, the averaged DOP value decreased by a quarter to a third from the initial DOP value. The data for 22 and 44 hours seems to show an increase in the DOP values but this is within uncertainty and so is not significant. As well, there appears to be an increase in the averaged DOP value at 2074 hours, but again within experimental uncertainty it did not change substantially from 1041 hours. It is believed that the reason the averaged DOP value showed these increases is a systematic error. That is, there are offsets possible with the DOP measuring system if it is not calibrated sufficiently. If each of the devices measured in a set of measurements had an offset relative to the other sets of measurements, then it would cause an apparent increase in the DOP. Within experimental uncertainty, the averaged DOP value is unchanged at 2074 hours compared with 1041 hours. Between 132 hours and 447 hours there is a definite drop in the averaged DOP

value which indicates stress relaxation over this time period. It would be desirable to have measurements at more points during the aging time between 132 and 447 hours to get a better idea of the trend of stress relaxation over that time period. Unfortunately such data was not available for this study.

6.4 Discussion

The relaxation of solders has been studied in detail elsewhere and it has typically been done in bulk form using a cast sample and an apparatus that measures the time dependent deformation of the material under constant strain conditions.[51] Most research has been done using a strain measurement apparatus over relatively short time scales such as tens of hours.[52] The work here shows stress relaxation over a much longer time period and it shows the stress relaxation *in situ* in an actual laser package. Because a hard solder was used for bonding, a long period for relaxation was expected. The DOP technique has been applied here to observe stress relaxation of the solder in diode lasers by measuring the strain in the laser chips. It is not believed that the crystalline InP, from which the lasers were made, would deform plastically under the thermal stresses of die bonding, so the relaxation is assumed to be entirely with the bond. The solder of the bond would be the primary place where the stress would relax. It may be possible that if the adhesion of the solder to the chip or the metallization layers were poor then the shear stress there could weaken the joint without deformation in the solder itself and be seen as stress relaxation. Since the time scale was so long for relaxation and since the bonds appeared to be uniform from the initial DOP maps, it is believed that all relaxation occurred within the solder.

A description of stress relaxation for solders is often modelled using an Arrhenius type relation to describe the rate of change of strain:

$$\frac{d\varepsilon}{dt} = A\sigma^{n}e^{-\frac{Q}{kT}} \tag{6.1}$$

where ε is the strain, A is a material dependent constant, σ is the stress, n is a stress exponent, k is Boltzmann's constant, T is the absolute temperature, and Q is the activation energy.[53] Such modelling uses an empirical power law to predict the effect of stress on the plastic strain rate of the material.[51] In this work only a single temperature was available since the samples here were measured as part of a larger aging study. It was, therefore, not possible to derive any temperature relationship with stress relaxation.

Stress relaxation in Pb-Sn solder was found by Tribula to be caused by extensive grain boundary sliding and intergranular cracking.[54] The temperature dependence on stress relaxation has been well studied and it is believed that inelastic deformation results from thermally-activated stress-assisted dislocation glide.[55] Increased temperature enhances stress relaxation since the added energy enables the relative displacements of atoms which must overcome energy

barriers to cross into neighbouring potential wells.[56] In the microstructure of a solder alloy, there exist regions of high concentration or even pure metals. The boundaries of these may be lines for displacements to occur. It was found by Vaynman that the microstructure of solders coarsens during prolonged aging, even at room temperature.[53] This coarsening leads to solder softening. Unksov states that stresses may not be completely relieved during relaxation, but are reduced to a value proportional to the initial stress.[56]

Since in this experiment the devices, hence the solder, experienced prolonged exposure to an elevated temperature and applied current, it is reasonable to expect these as contributing to the necessary energy requirements of the relaxation process. The time scale over which the stress relaxed in these samples is dependent on the temperature and possibly the current level. It would be desirable to conduct a study using a number of temperatures and currents to understand and quantify their effects on the stress relaxation. An important factor that is different in this study than others is that the stress here is thermally induced. The homologous temperature T_h of a material is the ratio of the current absolute temperature to the absolute melting point (it is a dimensionless parameter). The homologous temperature during aging here was $T_h = 0.77$. Operating the devices at such a high homologous temperature might seem to promote stress relaxation but thermal stress goes opposite to homologous temperature (i.e., the higher the homologous temperature, the lower the thermal stress).

Other experiments of stress relaxation typically use mechanically imposed strain, independent of temperature. Here, however, increased temperature would lead to lower thermal stress regardless of relaxation. So while the heat of the aging temperature may aid microstructural changes like dislocation glide, the increased aging temperature would have kept the chip and solder in a state of reduced stress during aging so the forces propelling any plastic deformation would have been reduced. It would have been useful to have a control group of chips that were driven with high levels of current but not held at an elevated temperature.

Each time the lasers were removed from the aging conditions, the thermal stress was increased in the die bonds as the homologous temperature was decreased. It is not known how much the cycling of the device temperature (from ambient conditions to the aging test conditions) affected the solder, such as causing fatigue in the metal. With such a small number of cycles it likely did not affect the solder.

Other solder relaxation work has found the relaxation time scale to be much shorter with softer solders like PbSn compared with hard solders like AuSn, as expected.[57] One might have expected the solder to relax in a shorter time since other research has shown stress relaxation to occur over much shorter time scales. Perhaps the physical form of the solder is a factor in this. That is, in stress relaxation experiments it is normal practice to cast a solid, bulk sample of the

material being tested and to use a strain gauge for measurements. The solder in a die bond is a relatively thin layer of material, several microns thick, and so the mechanics may be different than with a bulk sample. The material properties could be different at the scale of a real die bond. The observation of stress relaxation via the induced strain in the laser chips shows the effect on an actual device with the geometry and dimensions of real materials.

A bonding procedure has been proposed to use stress relaxation in a carefully controlled manner to reduce bonding strain. The idea is to neither slow cool nor rapid cool bonded devices after the solder is reflown, but instead to keep them at an intermediate temperature for an extended time.[42] Essentially, having the bonded chips held at a high homologous temperature for a number of hours is supposed to allow for solder relaxation to take place before the device is put into service. At higher temperatures, the relaxation should happen more quickly but the initial thermal stress would be lower. At lower temperatures the initial stress would be higher but the rate of relaxation would be reduced. A post-bonding heating of a sample at an intermediate temperature is a compromise between these two extremes. This has shown to be a successful procedure in die bonding large GaAs chips.[42]

6.5 Summary

Stress relaxation in diode laser die bonds was observed indirectly by measuring the decrease over time of the average DOP at the facet of diode lasers that were part of an accelerated aging study. The time scale over which this relaxation occurred was found to be on the order of hundreds of hours of accelerated aging. For the aggregate data, it was found that between 132 and 447 hours, the average DOP value measured decreased by approximately a third to 68 $\pm$ 10 percent of the initial value of DOP at time zero. The average total amount of DOP reduced after almost 2100 hours of accelerated aging was around a quarter to a third of the initial amount. It is sensible to suppose that reduced stress with age could be beneficial to the long term reliability of a diode laser. However, since it took many hundreds of hours of high current and temperature to relax the stress in these solder bonds it is not likely that stress relaxation would reduce the strain enough in a laser chip under normal conditions and in a reasonable amount of time to enhance a device's reliability.

The duration used for aging corresponds to many times the real time in actual devices at normal operating conditions. In other work related to stress relaxation in solders, relaxation times significantly shorter than this were observed. For a hard solder like AuSn relaxation times are expected to be longer compared with relatively softer materials like PbSn. It was observed that relaxation occurred over hundreds of hours of accelerated aging.

This work demonstrates that it is possible to observe stress relaxation in actual diode laser packages by making measurements on the diode laser itself.

This has the advantage that the measurements, while indirect of the actual plastic deformation in the solder responsible for the reduced strain on the chip, are made using solder that is in the form in a real bond. If the material properties of the solder are affected by its form this technique of observing the stress relaxation is more realistic than doing measurements using cast bulk samples.

CHAPTER 7 - FINITE ELEMENT METHOD FITTING

7.1 Introduction

This chapter is an explanation of a finite element method (FEM) model that is used iteratively in fits to polarization-resolved photoluminescence data. The chapter begins with an explanation of the motivation for creating such a model. The chapter then gives a general overview of the finite element method. Following that there is a FEM derivation specific to the model for elasticity problems with some comments about meshing and convergence. Once the specifics of the model are established, details of how the model is fit to the DOP and ROP data are given. In addition, some information is provided about how the fitting code was optimized to run more efficiently.

7.2 Motivation for FEM Fitting Code

A limitation with DOP and ROP measurements is that the DOP is proportional to a difference of strains or stresses. This makes directly interpreting the false colour maps difficult in complex cases (as in Fig. 5.4). In certain cases, one component of the strain or stress can be neglected by making assumptions about the boundary conditions on the diode laser chip. However, this fails if the conditions are anything but very simple. From (2.10) a negative DOP value means that ε_{xx} (or σ_{xx}) is greater than ε_{yy} (or σ_{yy}) but it does not provide the values of the individual components. Under simple assumed boundary conditions, it might be possible to make some approximation such as $\varepsilon_{xx} >> \varepsilon_{yy}$ (or $\sigma_{xx} >> \sigma_{yy}$) as in Section 4.2.1. This is only appropriate for cases in which the cause of the strain is well understood and the DOP map is unambiguous. If the DOP and ROP maps show complex patterns with varying positive and negative areas, it may not be justifiable to make such simplifications. In such cases it is still desirable to get quantitative information from the measurements rather than only qualitative patterns. To get the most out of the available data, a finite element method (FEM) model was created that fits to the measured data on the facet of the diode laser. The FEM model is fit to the measured DOP and ROP values to predict numerically the values of the components of stress and strain anywhere on the facet. From this information it is possible to estimate the effects of the strain on the reliability or on the optical properties of the device. This model was written before the latest calibration work, as described in Chapter 2, was completed and so it considers the DOP to be proportional to the difference of normal stresses and the ROP to be proportional to the shear stress in (2.10) and (2.12).

7.3 Finite Element Method

7.3.1 FEM Overview

The finite element method is a numerical modelling technique for approximately solving a broad assortment of problems for which a closed form solution is impossible or very difficult to obtain.[58] It works by breaking down a continuous problem domain into small domains and then solving the simplified individual problems concurrently. The result is a piecewise approximation across the problem domain to the governing equations of the system.[58] The problem domain is broken up into a finite number of elements, which can be of a large variety of shapes. The finite element discretization process reduces the overall problem such that there are a finite number of unknowns. Within each element, the unknown field variables are expressed in terms of approximating or interpolation functions. The approximating functions are defined in terms of the values of the field variables at nodes.[58] Each element is composed of a number of nodes. The discretization of a continuous domain makes the finite element method particularly well suited for solving problems using computers

There are several ways to formulate a finite element elasticity method problem. The direct approach is based on the direct stiffness method of structural analysis and is the simplest to understand. Two other ways of formulating finite element method problems include the variational approach and the weighted residuals approach, both of which are conceptually more difficult to understand than the direct approach. The variational approach is based on variational calculus and involves extremizing a functional.[59] The weighted residual approach is a more general way to set up a finite element method problem. The variational method is the one used in the model explained here and it is reasonably straightforward for solving three-dimensional elasticity problems.

The way in which the problem is mathematically formulated is only part of the procedure for solving it. Regardless of how the formulation is done, there are a number of steps in performing a finite element method calculation that are common. Generally, the steps are:[58]

- *discretize the continuum into a number of elements*
- *select the interpolation functions that will serve as approximations of the solution within the element*
- *set the properties of the element using one of the three formulation methods stated previously*
- *assemble the element properties into a system of equations that can be solved simultaneously*
- *set the boundary conditions on the physical system*
- *solve the system of equations*

7.3.2 Elasticity Problems

The finite element method model developed here is based on a relatively straightforward elasticity problem in solid mechanics. The model in this elasticity problem finds the nodal displacements given forces applied to a body. The model then calculates the strains (from displacements) and the stress throughout the body. It is a displacement formulation that uses the variational principal of solving for the minimum potential energy. The unknowns in the problem are the displacements of the nodes.

A continuous solid body experiences body forces throughout its volume and tractions on its surface. In three dimensions, these forces have three directional components. In each element, each node has three displacement degrees of freedom. The way in which these are constrained given applied forces comprises the boundary conditions for the problem. The nodes are displaced owing to the forces and from the nodal displacements, the elemental strains are computed based on the size and shape of the element. The stresses are calculated from the strains using the modulus matrix as in (2.8).

7.3.3 Meshing

In the finite element model described here the simplest three-dimensional element was used: a linear tetrahedral element. Such an element has four nodes each with three degrees of freedom corresponding to the three directions for displacement as in Fig. 7.1. Generating tetrahedra to fill arbitrarily a given volume and shape is a non-trivial task. To generate the tetrahedra used in this model, freeware code obtained on the Internet was implemented. The code was written by a computer science student, Hang Si, in China and it was made freely available.[60] For the purpose of modelling elasticity in diode lasers, a model chip is first fashioned as a space lattice of nodes. The tetrahedral generating routine, kept as a separate code library, is then called to fill in the mesh with tetrahedra (creating interstitial nodes where necessary to complete the tetrahedralization). It is fortunate that this highly useful code library was found and that it was put in the public domain.

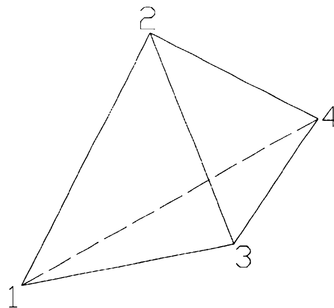

Fig. 7.1 Schematic of tetrahedral element.

7.3.4 Interpolation Functions

The interpolation functions used to approximate the displacement variables within the element are linear polynomials. Since the displacements vary linearly within the element, the stresses and strains, which are related to the derivatives of the displacements are constant within the elements. Therefore the element used is considered to be a constant strain tetrahedron.[58]

So-called natural coordinates are used to define the interpolation functions for the elements. Natural coordinates rely on the geometry of the element for their definition. The local coordinates range from 0 to 1 within the element. Any given coordinate has a value of 1 at one node and 0 at the other nodes, with the value varying linearly within the element.[59] In the case of a four-node tetrahedron, the natural coordinates are volume coordinates which physically correspond to ratios of volumes in the tetrahedron. By using natural coordinates with linear polynomial interpolation functions, closed-form integration formulas exist which simplifies computation.

In this section and the next, the equations for a single tetrahedral element will be derived. The resulting system of equations for each element are then combined together into a global system of equations covering the entire body in question. In the following, u, v, and w represent displacements in the x, y, and z directions respectively. A column vector is represented using the brackets $\lfloor\ \rfloor$, a row vector is represented using $\lceil\ \rceil$, and a matrix is represented by [ ]. Assume a tetrahedron with the four nodes labeled *1, 2, 3*, and *4* as in Fig. 7.1. For a linear tetrahedron, the global Cartesian coordinates (x_i,y_i,z_i; i = 1,2,3,4) and natural local coordinates (x, y, z) are related by:[58]

$$\begin{aligned}
x &= N_1x_1 + N_2x_2 + N_3x_3 + N_4x_4 \\
y &= N_1y_1 + N_2y_2 + N_3y_3 + N_4y_4 \\
z &= N_1z_1 + N_2z_2 + N_3z_3 + N_4z_4 \\
1 &= N_1 + N_2 + N_3 + N_4
\end{aligned} \qquad (7.1)$$

This set of equations can be solved using Cramer's determinant method to give the interpolation functions N_i as functions of x, y, and z:

$$N_i(x,y,z) = \frac{1}{6V}\left(a_i + b_ix + c_iy + d_iz\right) \; i = 1,2,3,4 \qquad (7.2)$$

where 6V is the volume of the tetrahedron and is given by:

$$6V = \begin{vmatrix} 1 & x_1 & y_1 & z_1 \\ 1 & x_2 & y_2 & z_2 \\ 1 & x_3 & y_3 & z_3 \\ 1 & x_4 & y_4 & z_4 \end{vmatrix}$$

and the coefficients are given by:

$$a_1 = \begin{vmatrix} x_2 & y_2 & z_2 \\ x_3 & y_3 & z_3 \\ x_4 & y_4 & z_4 \end{vmatrix} \quad b_1 = -\begin{vmatrix} 1 & y_2 & z_2 \\ 1 & y_3 & z_3 \\ 1 & y_4 & z_4 \end{vmatrix} \quad c_1 = -\begin{vmatrix} x_2 & 1 & z_2 \\ x_3 & 1 & z_3 \\ x_4 & 1 & z_4 \end{vmatrix} \quad d_1 = \begin{vmatrix} x_2 & y_2 & 1 \\ x_3 & y_3 & 1 \\ x_4 & y_4 & 1 \end{vmatrix}$$

with the other constants (a_2, a_3, a_4, b_2, b_3, etc.) given by cyclic permutation of the subscripts. Using the interpolation functions N_i the element displacement field can be expressed in terms of the nodal displacements (u_1, v_1, w_1, u_2, v_2, w_2, etc.):

$$\begin{aligned} u(x,y,z) &= N_1(x,y,z)u_1 + N_2(x,y,z)u_2 + N_3(x,y,z)u_3 + N_4(x,y,z)u_4 \\ v(x,y,z) &= N_1(x,y,z)v_1 + N_2(x,y,z)v_2 + N_3(x,y,z)v_3 + N_4(x,y,z)v_4 \\ w(x,y,z) &= N_1(x,y,z)w_1 + N_2(x,y,z)w_2 + N_3(x,y,z)w_3 + N_4(x,y,z)w_4 \end{aligned} \tag{7.3}$$

With [N] as the interpolation function matrix, and $\lfloor\delta\rfloor$ the nodal displacement vector, this can be written in matrix form as:

$$\begin{bmatrix} u \\ v \\ w \end{bmatrix} = \begin{bmatrix} N_1 & 0 & 0 & N_2 & 0 & 0 & N_3 & 0 & 0 & N_4 & 0 & 0 \\ 0 & N_1 & 0 & 0 & N_2 & 0 & 0 & N_3 & 0 & 0 & N_4 & 0 \\ 0 & 0 & N_1 & 0 & 0 & N_2 & 0 & 0 & N_3 & 0 & 0 & N_4 \end{bmatrix} \begin{bmatrix} u_1 \\ v_1 \\ w_1 \\ u_2 \\ v_2 \\ w_2 \\ u_3 \\ v_3 \\ w_3 \\ u_4 \\ v_4 \\ w_4 \end{bmatrix} = [N]\lfloor\delta\rfloor \tag{7.4}$$

The infinitesimal strain $\lfloor\varepsilon\rfloor$ at a point is related to the displacement vector via the linear operator matrix [L]:[58]

$$\lfloor \varepsilon \rfloor = \begin{bmatrix} \varepsilon_{xx} \\ \varepsilon_{yy} \\ \varepsilon_{zz} \\ 2\varepsilon_{xy} \\ 2\varepsilon_{xz} \\ 2\varepsilon_{yz} \end{bmatrix} = \begin{bmatrix} \frac{\partial}{\partial x} & 0 & 0 \\ 0 & \frac{\partial}{\partial y} & 0 \\ 0 & 0 & \frac{\partial}{\partial z} \\ \frac{\partial}{\partial y} & \frac{\partial}{\partial x} & 0 \\ \frac{\partial}{\partial z} & 0 & \frac{\partial}{\partial x} \\ 0 & \frac{\partial}{\partial z} & \frac{\partial}{\partial y} \end{bmatrix} \begin{bmatrix} u \\ v \\ w \end{bmatrix} \tag{7.5}$$

Substituting (7.4) into (7.5) the interpolation matrix is differentiated by the linear operator matrix to give:

$$\lfloor \varepsilon \rfloor = [L][N]\lfloor \delta \rfloor$$

$$= \begin{bmatrix} \frac{\partial N_1}{\partial x} & 0 & 0 & \frac{\partial N_2}{\partial x} & 0 & 0 & \frac{\partial N_3}{\partial x} & 0 & 0 & \frac{\partial N_4}{\partial x} & 0 & 0 \\ 0 & \frac{\partial N_1}{\partial y} & 0 & 0 & \frac{\partial N_2}{\partial y} & 0 & 0 & \frac{\partial N_3}{\partial y} & 0 & 0 & \frac{\partial N_4}{\partial y} & 0 \\ 0 & 0 & \frac{\partial N_1}{\partial z} & 0 & 0 & \frac{\partial N_2}{\partial z} & 0 & 0 & \frac{\partial N_3}{\partial z} & 0 & 0 & \frac{\partial N_4}{\partial z} \\ \frac{\partial N_1}{\partial y} & \frac{\partial N_1}{\partial x} & 0 & \frac{\partial N_2}{\partial y} & \frac{\partial N_2}{\partial x} & 0 & \frac{\partial N_3}{\partial y} & \frac{\partial N_3}{\partial x} & 0 & \frac{\partial N_4}{\partial y} & \frac{\partial N_4}{\partial x} & 0 \\ \frac{\partial N_1}{\partial z} & 0 & \frac{\partial N_1}{\partial x} & \frac{\partial N_2}{\partial z} & 0 & \frac{\partial N_2}{\partial x} & \frac{\partial N_3}{\partial z} & 0 & \frac{\partial N_3}{\partial x} & \frac{\partial N_4}{\partial z} & 0 & \frac{\partial N_4}{\partial x} \\ 0 & \frac{\partial N_1}{\partial z} & \frac{\partial N_1}{\partial y} & 0 & \frac{\partial N_2}{\partial z} & \frac{\partial N_2}{\partial y} & 0 & \frac{\partial N_3}{\partial y} & \frac{\partial N_3}{\partial y} & 0 & \frac{\partial N_4}{\partial z} & \frac{\partial N_4}{\partial y} \end{bmatrix} \begin{bmatrix} u_1 \\ v_1 \\ w_1 \\ u_2 \\ v_2 \\ w_2 \\ u_3 \\ v_3 \\ w_3 \\ u_4 \\ v_4 \\ w_4 \end{bmatrix} \tag{7.6}$$

$$= [B]\lfloor \delta \rfloor$$

The [B] matrix is known as the strain-interpolation matrix or the kinematic matrix in finite element method problems.

7.3.5 Minimum Potential Energy Principle

The minimum potential energy principle is a variational principle in solid mechanics. If a body is deformed elastically by external forces the potential energy of such a body is defined as the energy of deformation of the body (strain energy) minus the work done on the body by the external forces. The minimum potential energy principle is as follows: the displacement which satisfies the differential equations of equilibrium, as well as the conditions at the boundary surface, yields a smaller value for the potential energy than for any other displacement which satisfies the same conditions at the bounding surface.[59]

If $\Pi(u,v,w)$ is the potential energy, $U(u,v,w)$ is the strain energy, and $V(u,v,w)$ is the work done by the loading during displacement (u,v,w) then at equilibrium:

$$\Pi(u,v,w) = U(u,v,w) - V(u,v,w) \tag{7.7}$$

The strain energy for a solid body of volume Ω that is strained by an amount ε with a stress σ is defined as:[58]

$$U(u,v,w) = \frac{1}{2}\int_\Omega \lceil \varepsilon \rceil \lfloor \sigma \rfloor dV \tag{7.8}$$

Substituting in the expressions from (7.6) and (2.8) into (7.8),

$$U(u,v,w) = \frac{1}{2}\int_\Omega \lceil \varepsilon \rceil [C] \lfloor \varepsilon \rfloor dV = \frac{1}{2}\int_\Omega \lceil \delta \rceil [B]^T [C][B] \lfloor \delta \rfloor dV \tag{7.9}$$

The work done by external forces (volume body forces F_b and surface tractions T) is:

$$V(u,v,w) = \int_\Omega \lceil \delta \rceil [N]^T \lfloor F_b \rfloor dV + \int_S \lceil \delta \rceil [N]^T \lfloor T \rfloor dS \tag{7.10}$$

The potential energy, in (7.7), including an initial strain factor, is then:[58]

$$\begin{aligned} \Pi(u,v,w) = &\frac{1}{2}\int_\Omega \left\{ \lceil \delta \rceil [B]^T [C][B] \lfloor \delta \rfloor - 2\lceil \delta \rceil [B]^T [C] \lfloor \varepsilon_o \rfloor \right\} dV \\ &- \int_\Omega \lceil \delta \rceil [N]^T \lfloor F_b \rfloor dV - \int_A \lceil \delta \rceil [N]^T \lfloor T \rfloor dS \end{aligned} \tag{7.11}$$

This total potential energy can be minimized using variational calculus,

$$\frac{\partial \Pi(u,v,w)}{\partial [\delta]} = 0 \tag{7.12}$$

to result in

$$\int_{\Omega}[B]^T[C][B]\lfloor\delta\rfloor dV - \int_{\Omega}[B]^T[C]\lfloor\varepsilon_o\rfloor dV - \int_{\Omega}[N]^T\lfloor F_b\rfloor dV - \int_{A}[N]^T\lfloor T\rfloor dS = 0$$

$$\int_{\Omega}[B]^T[C][B]\lfloor\delta\rfloor dV = \int_{\Omega}[B]^T[C]\lfloor\varepsilon_o\rfloor dV + \int_{\Omega}[N]^T\lfloor F_b\rfloor dV + \int_{A}[N]^T\lfloor T\rfloor dS \tag{7.13}$$

$$[K]\lfloor\delta\rfloor = \lfloor F\rfloor$$

with

$$\lfloor F\rfloor = \lfloor F_o\rfloor + \lfloor F_B\rfloor + \lfloor F_T\rfloor \tag{7.14}$$

The initial force vector is:

$$\lfloor F_o\rfloor = \int_{\Omega}[B]^T[C]\lfloor\varepsilon_o\rfloor dV \tag{7.15}$$

The body force vector is:

$$\lfloor F_B\rfloor = \int_{\Omega}[N]^T\lfloor F_b\rfloor dV \tag{7.16}$$

The surface traction vector is:

$$\lfloor F_T\rfloor = \int_{S}[N]^T\lfloor T\rfloor dS \tag{7.17}$$

If there are N nodes then there will be 3N displacements, 3N forces, and a stiffness matrix that is 3N x 3N. Once the strain-displacement matrix, B, is determined then the stiffness matrix can be calculated and the linear system solved for the unknown nodal displacements.

To determine the stiffness matrix it is required, in general, to perform differentiations and integrations (closed form or numerically). The convenience of the natural coordinates allows this to be done simply and in advance in a constant strain element. From (7.13),

$$[K] = \int_{\Omega}[B]^T[C][B]dV \tag{7.18}$$

From (7.6)

$$
[B]=[L][N]
$$

$$
=\begin{bmatrix}
\frac{\partial N_1}{\partial x} & 0 & 0 & \frac{\partial N_2}{\partial x} & 0 & 0 & \frac{\partial N_3}{\partial x} & 0 & 0 & \frac{\partial N_4}{\partial x} & 0 & 0 \\
0 & \frac{\partial N_1}{\partial y} & 0 & 0 & \frac{\partial N_2}{\partial y} & 0 & 0 & \frac{\partial N_3}{\partial y} & 0 & 0 & \frac{\partial N_4}{\partial y} & 0 \\
0 & 0 & \frac{\partial N_1}{\partial z} & 0 & 0 & \frac{\partial N_2}{\partial z} & 0 & 0 & \frac{\partial N_3}{\partial z} & 0 & 0 & \frac{\partial N_4}{\partial z} \\
\frac{\partial N_1}{\partial y} & \frac{\partial N_1}{\partial x} & 0 & \frac{\partial N_2}{\partial y} & \frac{\partial N_2}{\partial x} & 0 & \frac{\partial N_3}{\partial y} & \frac{\partial N_3}{\partial x} & 0 & \frac{\partial N_4}{\partial y} & \frac{\partial N_4}{\partial x} & 0 \\
\frac{\partial N_1}{\partial z} & 0 & \frac{\partial N_1}{\partial x} & \frac{\partial N_2}{\partial z} & 0 & \frac{\partial N_2}{\partial x} & \frac{\partial N_3}{\partial z} & 0 & \frac{\partial N_3}{\partial x} & \frac{\partial N_4}{\partial z} & 0 & \frac{\partial N_4}{\partial x} \\
0 & \frac{\partial N_1}{\partial z} & \frac{\partial N_1}{\partial y} & 0 & \frac{\partial N_2}{\partial z} & \frac{\partial N_2}{\partial y} & 0 & \frac{\partial N_3}{\partial y} & \frac{\partial N_3}{\partial y} & 0 & \frac{\partial N_4}{\partial z} & \frac{\partial N_4}{\partial y}
\end{bmatrix}
$$

$$
=\frac{1}{6V}\begin{bmatrix}
b_1 & 0 & 0 & b_2 & 0 & 0 & b_3 & 0 & 0 & b_4 & 0 & 0 \\
0 & c_1 & 0 & 0 & c_2 & 0 & 0 & c_3 & 0 & 0 & c_4 & 0 \\
0 & 0 & d_1 & 0 & 0 & d_2 & 0 & 0 & d_3 & 0 & 0 & d_4 \\
c_1 & b_1 & 0 & c_2 & b_2 & 0 & c_3 & b_3 & 0 & c_4 & b_4 & 0 \\
0 & d_1 & c_1 & 0 & d_2 & c_2 & 0 & d_3 & c_3 & 0 & d_4 & c_4 \\
d_1 & 0 & b_1 & d_2 & 0 & b_2 & d_3 & 0 & b_3 & d_4 & 0 & b_4
\end{bmatrix} \tag{7.19}
$$

The [B] matrix is composed of values depending on the size and shape of the element. The [C] matrix is composed of values dependent on the material properties. Both of these are constants in the case of a tetrahedron with linear polynomial interpolation functions so the evaluation of the integral in (7.18) involves only constant terms. The stiffness matrix for an element can then be computed as a matrix multiplication times a scalar:

$$
[K]=[B]^T[C][B]V \tag{7.20}
$$

The stiffness matrix [K] in (7.20) is for a single element and is called a local stiffness matrix.[58] It gives the relationship between the forces on an element and the displacements of the nodes from (7.13):

$$
\lfloor F \rfloor = [K] \lfloor \delta \rfloor \tag{7.13}
$$

The local stiffness matrix is a symmetric 12×12 matrix for a four-node tetrahedral element. The force vector and the displacement vector are each 1×12 column vectors (for each direction of each node). The local stiffness matrices for each element are then assembled into a global stiffness matrix for the entire problem, covering all the elements. As well, the forces on the local nodes of each element are assembled into a global force vector. The result is a large system of linear equations (3N equations and 3N unknowns for N nodes). Upon solving the linear

system for the displacements $\lfloor\delta\rfloor$ owing to the forces $\lfloor F\rfloor$, the strains $\lfloor\varepsilon\rfloor$ and stresses $\lfloor\sigma\rfloor$ can be computed for each element from (7.6) and (2.8):

$$\lfloor\varepsilon\rfloor=[B]\lfloor\delta\rfloor \tag{7.6}$$

$$\lfloor\sigma\rfloor=[C]\lfloor\varepsilon\rfloor \tag{2.8}$$

The forces are applied using (7.15-7.17) to the nodes in the force vector. The surface tractions are applied to the outside triangular faces of the tetrahedra using the lumped force method.[58] This method works only for the case of linear interpolation (constant strain) and uses forces calculated at the nodes based on the exposed surface area of the face. Any traction is given as a force per unit area and the lumped force method calculates the force on the nodes by way of the area of the face. This, again, avoids complications that would necessitate numerical integration if higher order interpolation functions were used.

7.3.6 Convergence

Since the finite element method uses a discrete approximation to a continuous function there is the matter of the convergence of the approximate solution to the true solution. The finite element method is limited by the rate of convergence to a solution, as a function of the number of elements used.[61] For a solution to converge with an increasing number of elements, there are two principal requirements of the interpolation functions: completeness and compatibility. The compatibility requirement states that the field variable (displacement in this case) and any of its partial derivatives must be continuous at element interfaces. The completeness requirement states that when the element size is decreased and approaches zero, the highest derivative of the field variable (displacement) exists. For the constant strain tetrahedron element, these conditions hold so the FEM solution does converge in the limit.[59]

The rate of convergence of the approximate solution to the exact solution is often given in terms of a parameter, h, that is a measure of the mesh "size" of the element. The error is the difference between the approximate solution and the exact solution. A properly defined FEM problem will yield an exact solution in the limit as $h \to 0$. The rate of convergence is the rate that the error is reduced as h is decreased (i.e., greater number of elements). It can be shown that for a polynomial interpolation function of degree p, the convergence rate is of order $O(h^{p+1})$. So for a first order polynomial, as is the case here, the convergence rate is of order $O(h^2)$. This means that reducing the mesh spacing parameter h by 2 will reduce the error by 4.[59] There are other sources of error, to be discussed later, which are more significant in the overall FEM fitting than this error.

The finite element method code was tested using a number of problems for which closed form solutions were known. These included such problems as three-point bending, uniaxial stress, and cantilever problems. The code correctly predicted the stresses and strains for these. That is, for the simplest problems, the

code was able to produce the results almost exactly and for slightly more complicated problems the results were correct within a few percentage points. In addition the code was compared with a commercial FEM package, ANSYS, using more complex problems and it was found to produce similar results as that package.

7.4 Fitting to Degree of Polarization Data

The fitting routine finds the combination of forces (surface tractions) that generates stresses in the material that, when converted to DOP and ROP values via (2.10) and (2.12), best match the measured DOP and ROP patterns. Since the DOP and ROP data are measured of the photoluminescence at the facet (which is created within a short depth of the surface), the simulated stresses are compared at the surface of the model. The tractions are representative of the forces that are imposed on a diode laser by such things as deposited oxide layers, metal films, and die bonding. These external forces are on the top and bottom of a laser chip so in the model the forces are imposed on the top and bottom of the model chip. The modelled DOP and ROP data are matched with the measured data by a least squares fitting routine.

It is desired to find the combination of surface forces that results in a best fit match between the measured data and the FEM model at the facet. It is preferred to limit the number of times that the FEM solver would have to execute during a fit since each FEM solution is computationally intensive and so is time consuming. It would be imprudent to have the FEM code execute multiple times within the fitting algorithm each time one of the applied forces is adjusted slightly while a best fit is sought. In the fitting algorithm the hundreds of forces that are used to fit a model are adjusted thousands of times. Conveniently the FEM solver provides a linear solution to a linear problem so that the effects of each of the forces can be computed independently. The solver finds the m nodal displacements $\lfloor \delta \rfloor$, an $m \times 1$ vector, as a consequence of applied forces $\lfloor F \rfloor$, an $m \times 1$ vector, via the global stiffness matrix $[K]$, an $m \times m$ matrix, by solving the linear system: $\lfloor F \rfloor = [K]\lfloor \delta \rfloor$. Since it is a linear system the principle of linear superposition can be used to separate the strains owing to different forces. That is, if a force was composed of two forces, i.e. $F = F_1 + F_2$, then the force vector could be given by $\lfloor F \rfloor = \lfloor F_1 \rfloor + \lfloor F_2 \rfloor$. Each of the forces results in displacements via the global stiffness matrix, $\lfloor F_1 \rfloor = [K]\lfloor \delta_1 \rfloor$ and $\lfloor F_2 \rfloor = [K]\lfloor \delta_2 \rfloor$. Since the system is a linear system,

$$\begin{aligned} [F] &= [F_1] + [F_2] \\ &= [K]\lfloor \delta_1 \rfloor + [K]\lfloor \delta_2 \rfloor \\ &= [K]\lfloor \delta_1 + \delta_2 \rfloor \end{aligned} \tag{7.21}$$

The sum of the resultant nodal displacements (hence elemental strains and stresses) of separately applied forces is equivalent to the result of applying the sum of the

forces together. It is then required to only find a FEM solution once for each of the applied forces. A best fit match between the measured data and the model is a linear combination of the resultant strains owing to the separately applied forces. The stresses are calculated in the model for each force separately with the FEM solver and then those stresses near the facet are stored and converted to DOP and ROP via (2.10) and (2.12). The independently calculated DOP and ROP patterns are then used in the fitting algorithm to find a linear combination that best fits the measured data. The linear coefficients that are found in the fitting portion of the code are used as scaling coefficients for the forces in the final model.

Once the strain patterns at the model facet for the individually applied surface tractions have been calculated with the FEM solver and converted to DOP and ROP values it is left to a fitting routine to find the combination of them that best matches the measured DOP and ROP patterns. The problem is really a least squares fit to two arbitrary functions where the functions are the values of the DOP and ROP data at each point on the facet. That is, one wants to minimize the difference between each datum from the measured pattern with a linear combination of the modelled data. If χ^2 is the sum of the squares of the difference between the measured values and a linear combination of the modelled values, then a best fit will be achieved by minimizing:

$$\chi^2 = \sum_{j=1}^{n}\left[y_j - \sum_{i=1}^{m} a_i x_{ij} \Big| \right]^2 \tag{7.22}$$

where y_j is one of the n measured values on the facet, x_{ij} is one of the n modelled values on the facet owing to one of the m applied forces, and a_i is one of the m linear coefficients. It is for the a_i parameters that the fitting algorithm is searching. The fitting routine needs to search an m-dimensional hyperplane to find that point where the χ^2 function is minimal.[45]

There are a number of ways to achieve a best fit but a reliable and efficient algorithm is one first proposed by Marquardt.[62] This algorithm performs an optimum interpolation between a gradient search method and an analytic expansion of χ^2 to find a minimum. It is largely insensitive to starting parameters yet converges reasonably quickly to a best fit solution. The measured data consist of two parts: the DOP and ROP, and the total χ^2 is a combination of the two: $\chi^2 = \chi^2_{DOP} + \chi^2_{ROP}$. The algorithm therefore finds the minimum of this goodness-of-fit function which consists of the sum of two sets of n points each where each point is the squared difference of the measured value and a linear combination of m FEM generated values. A block diagram of the fitting procedure is in Fig. 7.2.

Once χ^2 has been minimized and the linear coefficients determined, a final FEM model is run with all of the forces applied with their correct weighting to give a best fit of the model to the measured DOP and ROP patterns on the facet. The final model enables easy extraction of the components of stresses and strains anywhere on the facet. From elaborate DOP and ROP patterns, least squares

estimates of the values are obtained for the strains and stresses present at the facet. The uncertainty in the values derived from the fits is believed to be dominated by the uncertainty in the calibration constant in (2.10) and (2.12). Other factors would be the quality of the fit, the error in the FEM model, and noise in the polarization-resolved measurements. Based on these factors the uncertainty for the values derived by this method are estimated to be approximately 20%.

InP-based diode lasers were studied with this fitting technique and since InP is a III-V semiconductor that is an orthotropic material, there are only three independent stiffness constants (C_{11}, C_{12}, and C_{44} in the standard matrix notation from Table 3.1). The DOP and ROP are measured on the diode laser facet which is along the principal cleavage plane. Because this plane for such a semiconductor is a (110) plane the fourth rank modulus tensor has to be rotated 45° about [001]. The rotated tensor components are used in the FEM code in the simplified matrix format.

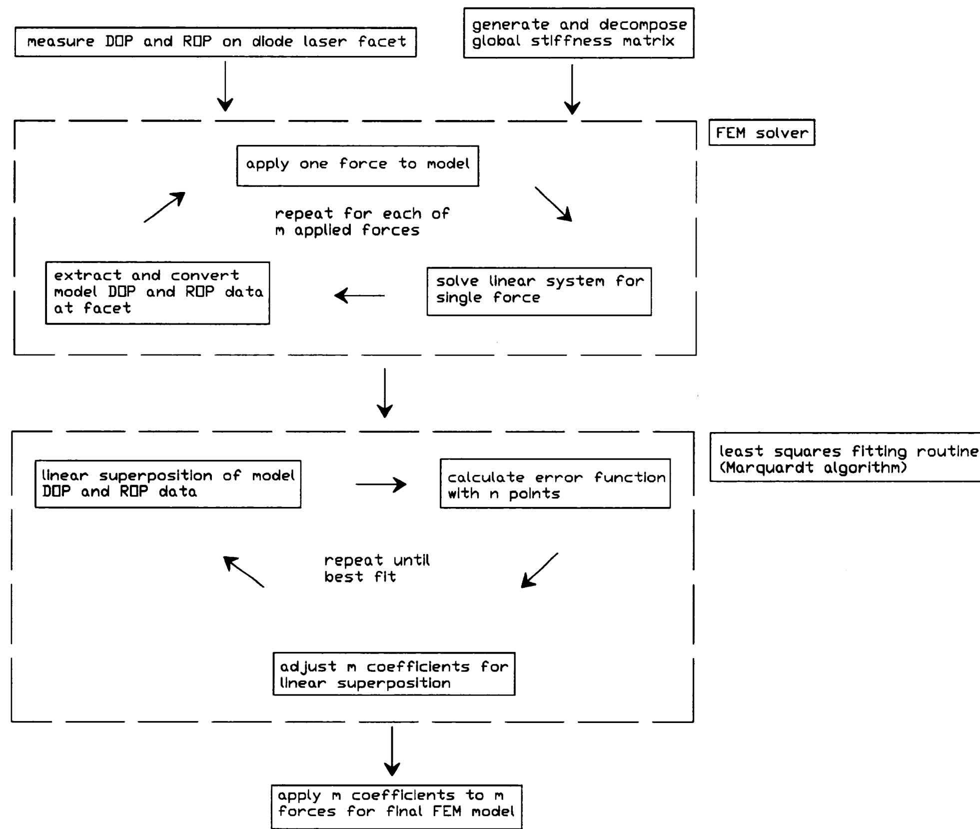

Fig. 7.2 Diagram of general steps in iterative fitting of FEM model to DOP and ROP data.

7.5 Efficiency Improvements

An iterative finite element method routine is computationally intensive. It requires repeatedly finding FEM solutions to fit to the desired solution. There are a number of enhancements which have been implemented in the code described here to make the model run as efficiently as possible. The principal enhancements which will be described below are:

- *superposition of individual FEM solutions*
- *banded Cholesky decomposition for solving the linear system*
- *re-use of the global stiffness matrix*
- *use of the Marquardt fitting algorithm*

The most important enhancement has already been described in the previous section. Since the finite element method in this case is a linear system, it is possible to separate the stresses owing to separate forces applied individually and use the principle of superposition to combine them. The fitting algorithm can then run afterwards without re-running the FEM code for each adjustment that is made in trying to find a least squares fit of the model to the measured DOP and

ROP data. If the fitting routine had to run the FEM code for each adjustment instead of just altering the coefficients in the linear combination, it would take many times longer to find a best fit solution. It would not be possible to perform a fit like this with a problem that is not linear.

To solve the system of linear equations there are a number of well-known methods available. There exist Gaussian elimination and LU decomposition as examples.[63] For computational efficiency it was decided to use the Cholesky decomposition algorithm. The Cholesky method decomposes the system matrix into a lower triangular matrix which is used to back substitute for the unknowns of the system. The Cholesky method takes advantage of the fact that the system of equations produces a symmetric, positive definite matrix.[63] This allows it to avoid unnecessary calculations and memory usage. If the element nodes are numbered appropriately, then the system matrix can have a small bandwidth (that is, many zero elements off of the diagonal). This is used to advantage to save memory and computing time greatly.

In finding the FEM solutions to the individually applied forces, it was found to be advantageous to break the FEM code into those parts which change upon applying a new force and those which do not. For example, the global stiffness matrix remains the same for each applied force. The linear system is solved using a banded Cholesky decomposition algorithm as described above. The global stiffness matrix only needs to be decomposed once. Creating the local stiffness matrices, combining them into a global stiffness matrix, and decomposing that matrix is the most computationally demanding part the FEM solution. By setting up the code to only do this once and to store the partial results to be used for each applied force saves a significant amount of computer time. Essentially, once the global stiffness matrix has been created and decomposed, the force vector for each applied force can be back-substituted into the linear system to solve for each displacement vector quite quickly. Elimination of the repeated creation and decomposition of the stiffness matrix resulted in the code running hundreds of times faster.

The choice of the fitting algorithm used to find the linear combination of FEM solutions that yields a least squares minimum is also quite important for efficiency. There exist a number of methods of fitting an arbitrary function to data, such as the grid-search method and the gradient-search method.[62] These methods were implemented in turn, owing to their simplicity, but both were found to be too inefficient. The Marquardt algorithm which was considerably more complicated to use, was found to be excellent at finding best fit solutions reasonably quickly.[62] It involves a hybrid search method that incorporates the best of both the gradient search method and analytical expansion methods to produce a reliable and quick algorithm.[62]

There were other aspects of the code which were ameliorated for speed and memory usage but the optimizations above, which were incrementally implemented in the FEM fitting code, resulted in speed improvements of many

thousands of times and greatly reduced memory. Using a state of the art computer, as of the year 2003, running at 2 GHz and with 1 GB of RAM, a fit like those to be shown in the following chapter took about half a day to compute. This is with the numerous optimizations included. Without these it would not be possible to do such fitting.

7.6 Summary

This chapter described the finite element method code used to fit to DOP and ROP measurements to extract stress and strain components. The motivation for writing a FEM fitting code was given in 7.2. In 7.3, the finite element method as it applies to linear elasticity problems was developed. Section 7.4 described the way in which the finite element method was used to fit to the measurements. Finally, in section 7.5 were described a number of important optimizations that were implemented to make the code run more efficiently. The results of the FEM fitting code will be shown in the next chapter.

CHAPTER 8 - APPLICATION OF FEM FITTING

8.1 Introduction

This chapter builds on the previous one by providing examples of fits from the iterative finite element method fitting code. In 8.2 an example FEM fit to a bonded chip is shown. There are false colour maps shown comparing the measured and modelled DOP and ROP data for an InP chip bonded to a copper carrier. As well, there are data extracted from this model. In Section 8.3, a number of chips from Chapter 5 are examined. This section shows how some of the intricate DOP and ROP maps owing to die bonding strain can be fitted quite well using the FEM fitting code. Section 8.4 demonstrates how the output from a FEM fit can be used to predict photoelastic effects. These refractive index changes are then used to simulate variations in the mode of the waveguide. In Section 8.5 there is an exploration of using DOP measurements, along with the FEM fitting to detect voids in diode laser die bonds.

8.2 Example Fit to Bonded Device

To test the FEM fitting code, a number of diode laser chips were die bonded and fitted. This section shows the results of the first of these. An InP chip was mounted to a copper chip carrier using a solder preform that had a composition of 80/20 (weight percent) Au/Sn. The chip was bonded using a Kulicke and Soffa manual hotspot die bonder. The bonding temperature was approximately 320°C and forming gas was used. The solder thickness was estimated to be approximately 10 μm.

The DOP and ROP values over the facet of the packaged device were measured using the set-up described previously in Chapter 2. In the DOP and ROP maps, the scanning resolution was 5 μm both horizontally and vertically, which is sufficient to observe bonding features. The data maps in Fig. 8.1 show the results of the measurements with the DOP on the left and the ROP on the right.

A finite element method model was iteratively fit to the DOP and ROP maps of the facet. The FEM model for this chip was composed of 84240 elements and 16324 nodes and the fit used 260 surface tractions on the bottom of the chip to simulate the behaviour of the solder there to fit to the measured DOP and ROP maps. The dimensions of the elements were of the order of 5 μm × 5 μm × 15 μm. The number of points on the facet with which the algorithm fit the data is 1404 so that from (7.22) $n = 1404$ and $m = 260$. With N = 16324 nodes, the linear system was composed of 3 × N = 48972 equations and 48972 unknowns. These fitting parameters are typical of the other fits reported in this thesis. Figure 8.2 shows false colour maps of modelled DOP and ROP data from the fit.

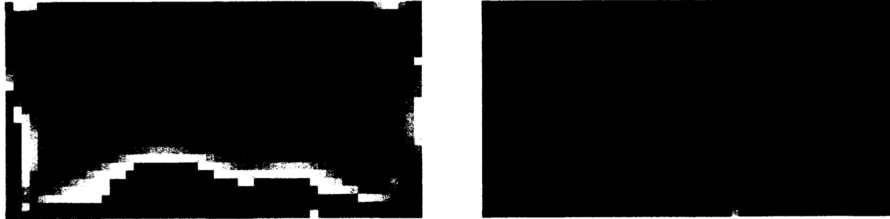

Fig. 8.1 False colour maps of measured DOP (left) and ROP (right) of the facet of a chip bonded to a copper carrier.

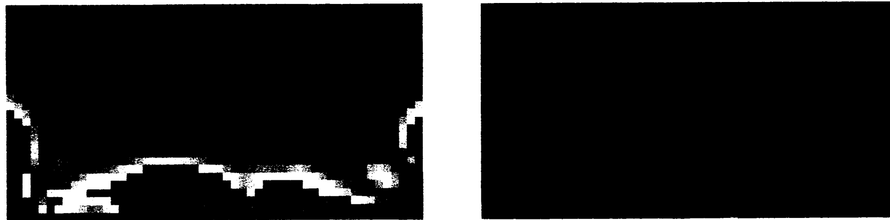

Fig. 8.2 False colour maps of modelled DOP (left) and ROP (right) from the chip shown in Fig. 8.1.

There is a reasonable agreement between the measured and modelled DOP and ROP maps comparing Figs. 8.1 and 8.2. The DOP and ROP are each visually similar over most of the area of the facet except the top of the DOP where there is a noticeable difference. Since a preform was used to bond the chip, it could be that solder that protruded out and up the sides of the chip and might have introduced strain along the sides that is in addition to the strain in the plane of the bonding interface. The model only used surface forces on the bottom of the chip.

In Fig. 8.3 strain data have been extracted from the model. These data are taken at the facet of the modelled chip along a horizontal line 5 μm from the bottom of the chip. The line plot of strain in Fig. 8.3.(a) is ε_{xx} strain (x is horizontal and y is vertical, as in Fig. 2.1). In Fig. 8.3.(b) is a plot of ε_{yy} strain along the same line. The maximum ε_{xx} strain along this line is approximately -0.4% (i.e., in compression). Since this is an InP based chip bonded to a copper carrier, it is expected that the chip would be in compression near the bonding interface because of the different thermal expansion coefficients (i.e., $CTE_{CU} > CTE_{InP}$). Near the top of the chip the material is in tension. Fig. 8.3(c) shows a line plot of ε_{xx} taken 20 μm from the top of the chip and here the strain in slightly positive indicating tension there. The reason for this is that the chip is bent slightly by the bonding stress at the bottom, compressing it at the bottom and stretching it at the top.

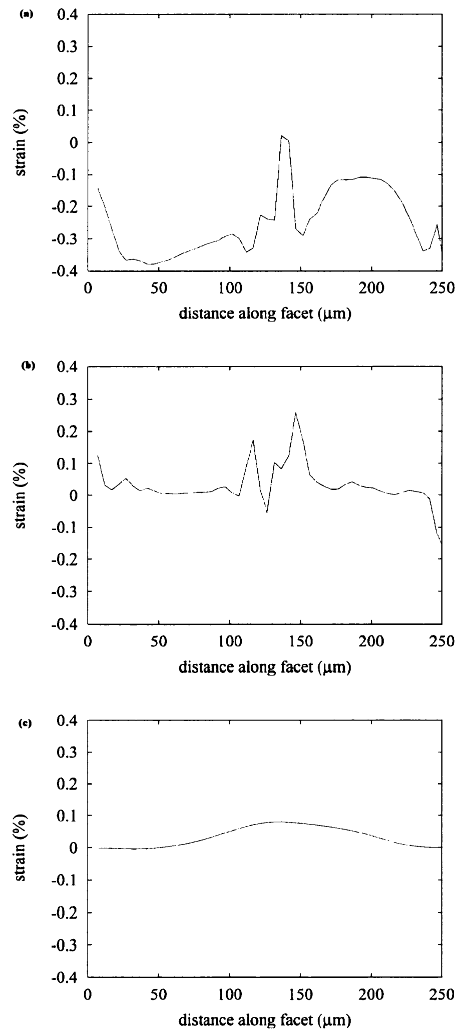

Fig. 8.3 Strain data extracted from the FEM model. (a), ε_{xx}, and (b), ε_{yy}, are along horizontal lines taken 5 μm from the bottom of the chip. (c), ε_{xx}, is along a horizontal line taken 20 μm from the top of the chip.

8.3 FEM Fits of Chips on Pre-Deposited Carriers

A number of DOP and ROP maps from the experiments in Chapter 5 were fit to using the FEM fitting routine. The modelling parameters are similar to those described in the previous section and the fitting took approximately the same length of time to complete. Line plots of strain were extracted from the FEM models to compare the die bonds of the devices. In Fig. 8.4 is shown a plot of ε_{xx} strain following a horizontal line at the facet, 20 μm above the bottom of an unbonded device, such as in the DOP map at the top of Fig. 5.2. As can be seen,

the strain along the line from the bonding interface is negative, or compressive, which is a result of the contact metallization. The shape of the plot owes to the metallization pattern. There are three valleys in the plot and they roughly correspond to the metal pads at the corners and the metal stripe down the centre of the chip (as in Fig. 5.2). The metal deposition occurs at an elevated temperature and metal films such as Au and Pt have higher thermal expansion coefficients than InP (as in Table 3.1) so there is compressive strain in the chip from the metal film deposition following the pattern of the metallization.

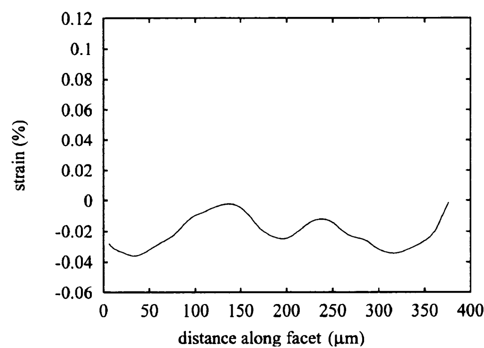

Fig. 8.4 Strain data extracted from the FEM model of an unbonded chip. It is ε_{xx} strain along a horizontal line 20 μm from the bottom of the chip.

Figure 8.5 is an example fit of a chip from the reflow time experiment. On the left are the measured DOP (top) and ROP (bottom) maps from a chip in Chapter 5. On the right are the modelled DOP (top) and ROP (bottom) maps from the FEM fitting code. The match is good between the measured and modelled data. The red and blue lobes show good correspondence between the measured and modelled maps. The key traits of the DOP and ROP measurements have been reproduced in the simulation.

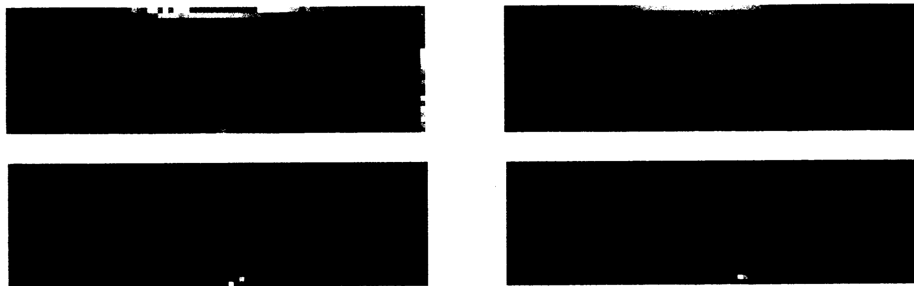

Fig. 8.5 False colour images of measured (left) and modelled (right) maps for the DOP (top) and the ROP (bottom) of a bonded chip.

In Fig. 8.6 there is strain data extracted from the fitted model of Fig. 8.5. This is ε_{xx} strain along a horizontal line 20 μm from the bottom of the chip. The data were extracted from the model along this line because at this distance from the bonding interface it shows the features of the bonding strain well. Further away, the bonding strain is averaged out too much in the material and it is difficult to see features (the superposition of the strains owing to the tractions is smoothed out). Too close to the interface and the extracted data appears "noisy." The tractions that simulate the effects of the bonding stress are applied on the bottom of the model chip. Extracting data from the model very close to where the tractions are applied can result in a jagged or "noisy" looking line plot of strain since there is little room for any smoothing by the superposition of the strains from the individually applied tractions.

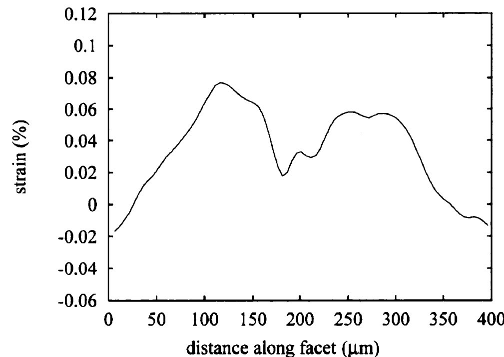

Fig. 8.6 Strain data extracted from the FEM model of the chip in Fig. 8.5. It is ε_{xx} strain along a horizontal line 20 μm from the bottom of the chip.

There are two main peaks in Fig. 8.6 on either side of the middle and a small bump near the centre. The main peaks are each about 75 μm from the centre of the plot and the maximum strain values are in the order of 0.06 % to 0.08 % there. It is believed that as the chip and carrier cooled after bonding, thermal stress built up in the solder pads in contact with the chip, which resulted in the strain in the laser. Since the carrier is made of silicon it has a lower CTE than the InP chip and so the chip contracts less as the bonded package is cooled from the solder freezing point. The result is tensile (positive) strain in the chip. The non-uniform tensile strain shown in the extracted strain plot in Fig. 8.6 is a result of the pattern of the solder on the carrier and the pattern of the contact metallization on the chip. The tensile strain in the chip from die bonding would have been offset somewhat by the compressive strain already in the chip owing to the metallization pattern (as shown in Fig. 8.4).

The main peaks in the strain profile are roughly over the open spaces in the solder pattern. This suggests that the stresses on both sides of the chip were pulling the chip apart by the solder pads. Between the solder pads there would be

no forces applied but that area would still be strained by the stresses at the ends. At the metallization stripe in the middle, the compressive strain from the metallization would have offset the bonding strain there, resulting in the dip in the profile. At the ends, the compressive strain from metallization pads on the chip would also have offset the tensile bonding strain in those areas. The strain plot is not symmetric and this is because the bonding may not have been symmetric across the bottom of the chip. This may be due to wetting, solder spreading, a non-uniform contact force on the chip during bonding, or a slight misalignment of the chip metallization pattern and the solder pattern.

The false colour maps in Fig. 8.7 show the measured (left) and modelled (right) of the DOP (top) and ROP (bottom) maps for a chip bonded in the reflow temperature experiment. Here, again, the fit is quite good in that the principal features of the measured data have been reproduced well in the model. In Fig. 8.8 is a line plot from the modelled chip in Fig. 8.7, taken 20 μm from the bonding interface at the bottom. It is an example of a strain profile that is slightly more symmetric than the previous one. The two peaks on either side of the centre are closer together than the fit in Fig. 8.6. The magnitudes of the peaks are approximately 0.09% to 0.10%. In this plot, there is no small bump at the centre, which contrasts with the previous one. It is a smoother plot which may indicate more uniform bonding. The higher strain values along the line plot indicate a stronger bond (the minimum value in between the two peaks is almost the same as the maximum peak values in Fig. 8.6).

Fig. 8.7 False colour images of measured (left) and modelled (right) maps for the DOP (top) and the ROP (bottom) of a bonded chip.

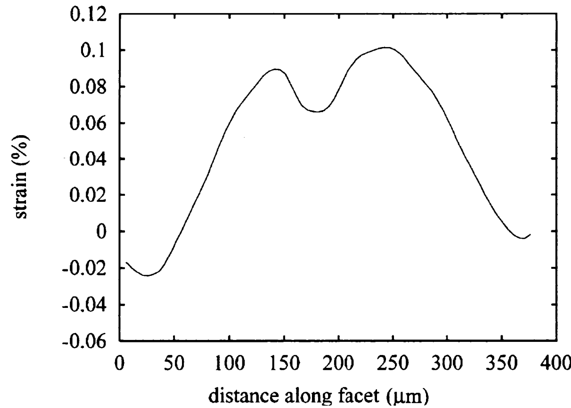

Fig. 8.8 Strain data extracted from the FEM model of the chip in Fig. 8.7. It is ε_{xx} strain along a horizontal line 20 μm from the bottom of the chip.

By looking at plots of strain along horizontal lines at different distances from the bottom of the chip, it is possible to see how the strain changes moving up the facet of the chip. For example, it was already mentioned that moving away from the bonding interface leads to smoother strain plots because the superposition of the strains in the bulk material of the chip owing to the bonding stresses at the bottom averages out further away from the stresses. This is visible in Fig. 8.9 which is a series of plots of strain taken from the chip in Fig. 8.7. On the left side (a, c, e, g, i, and k) are plots of ε_{xx} across lines at the facet and on the right (b, d, f, h, j, and l) are plots of ε_{yy} along the same line. The extracted lines are horizontal and are the following distances from the bottom of the chip: (a)(b) → 10 μm, (c)(d) → 30 μm, (e)(f) → 50 μm, (g)(h) → 70 μm, (i)(j) → 90 μm, and (k)(l) → 110 μm. Looking at the left side, it is apparent in the plots of ε_{xx} that the features from the bonding strain pattern decrease the further away one moves from the bottom of the chip (moving downwards in the set of plots). Near the top of the chip, in (k), the plot of ε_{xx} is a smooth, curved profile. In addition, the signs of the strains switched from positive (tension) to negative (compression) approximately between 70 μm and 90 μm, meaning that the material is unstrained in this region. Near the top of the chip, in (k), the maximum value of ε_{xx} is more that 0.05% in compression. As explained before from Fig. 8.3(c) this is because the chip is bending from the bonding stress at the bottom, although here it is bending the opposite way since the carrier here has a lower CTE rather than a greater CTE as in Fig 8.3. The ε_{yy} plots on the right side show that the ε_{yy} component of strain is less than the ε_{xx} and that moving further away the curvature is opposite to ε_{xx}. That is, near the top of the chip where the ε_{xx} component of strain is in compression (negative) the ε_{yy} component of strain is slightly in tension (positive) owing to the elastic properties of the material (a unit cell of material near the top that is being compressed in the x-direction will expand in the y-direction).

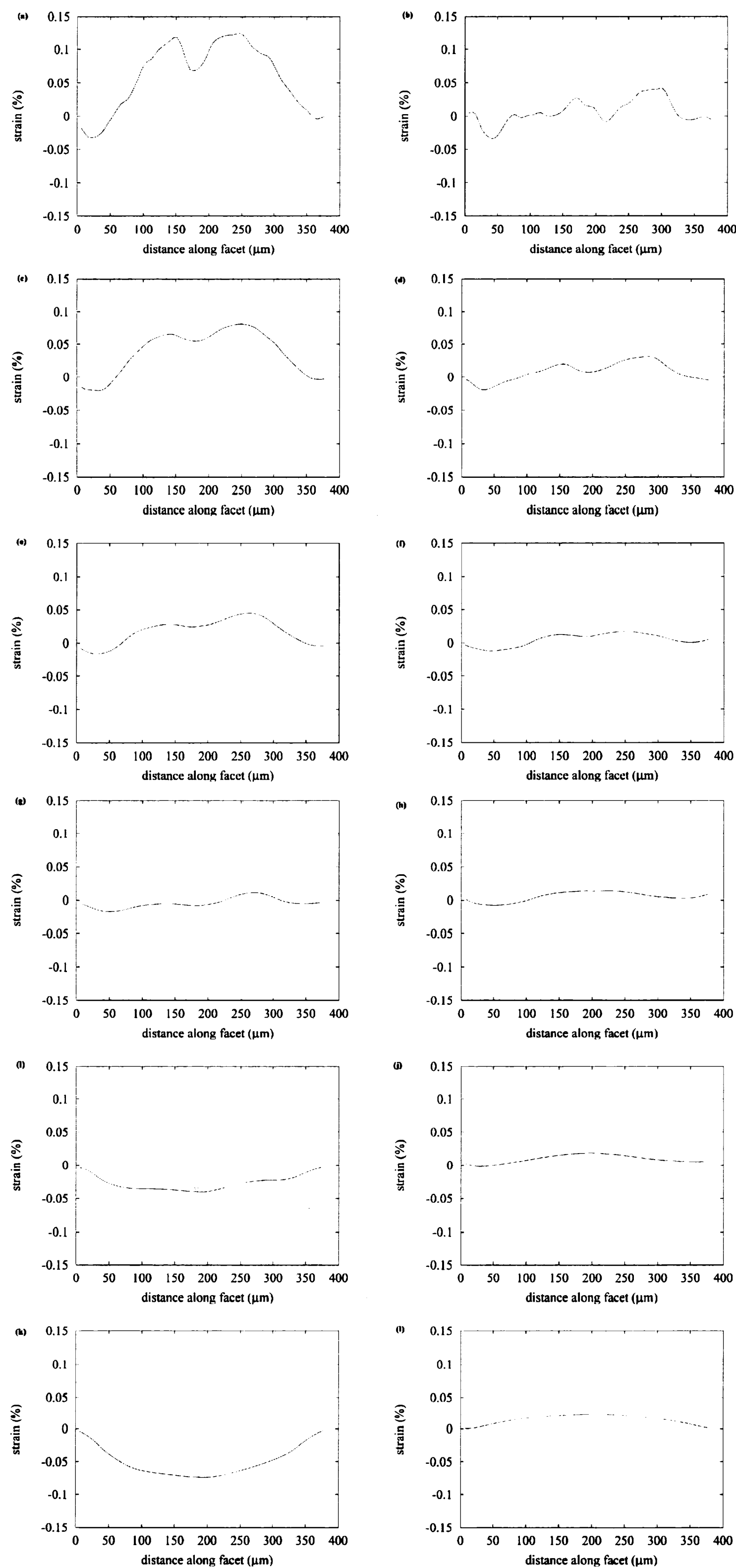

Fig. 8.9 Strain data extracted from the FEM model of the chip in Fig. 8.7 to show how the strain changes at different positions on the facet. On the left side are ε_{xx} strain plots taken at: (a) 10, (c) 30, (e) 50, (g) 70, (i) 90, and (k) 110 μm. On the right side are ε_{yy} strain plots taken along the same lines at: (b) 10, (d) 30, (f) 50, (h) 70, (j) 90, and (l) 110 μm.

An example of a device that was bonded quite differently is given in Fig. 8.10. This is a chip bonded in the reflow time experiment. The false colour images again show the measured (left) and modelled (right) maps of the DOP (top) and ROP (bottom) for the facet of the chip. Comparing them, the salient features of the measured data are modelled well in the fit. The quality of the fit is quite high for this example as the model was able to reproduce the details of the measurements particularly well.

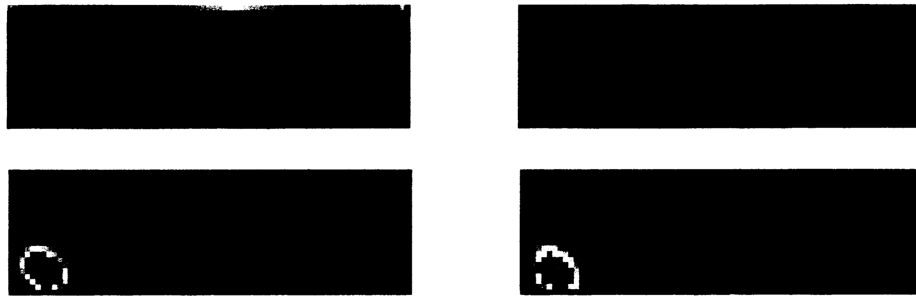

Fig. 8.10 False colour images of measured (left) and modelled (right) maps for the DOP (top) and the ROP (bottom) of a bonded chip.

In Fig. 8.11(a) is a line plot 20 μm from the bottom of the chip and it shows that the ε_{xx} strain values are quite asymmetric owing to the die bonding. The principal peak, with a maximum of 0.06 % in tension, is approximately 100 μm from the left edge. That peak is essentially over the top of the solder pad on the left side and is significantly greater than a weaker peak on the right. For this to be the case the bond on the left must be stronger than on the right. This may point to a larger surface area bonded on the left compared with the right which indicates that the left solder pad must have wet the contact metallization better and formed a superior bond than on the right. The shape of the plot is quite bumpy and this also suggests uneven bonding. Looking at Fig. 8.11(b) there are two line plots of the ε_{yy} strains extracted from the model along a *vertical* line from the bottom of the chip to the top, taken from different horizontal positions. Each line is taken 100 μm from the horizontal centre of the chip and it is obvious that the magnitude of the strains are different on either side of centre. The plot from the one that is right of centre is a solid line and the plot from the one left of centre is a dashed line. The negative ε_{yy} strain is a result of the elastic properties of the chip as explained previously. The tensile ε_{xx} strain necessarily leads to a contraction in the y-direction and ε_{yy} diminishes in negative values moving further away from the bonding interface, as seen in the figure. The strain is significantly greater on the left (solid line) than the right (dashed line). The strain profiles in Figs. 8.6 and 8.8 point to a die bond attached roughly according to the solder pattern, but the strain data for this chip is not consistent with this. The chips and

carriers were essentially identical yet the resulting bonding strain was significantly different. This likely resulted from a misalignment of the chip on the carrier in conjunction with uneven solder wetting. It seems clear from this analysis that the bonding strain in these chips bonded onto these carriers is quite sensitive to the bonding conditions.

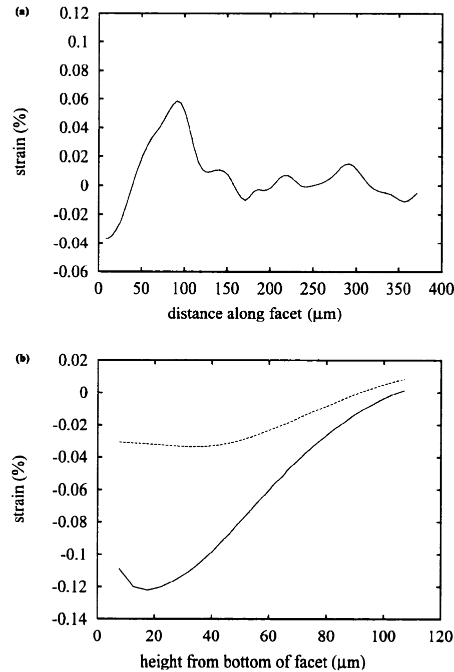

Fig. 8.11 Strain data plots extracted from the FEM model of the chip in Fig. 8.10. In (a) is ε_{xx} strain along a horizontal line 20 μm from the bottom of the chip. In (b) are ε_{yy} strain plots along *vertical* lines 100 μm to the left of the centre of the chip (solid line) and 100 μm to the right of the centre of the chip (dashed line).

A further example of a FEM fit to a bonded chip is shown in Fig. 8.12. As before, the measured maps are on the left and the modelled maps are on the right. This is from the reflow time experiment. A plot of ε_{xx} data taken 20 μm from the bottom of the chip is in Fig. 8.13. Here, there are a few peaks of strain along the extracted line with values of around 0.1%. This unevenness in the extracted strain is an indicator of the die bond. The solder is not contacted with the chip the same as the chips in Figs. 8.6, 8.8, or 8.11. From this strain information, the die attachment is uneven along the bonding interface and it appears to be a stronger attachment on the right side. Ultimately what this shows is that there is a significant amount of variability in the strain owing to die bonding for these chips and carriers. The use of solder patterns and the spreading of solder because of intermittent wetting results in different strain in the chips. These chips were all

bonded under basically the same conditions and the chips and carriers came from the same batches of materials, yet the resulting die bonds were quite different.

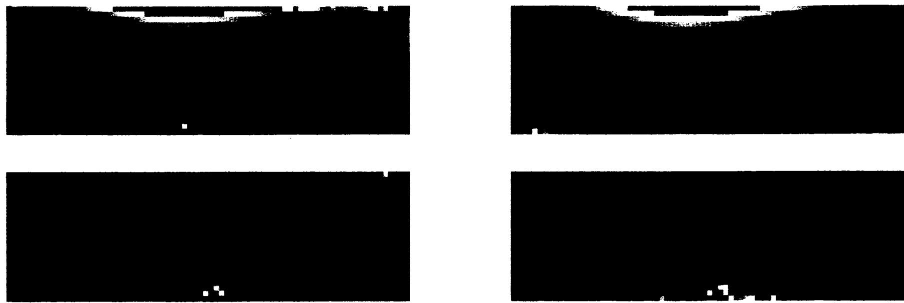

Fig. 8.12 False colour images of measured (left) and modelled (right) maps for the DOP (top) and the ROP (bottom) of a bonded chip.

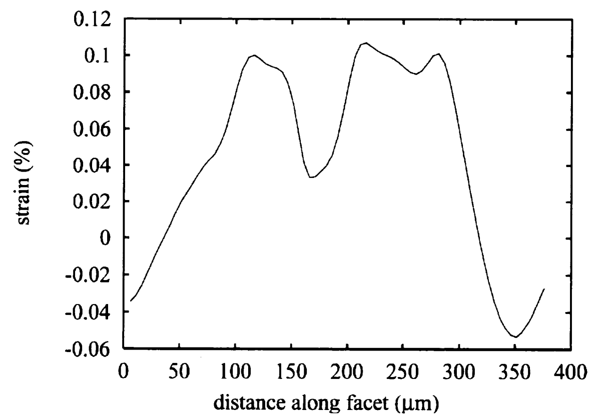

Fig. 8.13 Strain data extracted from the FEM model of the chip in Fig. 8.12. It is ε_{xx} strain along a horizontal line 20 μm from the bottom of the chip.

8.4 Photoelastic Effect Owing to Die Bonding

In this section, the effect of bonding strain on optical guiding will be discussed. Strain influences the operation of diode lasers through the photoelastic effect.[11] The dielectric permittivities, hence the refractive indices, for different orientations in a crystal are, in general, functions of the strain in the material.[18] As seen in the previous section, the strain that results from die bonding is often not uniform. This is in contrast with the strain that results from an epitaxial layer mismatch in which case it may be possible to predict accurately the strain from the known material parameters. For this reason it is necessary to determine the bonding strain in a laser and to use this data to predict the changes in an optoelectronic device.

8.4.1 Experimental Procedure

The chip that is described in this section is an InP diode laser that was bonded p-side down onto a silicon carrier, from the experiments of Chapter 5. After die bonding, the induced strain was determined from a best fit FEM model. It was then possible to extract all the strain components and then compute the changes in refractive indices, as a result of the photoelastic effect, owing to die bonding.

The change in the relative dielectric impermeability tensor B_{ij} owing to stress is expressed as $\Delta B_{ij} = \pi_{ijkl}\sigma_{kl}$.[18] In an InP based laser, the facet is a (110) cleavage plane so the photoelastic tensor π must be rotated by 45°. For a $\bar{4}3m$ cubic crystal like InP there are only three independent components in the fourth rank π tensor (π_{11}, π_{12}, π_{44} using the matrix notation). After the tensor is rotated, the photoelastic effect for the three normal directions can be expressed in terms of the stresses as:

$$\begin{aligned} \Delta B_{xx} &= \pi_{11}\sigma_{xx} + \pi_{12}\sigma_{yy} + \pi_{12}\sigma_{zz} \\ \Delta B_{yy} &= \pi_{12}\sigma_{xx} + \frac{\pi_{11} + \pi_{12} + \pi_{44}}{2}\sigma_{yy} + \frac{\pi_{11} + \pi_{12} - \pi_{44}}{2}\sigma_{zz} \\ \Delta B_{zz} &= \pi_{12}\sigma_{xx} + \frac{\pi_{11} + \pi_{12} - \pi_{44}}{2}\sigma_{yy} + \frac{\pi_{11} + \pi_{12} + \pi_{44}}{2}\sigma_{zz} \end{aligned} \tag{8.1}$$

From the relative dielectric impermeabilities, the changes in refractive indices in the different orientations can then be determined:[18]

$$\begin{aligned} B_{ii} &= \frac{1}{n_{ii}^2} \\ \therefore\ \Delta B_{ii} &\approx \frac{-2}{n_{ii}^3}\Delta n_{ii} \\ \text{or}\ \ \Delta n_{ii} &\approx -\frac{1}{2} n_{ii}^3 \Delta B_{ii} \end{aligned} \tag{8.2}$$

The FEM model was fit to both normal and shear components by way of the DOP and ROP measurements. By the symmetry of InP the changes in the refractive indices in the three normal directions are functions of only the normal stress components. The piezo-optical coefficients π_{ij} were calculated from the elasto-optical coefficients p_{ij} which have been measured for InP.[64] The piezo-optical coefficients calculated for InP are

$$\left.\begin{array}{l}\pi_{11} = -1.103 \\ \pi_{12} = -0.323 \\ \pi_{44} = -1.266\end{array}\right\} \mathrm{x}10^{-12}\ \mathrm{m^2/N\ at\ 1.55\ \mu m.}$$

The refractive index used in (8.2) to calculate the change in refractive index is n = 3.167 for InP at 1.55 μm.[65]

Once the changes in the refractive indices along orthogonal orientations were computed, the effects of these changes on the laser were determined. A commercial mode-solving software package was used to simulate the effects of the bonding strain on a waveguide. The package used the alternating-direction-implicit finite difference iterative method to model the waveguide.[66] The structure that was simulated was a ridge waveguide and is shown in Fig. 8.14. The structure was a 5 μm wide InP ridge capped with a 0.10 μm layer of lattice matched InGaAs. The active region was 0.85 μm below the ridge (which has a set-off of 0.60 μm). The active region was modelled as a 0.15 μm layer of lattice matched InGaAsP. Because this was a weakly guided structure, the effect of the strain would be more pronounced in it than in a strongly guided device. The simulation was run using a Gaussian starting field with a wavelength of 1.55 μm.

The changes of refractive indices were incorporated into the waveguide model by breaking the structure into elements similar to the finite element model and then applying the altered indices to these elements. The guided mode was first simulated with the structure unstrained, that is, without incorporating the refractive index changes. The mode-solving package was then used to compute the guided mode with the changes in the refractive indices included from the FEM fit. The differences of the guided mode with and without the photoelastic effect are shown in the next section.

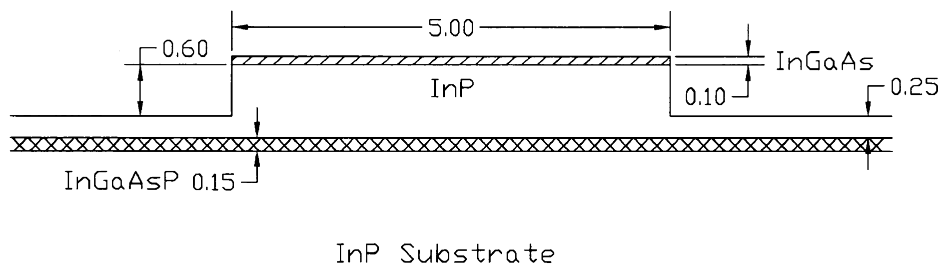

Fig. 8.14 Waveguide structure used in mode solving software. Dimensions are in μm.

8.4.2 Results and Discussion

8.4.2.1 Waveguide Mode

The solder induced varying amounts of strain in different parts of the diode laser. This variation in the strain manifested itself in the photoelastic effect as shown in Fig. 8.15. This is data calculated using the FEM model fitted to the measured DOP and ROP values at the facet of the laser. The change of refractive indices in the TE polarization direction are shown along a line parallel to the bonding interface, 5 μm from the bottom of the chip.

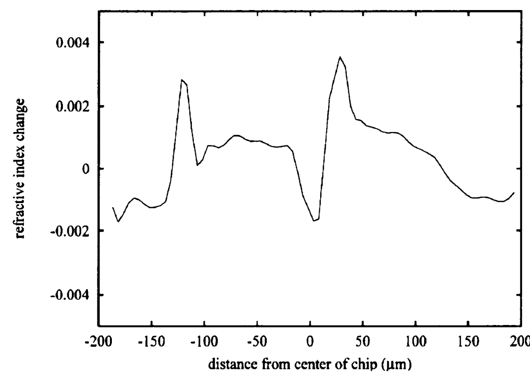

Fig. 8.15 Photoelastic effect in TE polarization along horizontal line at the facet, 5 μm from bottom of chip.

From this line plot it is clear that the refractive index change is quite variable across the width of the chip because of the die bonding. The DOP and ROP data are representative of the strain near the surface of the facet. It has been found that the strain fields at the facet correspond to the strain along the cavity in diode lasers.[67] While the bonding strain along the length of the device could be somewhat variable, it is reasonable that it would be similar to that found at the facet. The consequence of the photoelastic changes in the refractive indices on the waveguide was determined with the mode-solving software. As a simplification it was assumed that the refractive index changes were constant along the length of the waveguide so that the problem could be treated as a two-dimensional calculation.

Using the mode solver for the case of the unstrained structure a single mode solution was found with a dominant TE polarization for the waveguide. This mode was centered with the ridge laterally and with the quaternary active layer transversely, as designed. Like with most diode lasers the mode was ellipsoidal. Figs. 8.16 and 8.17 show the lateral and transverse mode profiles for the mode in the waveguide. These show the shape of the mode as transverse and lateral slices with the field amplitude normalized.

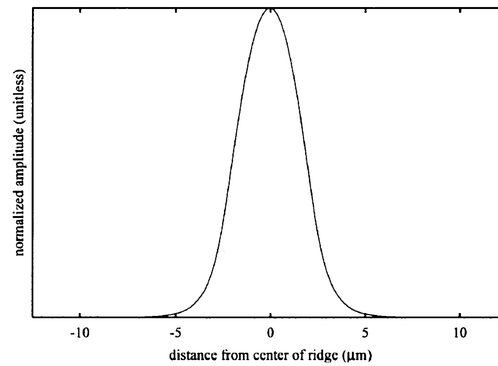

Fig. 8.16 Lateral mode profile along active region for an unstrained waveguide.

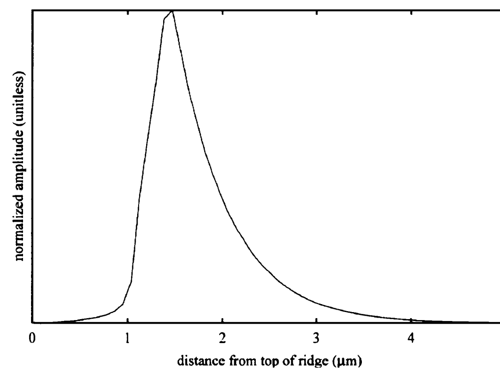

Fig. 8.17 Transverse mode profile near edge of ridge for an unstrained waveguide.

When the simulation was run with the altered refractive indices owing to the photoelastic effect from the die bonding the results were somewhat different. This is visible in Figs. 8.18 and 8.19 which show the lateral and transverse mode profiles at the same points in the structure as in Figs. 8.16 and 8.17. In both of these plots a normalized field amplitude is presented. Clearly the lateral mode profile is not symmetric any longer. The changed refractive indices have had an effect on the mode in the waveguide. There was leakage from the central peak into a side lobe of the mode.

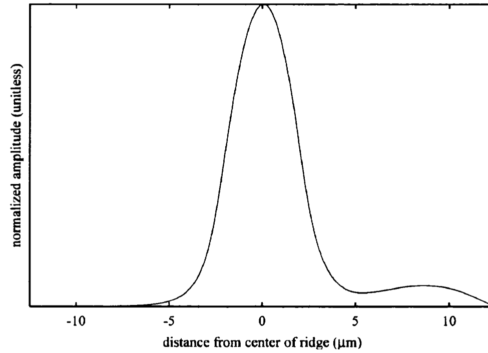

Fig. 8.18 Lateral mode profile along active region for waveguide with altered refractive indices owing to the die bonding.

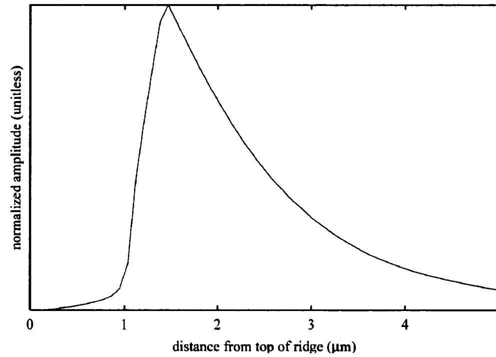

Fig. 8.19 Transverse mode profile near edge of ridge for waveguide with altered refractive indices owing to the die bonding.

In the transverse profile, the decay into the substrate was slower in the strained case than the unstrained case. The different refractive indices changed the structure enough that the field extended further into the substrate than with the unstrained structure. The full width at half maximum (FWHM) for the lateral mode profile increased from 3.95 μm to 4.20 μm, comparing the unstrained and strained guide modes. For the transverse case, the full width at half maximum for the mode profile increased from 0.68 μm to 1.25 μm. Both the lateral and transverse optical confinement were reduced, allowing the mode to expand out. The confinement factor, which gives the proportion of the integrated energy of the mode that is contained in a defined region, was calculated for each case. For this calculation the boundaries were set at ± 2.5 μm (width of the ridge) in the lateral direction and from 1 μm below the active layer to the top of the ridge in the transverse direction. For the unstrained structure the confinement factor was 98.1% whereas for the structure with the altered refractive indices it was 89.6%.

The results here are specific to this structure. There are no general rules as to how a waveguide will behave in the presence of non-uniform bonding strain. The

strain needs to be determined in a bonded laser chip and the changes in refractive indices calculated and applied to the waveguide. If the structure in Fig. 8.14 was altered slightly the effect of the strain could become very great. For example the thickness of the InP cap layer in the waveguide model was increased from 0.25 to 0.35 μm and the effect of the strain on the refractive indices caused the structure to become anti-guiding; most of the mode energy spread into the substrate. With the unstrained structure this adjustment only caused a moderate change in the shape of the guided mode. In a laser, the proportion of light in the active region will affect the performance of the laser. For the simple model here, gain in the active region was not considered. Normalized values of the far field amplitudes are given here since it is unknown, in this model, how the total power in the far field would be affected in a real laser.

8.4.2.2 Far Field

The change in the mode can affect the laser and its use in a number of ways. It might modify the performance of the laser since light is now less confined. If the intensity of the light in the laser is changed then the carrier distribution would be altered. In addition the strain could affect the output of light from the device. To see how the light output is influenced by the effect of the changed refractive indices, the far fields of the guided modes were calculated and compared. The far fields were calculated from the mode-solving software using Fraunhofer diffraction theory. Figures 8.20 and 8.21 are plots of the field amplitudes in the far field for the unstrained and strained cases respectively.

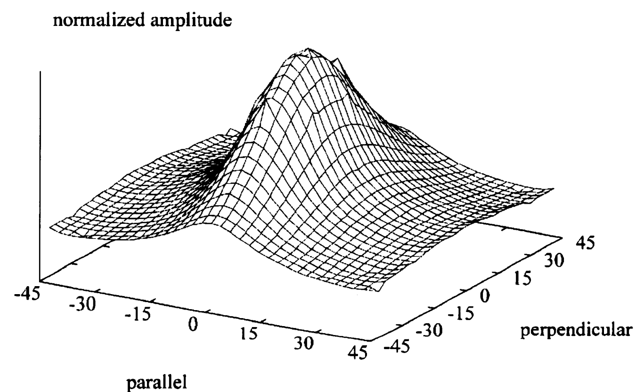

Fig. 8.20 Far field amplitude of laser output for unstrained laser structure. The axes are the angles from center and they range from - 45° to + 45° parallel and perpendicular, respectively, to the junction plane. The amplitude is normalized (unitless).

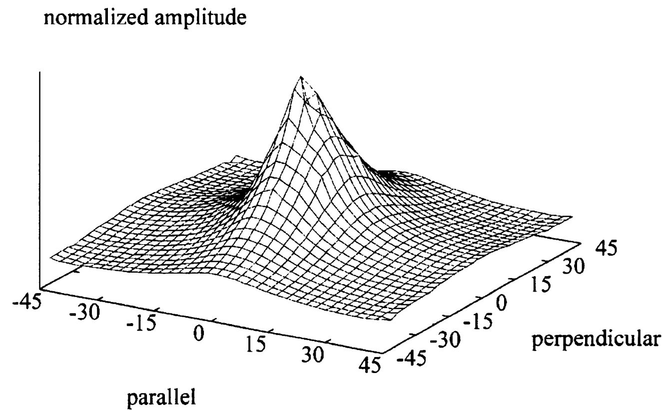

Fig. 8.21 Far field amplitude of laser output for the laser structure with altered refractive indices. The axes are the angles from center and range from - 45° to + 45° parallel and perpendicular, respectively, to the junction plane. The amplitude is normalized (unitless).

For the far field of the case without imposed changes in the refractive indices the field amplitude was Gaussian in shape, as in Fig. 8.20. The shape of the beam was ellipsoidal as would be expected given the mode in the waveguide. The full widths at half maximum were 15° and 42° for the profiles in the directions parallel and perpendicular to the junction plane, respectively. The plot in Fig. 8.21 of the far field amplitude for the strained case shows the effect of the refractive index changes in the structure. This plot is significantly different than the case for Fig. 8.20 and it is clear that in the far field the beam has been changed. Figures 8.22 and 8.23 show profiles from Fig. 8.21 of the far field of the structure with altered refractive indices.

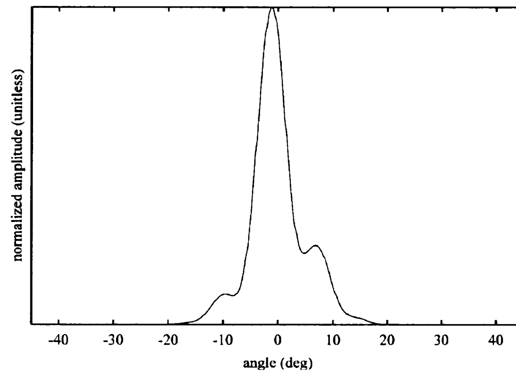

Fig. 8.22 Far field amplitude profile parallel to the junction plane.

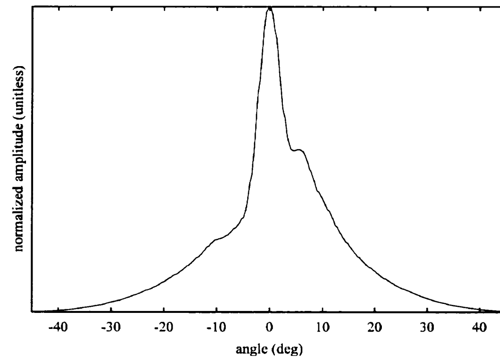

Fig. 8.23 Far field amplitude profile perpendicular to the junction plane.

It is evident that the far field is no longer a balanced pattern with the strain applied since the field amplitude profiles are not symmetric. The dips in the curves are a result of the different mode that is supported in the strained waveguide. The full widths at half maximum were 6° and 10° in the directions parallel and perpendicular to the junction plane respectively, quite distinct compared with the unstrained structure. The beam shape from this laser would be irregular and this could affect the coupling of light output from this structure. Table 8.1 shows a summary of some differences in the guiding of the unstrained and strained waveguide structures.

Table 8.1 Comparison of unstrained versus strained waveguide structure.

PARAMETER	UNSTRAINED	STRAINED
FWHM of mode (lateral)	3.95 μm	4.20 μm
FWHM of mode (transverse)	0.68 μm	1.25 μm
FWHM of far field (parallel to junction plane)	15°	6°
FWHM of far field (perpendicular to junction plane)	42°	10°
confinement factor	98.1%	89.6%

8.4.2.3 Photoelastic Effect in Diode Lasers

The photoelastic effect owing to the strain from dielectric and metallization layers has been shown in other work to affect the emission of ridge waveguide lasers. It was found that stress from metal and oxide films produced a dip in the near field emission pattern and that there was a concurrent increase in threshold current.[68] In addition, it has been demonstrated that epitaxial strain can cause TE-TM mode switching in diode lasers. Workers have shown that under certain stress levels in the active layer, caused by oxide and metal films, the mode pumping efficiency can be changed.[69] Perhaps the strain owing to die bonding can have a similar effect.

The analysis of strain in diode lasers in most work tends to use line forces or other simple models to make predictions about the strain and its effects. It has been shown that such models can, in fact, represent the strain distribution quite well.[11] In the case of strain owing to die bonding the non-uniformity of the strain often makes it impractical to use a simple model. Using degree of polarization measurements of a diode laser facet and an iterative finite element method model to estimate the components of strain allows for a reasonable prediction of the photoelastic effect in the material. Such a technique is sufficiently complex that it can provide the detailed predictions of the strain that match well with measurement and the resulting changes in refractive indices.

The photoelastic effect owing to processing induced strain is not always detrimental to laser performance. Diode laser structures have been designed to use the photoelastic effect to their advantage for optical confinement in semiconductor laser material. In certain cases strain was introduced intentionally with deposited thin films to create optical waveguides via the photoelastic effect.[70] The principal reason for such a design is simplicity; it is preferred if growth and etch steps can be eliminated from the processing of a laser. A photoelastic waveguide would obviously be very susceptible to the effects of bonding induced strain if bonded p-side down since the index difference creating the optical confinement in a photoelastic waveguide is small to begin with. Weakly guiding devices like ridge waveguides are also vulnerable to the effects of die bonding strain as was shown with the far field patterns in this section. For photoelastic waveguides the situation would likely be worse since the guiding is even weaker.

8.5 Detection of Voids in Die Bonding

Voiding in diode laser packaging is an important issue for a number of reasons. The consequence of voids on the thermal impedance of a bond is of most concern. Voids reduce the total area of a bond through which heat can dissipate, increasing the thermal impedance. This has a harmful effect on the performance of a bonded device since diode lasers are very sensitive to temperature. Voids in the

die bonds of electronic and optoelectronic components have been measured using scanning acoustic microscopy and X-ray imaging. The strain pattern that voids can cause is another way of detecting them. When the thermal strain that is a result of materials with dissimilar coefficients of thermal expansion (CTE) is not constant along an interface it indicates that the joint is not continuous. In a case in which the adherends are not in contact with the adhesive the strain is lowered locally since there are no forces where there is no contact.

To illustrate the effect of voids, finite element method models of die bonding without and with voiding are shown in Figs. 8.24 and 8.25.

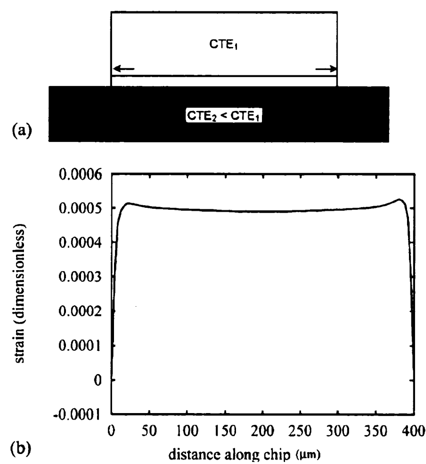

Fig. 8.24 Finite element method model of strain owing to die bonding in die bond that is free of voids. (a) Diagram of chip with coefficient of thermal expansion CTE_1 bonded to chip carrier with CTE_2. (b) Plot of strain in the chip along line 5 μm from the bonding interface.

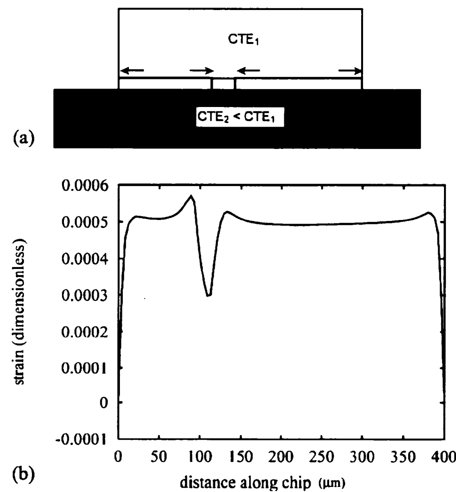

Fig. 8.25 Finite element method model of strain owing to die bonding in die bond with a void. (a) Diagram of chip with coefficient of thermal expansion CTE_1 bonded to chip carrier with CTE_2. (b) Plot of strain in the chip along line 5 μm from the bonding interface. Note the dip in the strain profile along the width of the chip due to the void.

Figure 8.24(a) shows an ideal bond without voiding for a chip (top) bonded to a carrier (bottom). The chip and carrier have different coefficients of thermal expansion CTE_1 and CTE_2. The FEM model was run to show the effect of a temperature change. In Fig. 8.24(b) is a plot of the horizontal strain components along a line 5 μm from the bonding interface. The thermal strain that is induced in the material is fairly constant in the middle and is only gradually and smoothly varying as seen in the plot. The model in Fig. 8.25(a) is similar but with the introduction of a void. Figure 8.25(b) shows the result of the void on the plot of strain. There is a dip that is a result of the lack of material in contact with the chip there. For voids that are at the facet, DOP and ROP measurements can detect them directly. In the case of voids further back from the facet there would still be some strain that should propagate to the facet and be measurable there, although weaker since the strain would be relieved somewhat through the material. In another FEM simulation similar to the ones explained above, it was found that a dip in the strain profile owing to a void was observable in a plot of strain extracted 40 μm away from the void. The dip in the plot of strain was reduced further away from the void but it was still detectable at a distance.

In Fig. 8.26 is an example of a fit to a chip that was different than the other chips shown in this Chapter. The chip had a solid bottom metallization but the carrier had a metallization pattern similar to that shown previously. In Fig. 8.26 the measured maps are on the left and the modelled ones on the right, with the DOP on the top and ROP on the bottom, as before. Since this chip had a solid metallization the solder, which was patterned, melted and adhered unevenly to the chip. The result were voids in the solder layer. The chip had a solid metallization so it introduced no distinct strain pattern in the chip itself.

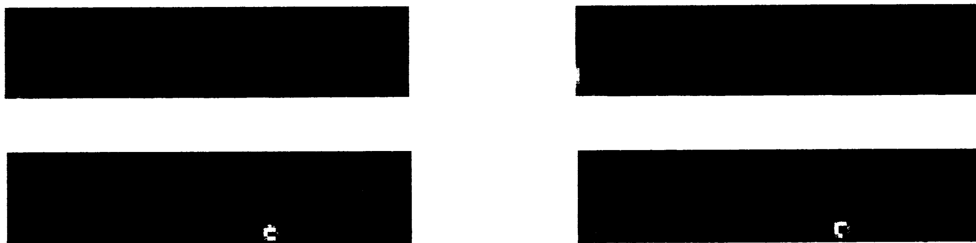

Fig. 8.26 False colour images of measured (left) and modelled (right) maps for the DOP (top) and the ROP (bottom) of a bonded chip.

The strain profile along a horizontal line 10 μm from the bonding interface is in Fig. 8.27. The dips in the strain profile around -25 μm, 50 μm, and 150 μm from the centre of the chip show where there is no bonding between the chip and carrier, i.e., a void. We can therefore detect the presence of voids that are near the facet of a diode laser using the DOP technique. This is important for qualifying die

bonding processes and materials. It could help in designing procedures and techniques to minimize voiding. The quantitative data that is a result of the FEM fitting to the DOP data is useful in knowing the position of voids. This technique is essentially non-destructive and, when compared with other methods of detecting voids such as scanning acoustic microscopy (SAM), it is much cheaper. It does not image the voids themselves like SAM but it is nevertheless able to detect their presence by their effect on the strain in the laser material. Strain due to voids that are behind the facet should be measurable even if weaker. Using DOP measurements at the front and back facets and possibly on the sides of a chip, large voids inside should be detectable. An issue with this method is that solder inhomogeneities near the edge of a chip could dominate such measurements even if the main die attach was homogeneous. Voids near the edge of a chip are observable with this method so measurements at the front and back facets, and possibly the sides of the chip could provide a more complete account of voiding. While this technique is limited, it is still capable of observing solder inhomogeneities in die bonds of laser chips.

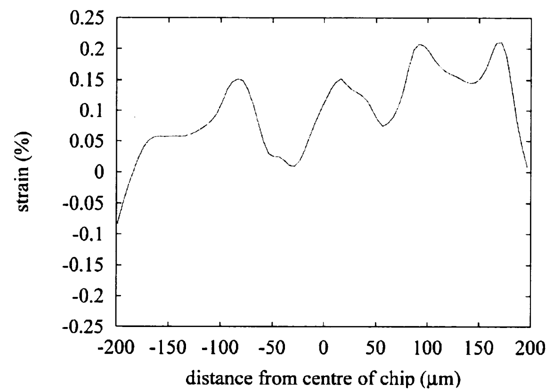

Fig. 8.27 Strain data extracted from the FEM model of the chip in Fig. 8.26. It is ε_{xx} strain along a horizontal line 10 µm from the bottom of the chip.

8.6 Summary

This chapter provided an examination of the strain in diode lasers owing to non-uniform die bonding. In particular, examples were provided of chips modelled using the finite element method iterative fitting routine. From these modelled data, components of strain were extracted along lines at the facet of the models. This helped understand the effect of die bonding on the chips. In Section 8.2, data was presented from a FEM model of a bonded device. The parameters of the fitting were provided and false colour maps of the measured and modelled DOP and ROP were compared. There was a good correspondence between the measured and modelled maps. In Section 8.3, some chips from the experiments of Chapter 5 were examined using the same technique. It was confirmed that even using similar chips and carriers, there were significant differences in the strain

owing to die bonding. This suggests some variability in the bonding, due to misalignments or perhaps intermittent solder wetting. In 8.4, the effect of bonding strain on the optical guiding of a device was explored. It was found in simulations that die bonding can affect the waveguide because of the photoelastic effect. Finally, Section 8.5 discussed using strain as a means of detecting solder voids in a die bond.

CHAPTER 9 DIE BONDING OF DISTRIBUTED FEEDBACK LASERS

9.1 Introduction

Lasers with built-in gratings are designed to provide single lasing mode operation to meet the strict linewidth requirements of certain applications such as high speed optical communications systems.[71] Distributed feedback (DFB) lasers incorporate a grating along the length of the device in the form of a periodic modulation of the index of refraction and/or gain, the purpose of which is to provide wavelength selective optical feedback along the length of the device.

It was desired in this research to also determine if diode laser operation could be affected by die bonding. This chapter explores the effect of die bonding on DFB lasers, particularly the effect of bonding strain on their spectra. A number of DFB lasers had their spectra measured before and after being die bonded. Some of the diode lasers were mounted p-side down, with the active region closest to the chip carrier, and others p-side up. In general the spectra were found to be altered. The changes in the spectra owing to the die attach procedure were measured and are shown here. These devices were bonded using epoxy since this was the only adhesive available at the time.

9.2 Experimental Procedure

9.2.1 Die Bonding

The devices used in this experiment were 1310 nm gain-coupled ridge waveguide distributed feedback diode lasers. The chip carriers to which the lasers were bonded were made of copper. The bonding material was EPO-TEK H20E conductive adhesive epoxy. This is a two part thixotropic paste that contains silver powder for electrical and thermal conduction dispersed in both the resin and the hardener components. The chips were die bonded using a semi-automatic epoxy die attach machine and cured in a temperature-stabilized oven at over 225° C for approximately 20 minutes. This is above the minimum curing schedule for this epoxy, to be sure that the chips would be well-cured for good attachment. The epoxy was deposited onto the carriers using an arm on the die attach machine. The epoxy was dispensed so that the p-down chips could be placed onto the carrier with minimal epoxy being spread out past the sides of the chips. It was attempted to make the epoxy deposition and spreading as consistent as possible from chip to chip but inevitably there were some differences in the die bonds.

Care was taken to minimize the amount of epoxy deposited too close to the edge of the carrier for the p-down mounted devices to help reduce the chance of the facet around the ridge being blocked and obstructing the output light. For this reason the p-down mounted chips were also bonded with a small amount of overhang. This helped in being able to couple light out of the p-down devices.

After die bonding, the spectra for some devices were not measurable. Some failures were intrinsic to the lasers themselves and they failed to lase or produce any light at all after being handled and bonded. Some p-down devices were unusable after bonding owing to epoxy blocking the light emission. After bonding there were 13 p-down lasers and 8 p-up lasers that were measurable.

9.2.2 Spectral Measurements

The optical spectra were measured using an Anritsu optical spectrum analyzer (OSA) with a tapered optical fiber. Coupling light out of the p-down bonded lasers was more difficult than the p-up devices since the ridge was not visible for helping to align the fiber. The lasers were placed on a temperature controlled stage and electrically contacted with fine-tipped probes (there was no wire bonding used in either the unbonded or bonded lasers). For the p-up mounted devices both the front and back facet spectra were measured. The back facet spectra could not be measured in the case of the p-down mounted devices since the back facet was not accessible by the fiber.

The unbonded spectra were all measured with the chips placed directly on the stage p-side facing up. Because of the reduced thermal impedance of the bonded devices, the spectra from the bonded lasers were each blue-shifted by a small amount since the temperature in the active regions was slightly lower. To compensate for this, the measurements of the bonded spectra were shifted back to match the unbonded spectra since it was the shape of each spectrum before and after bonding that was of interest and not the absolute values of the wavelengths. The lasing mode of each bonded spectrum was aligned with the lasing mode of the corresponding unbonded spectrum. The wavelengths in the figures are for the unbonded spectra; the bonded spectra were shifted by approximately 1 to 2 nm in each case to line up the lasing modes.

The laser spectra were measured at a number of current levels for each laser from below threshold to well above it. Threshold for these lasers was found to be approximately 12 mA. The maximum resolution of the OSA was 0.05 nm and each spectrum consisted of 2000 data points. The wavelength spans of the spectral scans were either 50 or 72 nm depending on the features being considered in a particular scan.

9.3 Results

The spectra for the devices showed various changes comparing them before and after die bonding. Some of these were quite distinct while other differences were subtle. All of the 21 devices bonded for which spectra were successfully measured showed some differences in the shape of their spectra after die bonding compared with before die bonding. Both the devices bonded p-side up and p-side down exhibited changes as a result of bonding. There was some mode flipping of the lasing mode on either side of the stopband. In the description

of the spectra, *'below'* the stopband refers to lower wavelengths (or higher frequency) and *'above'* the stopband refers to higher wavelengths (or lower frequency). There are indicator numbers in some figures of the laser spectra in this paper that are used to identify particular longitudinal modes for discussion purposes.

9.3.1 Stopband Width

Wave propagation in a medium with a periodic structure leads to a gap of wavelengths for which strong scattering occurs, the stopband.[72] The stopband width was measured from the spectra as the separation in the peaks of the two modes immediately on either side of the stopband. A majority of devices showed a decrease in stopband width with die bonding. From the 21 devices, 11 of them had decreased stopband widths, 7 of them were unchanged, and 3 had increased stopband widths. The changes in the stopband widths were quite varied from a decrease of 4.9% to an increase of 3.8%. The mean change in stopband width was a decrease of 0.9%. Figure 9.1, which depicts a device with very well matched spectra before and after die bonding, shows a stopband that is unchanged.

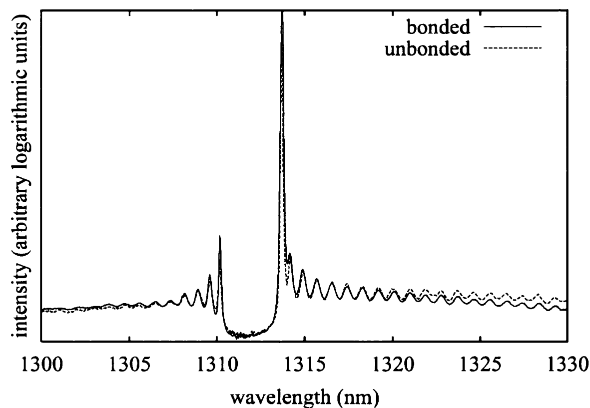

Fig. 9.1 Unbonded (dashed) and bonded (solid) spectra of a p-up mounted diode laser at 21.5 mA. The bonded spectrum was shifted in order to align with the unbonded spectrum for comparison.

The spectrum for this device, as well as for all spectra shown, was measured above threshold at a current of around 20 mA. The modes in the before and after spectra are nearly identical. The only substantial difference in shape for this p-up mounted device is the size of the dip between the lasing mode and the second mode on the right. Figure 9.2(a) is an example of a device which exhibited a decrease in its stopband width. With the lasing modes aligned in the two overlapping spectra, the decrease in the stopband width of 3.5% is evident in the mode immediately to the left in the lower wavelength region below the stopband. This is more evident in Fig. 9.2(b) which is an expanded view of the spectrum in

that area. Figure 9.2(c) is an enlarged view of the right in the higher wavelength region above the stopband.

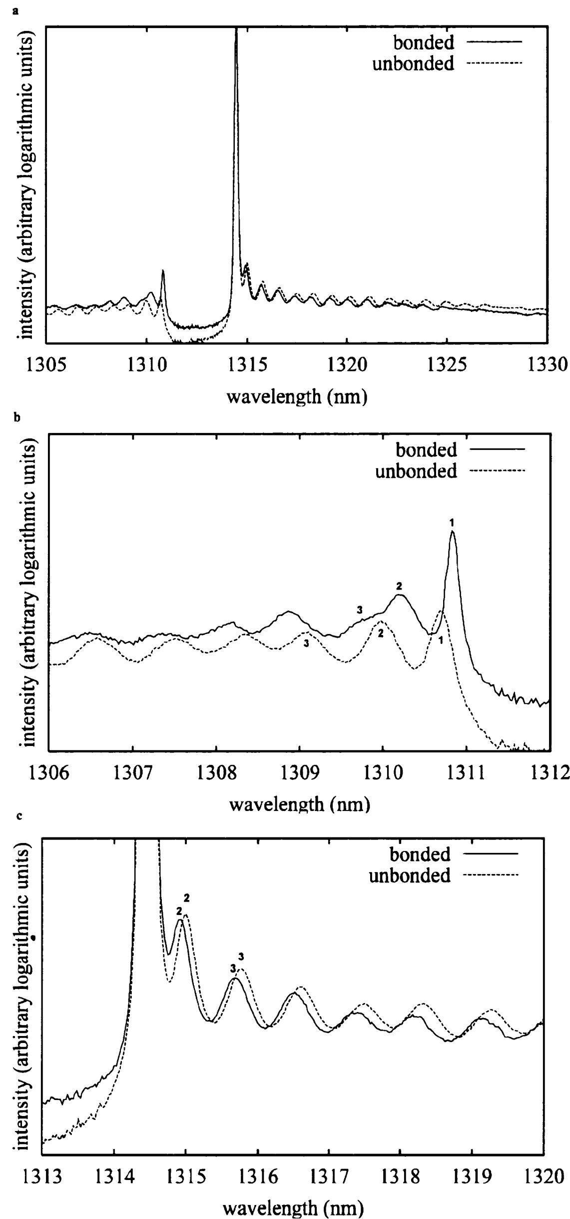

Fig. 9.2 Unbonded (dashed) and bonded (solid) spectra of a p-down mounted diode laser at 20 mA. (a) Wide view of the spectra. (b) Expanded view of the modes below the stopband. (c) Expanded view of the modes above the stopband. The reference numbers in (b) and (c) help to identify the modes. The bonded spectrum was shifted in order to align with the unbonded spectrum for comparison.

9.3.2 Modes

The change in the stopband width is an indicator of the Bragg modes changing in general with die bonding. When the spectra are superimposed on one another in Fig. 9.2 such that the lasing mode of each spectrum matches, the other modes on either side of the stopband do not align. For this laser, the stopband decreased by 3.5% upon die bonding. The modes above the stopband in the bonded case follow the shape of the modes of the unbonded spectra fairly consistently, however there is an offset which seems to occur due to the spacing of the second and third modes with respect to the lasing mode, as in Fig. 9.2(c). With the lasing modes aligned for the unbonded and bonded spectra, the separation between the lasing mode and the second mode decreased by 13% in the bonded spectrum. This narrowing of the mode spacing in the first two Bragg modes above the stopband caused the other modes to be offset. In the region below the stopband, the changes are more significant. The first two modes of the bonded spectrum, in Fig. 9.2(b), seem to correlate with the unbonded spectrum but are shifted inward toward the stopband. The third mode, clearly visible in the unbonded spectrum, seems to have shifted considerably and is visible only as a hump on the side of the second mode in the bonded case. The other modes in the bonded spectrum visible in Fig. 9.2(b) have shifted to the right, towards the stopband. Overall, the bonding appears to have affected the Bragg modes around the stopband in such a way that the stopband has narrowed and the modes nearby have been shifted inwards.

Figure 9.3(a) shows the unbonded and bonded spectra of a device mounted p-side down. The before and after bonding spectra match quite closely in the modes above the stopband including the lasing mode bounding the stopband. The spectra are quite different below the stopband. The Bragg modes do not align in this region at all. This is more visible in Fig. 9.3(b) which is an expanded section of this part of the spectrum. The magnitudes of the Bragg modes have increased on this side of the stopband and they have shifted as well. This spreading out of the Bragg modes results in the very visible differences in the spectra below the stopband. While the first mode below the stopband is aligned and the stopband width is the same in both spectra, the second mode has changed greatly. This mode in the spectrum of the unbonded laser is quite weak and almost not noticeable except in the expanded plot. It has grown considerably in magnitude and in breadth in the bonded device and is distinct even in the wide view of the spectrum. The largest difference between the two spectra is the gap between the second and third modes in Fig. 9.3(b). The third mode in the unbonded spectrum does not correspond with any mode in the bonded spectrum. It has disappeared upon die bonding, leaving a flat section in the spectrum between the second and third modes of the bonded spectrum.

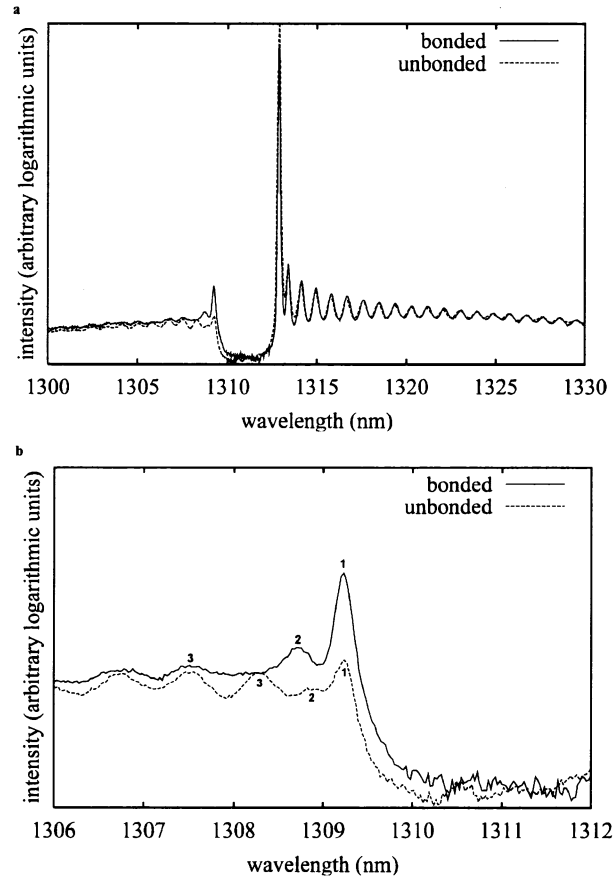

Fig. 9.3 Unbonded (dashed) and bonded (solid) spectra of a p-down mounted diode laser at 20 mA. (a) Wide view of the spectra. (b) Expanded view of the modes below the stopband. The reference numbers in (b) help to identify the modes. The bonded spectrum was shifted in order to align with the unbonded spectrum for comparison.

The comparison of the unbonded and bonded spectra of the device in Fig. 9.4(a) is another example of changes in the Bragg modes immediately surrounding the stopband affecting the overall spectrum. The stopband width in this p-down mounted laser was unchanged in the bonded spectrum compared with the unbonded spectrum yet the mode spacing changed enough to make the Fabry-Perot modes be misaligned on either side. In Fig. 9.4(b), the separation between the second and third modes from the left decreased by 23% upon bonding. This shift resulted in the rest of the modes to the left being offset in the bonded versus unbonded spectra. Above the stopband the mode spacing between the lasing mode and the second mode also decreased, by 10%. The result on this side is also a shifting of the modes and a misalignment of the Fabry-Perot modes further away.

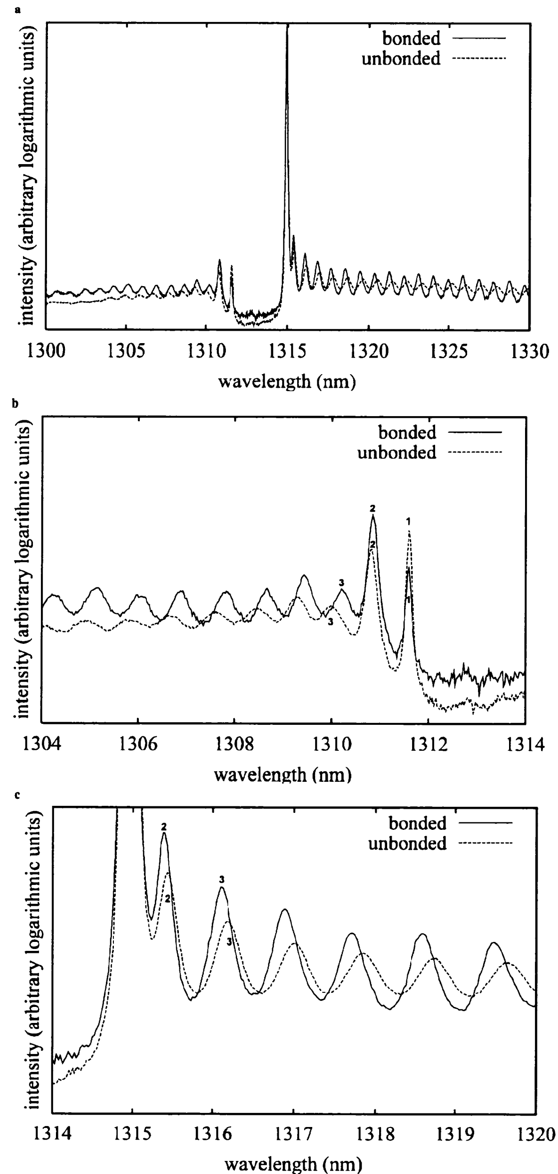

Fig. 9.4 Unbonded (dashed) and bonded (solid) spectra of a p-down mounted diode laser at 20 mA. (a) Wide view of the spectra. (b) Expanded view of the modes below the stopband. (c) Expanded view of the modes above the stopband. The reference numbers in (b) and (c) help to identify the modes. The bonded spectrum was shifted in order to align with the unbonded spectrum for comparison.

With the lasers mounted p-side up there tended to be less noticeable changes, on average, in the bonded lasers upon die bonding but there still were effects observed. One example is in Fig. 9.5(a). In this case the modes above the stopband seem to fit relatively well with a small shift and a change in the relative magnitudes of the Fabry-Perot modes. Below the stopband, the change is much

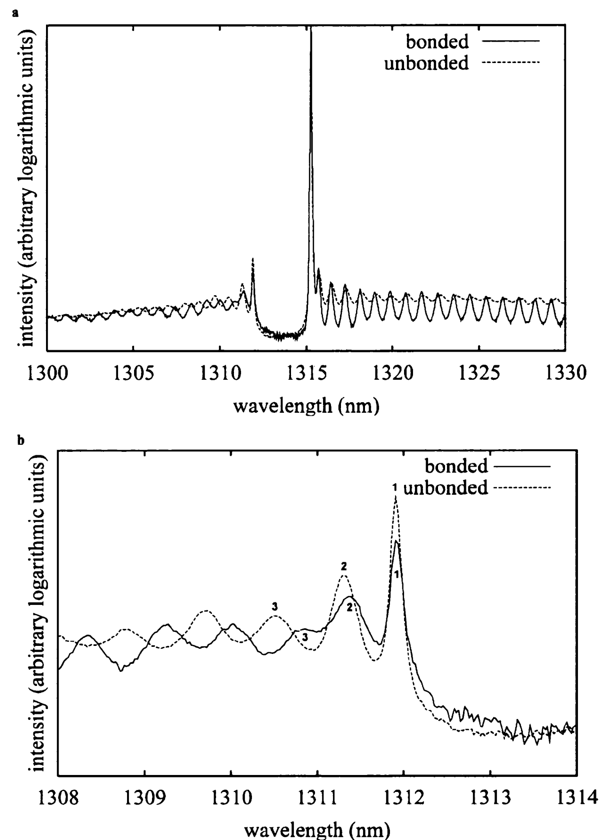

Fig. 9.5 Unbonded (dashed) and bonded (solid) spectra of a p-up mounted diode laser at 20 mA. (a) Wide view of the spectra. (b) Expanded view of the modes below the stopband. The reference numbers in (b) help to identify the modes. The bonded spectrum was shifted to align with the unbonded spectrum for comparison.

more apparent, as seen more easily in Fig. 9.5(b). The first mode on the left, bounding the stopband, matches well before and after bonding and the second mode is only slightly offset. The third mode has shifted toward the stopband significantly such that it appears like only a small mound on the side of the second mode in the bonded spectrum. This shift has resulted in the remaining modes being displaced so that they are completely unmatched with the modes of the unbonded spectrum. Whereas the second mode was displaced by approximately 0.05 nm towards the stopband, the third and fourth modes moved 0.35 nm and 0.38 nm respectively. This change in the modes significantly altered the shape of the spectrum before and after bonding.

The Fabry-Perot modes, those modes away from the stopband, remained mostly unchanged in the spectra before and after die bonding. Aside from being shifted, the shape and magnitude of these modes did not change very much. The shifting of these modes owes to the change in the Bragg modes around the stopband. The modes immediately surrounding the stopband changed

significantly enough in the bonded lasers compared with the unbonded lasers that some spectra seemed to have been modified considerably. The altering of the modes' position as well as their separation, caused what appear to be changes in the modes further away. In fact, the Fabry-Perot modes did not deviate much after bonding compared with before. There were cases where Bragg modes seemed to disappear after bonding or shift such that they became satellite bumps of other modes.

The separation of the modes immediately surrounding the stopband were measured for each device before and after die bonding. In particular, the space between the peaks of the stopband bounding modes on either side and the first two modes moving away from the stopband were measured from the spectra before and after bonding. These data demonstrated that, owing to the bonding, the modes surrounding the stopband were altered, however the data were scattered and no general pattern or relationship was found. Figure 9.6 shows the percentage change before and after bonding in the separation between the first and second modes below the stopband for each device. Evidently the data were widely distributed. The bonding caused the modes to shift such that the separation increased by as much as 33% for one device while the separation decreased by 23% for another device. In addition, there was no correlation in these data to show a difference between p-up and p-down mounted devices. The measurement of the stopband width did not show an absolute trend either. Only 3 of the 21 devices had increased stopbands and 11 decreased, yet 7 were unchanged. For those devices that did not have a change in the stopband width there were still changes in the spacing of the surrounding Bragg modes.

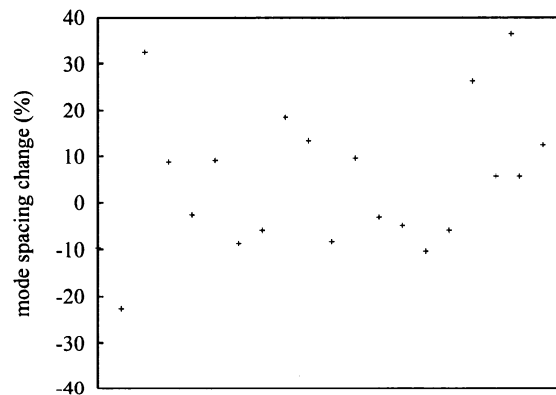

Fig. 9.6 Scatter plot to show the percentage change before and after bonding in the separation between the first and second modes below the stopband for each device.

9.3.3 Lasing Mode Flipping

For 3 of the 21 lasers, the lasing mode flipped from one side of the stopband to the other after die bonding. Two of them flipped from below to above the stopband while one did the opposite. Figure 9.7 shows bonded and unbonded spectra of an example of one of these devices. Before bonding the lasing mode was below the stopband and after the device was bonded the lasing mode shifted to above the stopband. Two of the devices for which the lasing mode flipped upon die bonding were mounted p-up while one of them, the device in Fig. 9.7, was bonded p-down. The shape of the unbonded and bonded spectra in Fig. 9.7 are very similar except for the slight misalignment of the modes below the stopband.

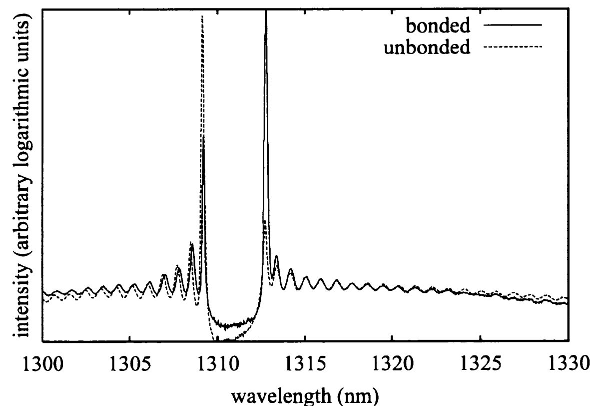

Fig. 9.7 Unbonded (dashed) and bonded (solid) spectra of a p-down mounted diode laser at 20 mA. The lasing mode was below the stopband in the unbonded spectrum and above the stopband in the bonded spectrum. The bonded spectrum was shifted to align with the unbonded spectrum for comparison.

9.4 Discussion

9.4.1 Bonding Strain

When the diode laser chips were die bonded, thermal strain was introduced into the semiconductor material owing to the difference in coefficients of thermal expansion (CTE) of the materials and the elevated curing temperature. While the diode laser chip, epoxy paste, and chip carrier were curing at a raised temperature they were strain-free. Upon cooling to room temperature, or slightly higher at the operating temperature, the materials contracted. The InP-based laser chip, having a lower CTE than the Cu chip carrier, was compressed as the chips and carrier cooled. It would be expected that for p-up mounted devices, the substrate material might provide some strain relief. P-down mounted devices should then be more susceptible to the effects of bonding strain since the active region is

almost directly in contact with the epoxy and carrier which are causing the strain in the chip. The spectral data did not particularly support this since the changes were so scattered. The shifts in the modes and the changes in the stopband width did not demonstrate a clear difference between the p-up and p-down bonded devices. Both cases showed positive and negative variations in modal spacing and stopband width.

Degree of polarization measurements of the facets did not yield any consistent information about the bonding strain since many of the p-down chips were bonded with an overhang. Instead, a finite element method (FEM) model was used to simulate the thermal strain in the chips. This was done to get an order of magnitude estimate of the upper range of strain. The FEM model was a three-dimensional elastic model with linear tetrahedral elements. This model was kept simple in that the entire interface between the bottom of the laser chip and the top of the chip carrier were in contact with a layer of epoxy. That is, it gave an approximation to an ideal die bond without voids or overhanging. The values in Table 3.1 were used as input parameters. The dimensions of the InP chip were $120 \times 260 \times 300\ \mu m^3$. The FEM simulation used the difference in thermal expansion coefficients and a temperature decrease of 225 °C to estimate the thermal strain. No relaxation was assumed in the materials. From the FEM model the maximum ε_{zz} strain, according to the orientation of Fig. 2.1, following a line along the length of the chip that was centred in the middle horizontally and near the bottom vertically was found to be approximately 0.2%. This corresponds to a maximum stress of about 50 MPa in InP. It is likely that the epoxy layer might actually undergo some stress relaxation in real bonds but this was not included in the model. These stress and strain values are therefore estimated upper limits.

9.4.2 Strained Grating

The observed effects on the spectra before and after die bonding were essentially confined to the Bragg modes. The Fabry-Perot modes, while shifted, were not significantly affected by the bonding. This indicates that the changes in the spectra were a result of changes in the grating itself. Strain in diode laser materials can affect the laser spectrum in a number of ways. Strain, by definition, changes the physical dimensions of the chip thereby altering the pitch of the *in situ* diffraction grating. Also, strain alters the refractive index of materials via the photoelastic effect and gain in active layers. Changes in these parameters are observable in the shape of the spectra. When the index and gain in a distributed feedback laser are altered it is expected that the coupling of the forward and backward travelling ways would be affected. The coupling coefficient κ is frequently measured using the stopband width (below threshold).[73] A change in the stopband therefore indicates a change in the coupling of the grating (the amount of feedback per unit length). The true stopband width is equal to 2κ

whereas the spacing of the two modes on either side of the stopband, which was how the stopband was measured in this work, depends on κL. Since L changed by less than 0.2%, according to the FEM model, L does not account for the up to 4.9% change in the stopband width observed. The modification of the stopband must therefore be largely due to a change in the coupling coefficient, κ.

The photoelastic effect owing to the bonding strain can be computed from the modelled stress values since the change in relative dielectric impermeability tensor B_{ij} is expressed as

$$\Delta B_{ij} = \pi_{ijkl}\sigma_{kl} \tag{9.1}$$

where π_{ijkl} are the piezo-optical coefficients and σ_{kl} are the stress components [18]. The changes in refractive indices Δn_{ii} are calculated from the changes in relative dielectric impermeabilities in InP by

$$\Delta n_{ii} \approx -\frac{1}{2} n_{oi}^{3} \Delta B_{ii} \tag{9.2}$$

For the strain estimated from the finite element model at the bottom of the chip, changes in the refractive index of the order of up to 10^{-3} could be expected in the InP chip. Since the gain is connected to the refractive index by the Kramers-Kronig relations any change in refractive index would be accompanied by a change in the gain. In a DFB laser the coupling coefficient is calculated in terms of the periodic difference in high and low index sections, Δn, and the accompanying difference in gain in these sections, Δg:

$$\kappa = \frac{\pi \Delta n}{\lambda} + i\frac{\Delta g}{2} \tag{9.3}$$

Changes in the gain and index along the length of the grating would result in changes in the index and gain differences in the periodic high and low index parts of the grating. Because of non-uniform bonding, the index and gain could have been perturbed along the length of the laser because of overhang and possibly voids. This would affect the overall coupling of the grating and, hence, change the coupling coefficient.

If strains of the magnitude estimated in the FEM model modified the grating then the grating pitch could be altered. A change in grating spacing owing to die bonding would alter the Bragg wavelength. The grating spacing Λ is related to the Bragg wavelength λ_B by:

$$\Lambda = \frac{m\lambda_B}{2n_{eff}} \tag{9.4}$$

If the grating spacing changed by 0.2% then the Bragg wavelength could shift by approximately a couple of nm for a first order grating in a 1.31 μm device. It was

not possible to isolate and measure this Bragg wavelength shift because of the thermal shift in the bonded versus the unbonded laser spectrum.

The observed shifting of modes are a result of the changes in the grating owing to the bonding strain. In cases where modes seemed to appear or disappear after bonding it really amounts to a shifting of Bragg modes. The Fabry-Perot modes remain essentially unchanged in bonding but shifting Bragg modes result in a sort of interference with the Fabry-Perot modes. In cases where destructive interference occurs, a mode may seem to disappear. As well, a shifting of Bragg modes could result in the appearance of new modes after bonding as the Bragg and Fabry-Perot modes constructively interfere.[74]

9.4.3 Multiple Phase-Shifted Lasers

The die bonding may have resulted in uneven contact between the laser chip and epoxy and this would create zones of uneven strains. The change in refractive indices and possibly grating pitch along different parts of the grating in a laser would cause varied coupling along the length of the laser. DFB lasers with axially-varying parameters have been modelled.[75] Agrawal explored a dual-pitch DFB laser structure where part of the laser was composed of a section of a slightly different pitch than elsewhere in the grating. This type of device was explained as being like two coupled conventional DFB lasers. There could be similarities with an unevenly die bonded device as the grating pitch would be changed along part of the length of the device owing to the strain.

Other workers have reported unexplained differences in the measured stopband width compared with what was theoretically predicted. Whiteaway *et al.*, [76], described how measurements of stopbands in $\lambda/4$ phase-shifted DFB lasers were different from what they had expected from their model. This variation was attributed, in their work, to non-uniformities in the devices although there was no definitive explanation for the variations. The devices in question were mounted p-side down onto a copper chip carrier. Perhaps bonding strain played a role with these devices in the observed differences between model and measurement. As it has been shown, bonding does affect the spectrum of DFB lasers.

Multiple phase-shifted lasers are designed to provide a relatively uniform intensity along the length of a DFB laser by introducing several phase shifts in the grating. If a laser were bonded non-uniformly it might experience a similar effect in that the non-uniform bonding strain could introduce gradual phase shifts along the length of a laser grating. Facet phase, the position of the DFB grating with respect to the cleaved facet, has been shown to affect the spectra of DFB lasers.[77] Strain owing to die bonding could slightly alter the facet phase if the length of the grating tooth at the facet was changed by bonding strain. This could alter the modes surrounding the stopband and change the spectrum slightly. The observations in the unbonded versus bonded spectra measured in this experiment

may be a result of a combination of these effects. The causes mentioned here for why the spectra may have changed are not independent of one another. Because of this it is not possible to isolate the reasons why the die bonding resulted in spectral changes. There were observed effects owing to die bonding and some possible individual explanations have been proposed here as to how bonding strain could cause these, even if they were not isolated in reality.

9.4.4 Mode Flipping

Of the 21 devices in the experiment, 3 showed flipping of the lasing mode across the stopband, as was shown in Fig. 9.7. In the case of Fig. 9.7, the lasing mode flipped from below to above the stopband. The majority of the devices exhibited a lasing mode above the stopband both before and after bonding which is consistent with the design of a gain-coupled laser, since it typically exhibits a spectrum with a lasing mode above the stopband.

To understand better how die bonding could have resulted in lasing mode flipping, a DFB spectral model was used to simulate the effect of bonding strain on the grating pitch of a laser. To do this, the spectra of an unbonded device were used to fit to the DFB model and then a perturbation that simulated the effect of bonding strain was applied to the grating in the model. This model was a probability-amplitude transfer-matrix model for distributed feedback laser structures.[78] The model was written by Gordon B. Morrison and was altered by him to permit the introduction of a perturbation in the grating spacing for the work explained here. The model fits to the spectra of DFB lasers to extract device parameters and understand spectral features. The model has been shown to fit to DFB spectra very effectively and predict device parameters well, such as facet phase.[77][79] The model fits to sub-threshold spectral data and matches both front and back facet spectra. In Fig. 9.8 are the spectra from a device that was mounted p-up for both the unbonded and bonded cases. From the figure it is clear that the lasing mode flipped from above to below the stopband. The die bonding altered the device sufficiently that it caused the mode to flip across the stopband.

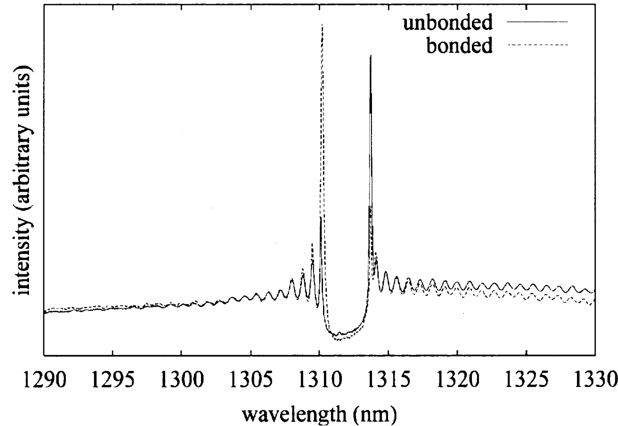

Fig. 9.8 Unbonded (solid) and bonded (dashed) spectra of a p-up mounted diode laser at 21.5 mA. The lasing mode is above the stopband in the unbonded spectrum and below the stopband in the bonded spectrum. The bonded spectrum was shifted in order to align with the unbonded spectrum for comparison.

The DFB spectral model was fit to the below threshold spectra from the front and back of the device before bonding. In Figs. 9.9(a) and 9.9(b) are plots of the below threshold spectra for the front facet and back facet spectra respectively. In these figures the solid line is the spectrum measured with the OSA and the dashed line is the spectrum modelled using the probability-amplitude transfer-matrix model. To perform a spectral fit like this, a large number of laser parameters were adjusted until a best fit laser model was obtained. From the figure it is clear that the fit was fairly good for the front and back facet spectra. The depth of the stopband in the model for the front facet spectrum was somewhat deeper than what was measured, but otherwise the modelled spectra reproduced the modal features fairly well. In performing this fit, the DFB model code determined a number of unknown parameters for the device before it was bonded. With this information the effect of bonding strain could be introduced into the model to see its effect on the spectrum. The DFB model can show the spectra of the device at an arbitrarily set gain. By increasing the gain to near threshold from the below threshold fit, the output spectrum was found to be very similar to the measured above threshold spectrum of the unbonded laser, as will be shown later.

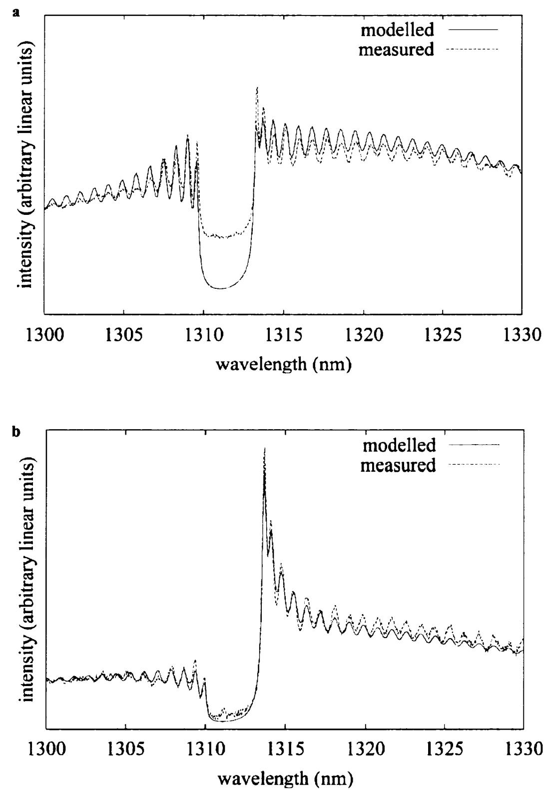

Fig. 9.9 Results of fitting the laser spectra from the device in Fig. 9.8 with the probability-amplitude transfer-matrix distributed feedback laser model. The measured (dashed) and modelled (solid) below threshold spectra are shown for the front (a) and back (b) facet spectra.

The finite element method model described earlier in this chapter was used to estimate the strain at the top of the bonded chip (since this device was bonded p-up). The FEM model was a simplification since it assumed a uniform layer of epoxy at the bottom of the chip which is unlikely. From the FEM model, the ε_{zz} strain, using the orientation of Fig. 2.1, following a line along the length of the chip where the grating would be was extracted and is shown in Fig. 9.10. This plot shows that the grating would be subject to varying amounts of strain along its length. Owing to the compressive strain at the bottom of the chip, from the Cu carrier which contracts a greater amount upon a decrease in temperature, the top of the chip exhibited tensile (positive) strain. This has been observed in a number of devices using DOP measurements. For a chip that is bonded to a carrier with a higher coefficient of thermal expansion, the bottom is compressed during cooling and the top of the chip is stretched as the chip undergoes a limited amount of flexing. The FEM model predicted a varying strain along the length of the grating owing to this flexing.

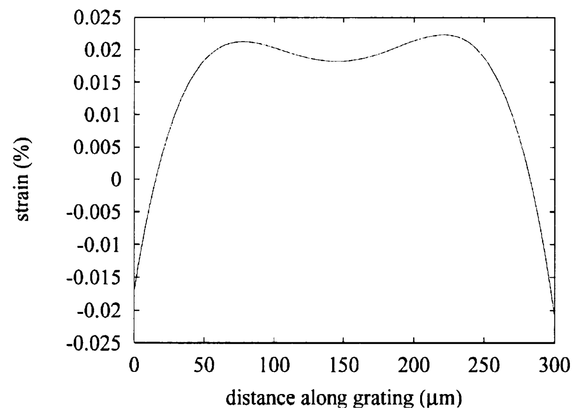

Fig. 9.10 The ε_{zz} strain along the length of the grating owing to die bonding, determined using a finite element method model.

Using this modelled strain information, the DFB spectral model was altered. The strain would affect the grating in two ways, by changing the grating pitch and by altering the refractive indices in the material via the photoelastic effect. These index changes were calculated from the FEM model and were estimated to be a maximum of around $\Delta n \approx 7\times10^{-5}$ which is less significant than the change of the grating pitch. The DFB spectral model was set up so that a perturbation of the grating spacing could be imposed on the model device. This perturbation was a proportional change in the length of the segments of the grating. Using the strain information determined by the FEM model, as shown in Fig. 9.10, a perturbation of the grating spacing proportional to the strain along the length of the grating was imposed on the DFB model of the unbonded laser. When the gain was increased in the model the lasing mode flipped to below the stopband as the gain reached near threshold. The strain values along the grating in the FEM model were only estimates from a simple model. However, the effect that was observed experimentally was reproduced using the model. The lasing mode, in the model without the perturbation, was above the stopband and, in the model with the perturbation, it was below the stopband. This was observed in the spectra of the device which were measured before and after bonding. This is shown in Fig. 9.11 which has the modelled spectrum of the unperturbed model as a solid line and the perturbed model as a dashed line. Note the similarities between the measured and modelled spectra for the unbonded (unperturbed grating) and bonded (perturbed grating) in Figs. 9.8 and 9.11. The lasing mode has flipped in the bonded case and in the model with the perturbed grating. Looking at the perturbation, it only required a very slight strain to cause this flipping, for this device. The maximum strain along the line in the FEM model was less than 0.025% yet this was enough to cause a significant and distinct change in the modelled spectrum.

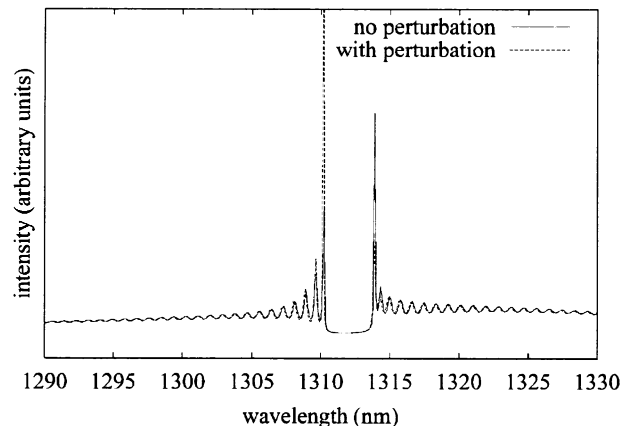

Fig. 9.11 Modelled front facet spectra near threshold for the cases with (dashed) and without (solid) an imposed perturbation of the grating that simulated the effects of bonding. Without a change in the grating spacing, the lasing mode was above the stopband, like the unbonded spectrum in Fig. 9.8. With the perturbation the lasing mode flipped to below the stopband, like the bonded spectrum in Fig. 9.8.

The measured spectra have shown clear evidence that die bonding affects distributed feedback lasers. This modelling confirms that it is an alteration of the grating (spacing and possibly refractive indices) owing to the bonding strain that is the cause of the mode flipping. Since this was a gain-coupled laser the situation is likely somewhat more complicated in that the gain in the grating would have been affected by the strain as well. However, the perturbation in the model was simply a change in the grating spacing and it seems to have accounted sufficiently for the change caused by the bonding in the real device.

9.5 Summary

The die mounting of gain-coupled distributed feedback diode lasers has been shown to affect the output spectra of these devices. Spectra were measured of 21 diode lasers before and after bonding and it was found that the spectra were modified owing to the die mounting. The stopband width was altered in a number of devices. Since the stopband width is directly proportional to the coupling coefficient in distributed feedback lasers, the strain owing to die bonding showed an effect on the coupling of the devices' gratings. The Bragg modes surrounding the stopband were altered by the die bonding. There were significant shifts of some modes in some devices and these led to differences in the before and after spectra. It was found in some cases that the lasing mode flipped across the stopband upon bonding. Using a probability-amplitude transfer-matrix model, it was shown that the inclusion of a perturbation in the grating spacing can result in flipping of the lasing mode across the stopband which matches with measured spectra.

CHAPTER 10 - CONCLUSION

10.1 Introduction

This thesis documented the research work into the die bonding of diode lasers conducted by the author as part of his Ph.D. studies. It was organized into the ten chapters presented, with the intention that it serve as a useful reference. This final chapter is a summary of the work reported in the thesis. In Section 10.2 is a chapter by chapter review of the research done and documented here. In Section 10.3 are some ideas for future work that would be interesting to do in the area of diode laser die bonding.

10.2 Review of Work

Die bonding is an important part of the production of diode lasers but it generally has not received as much attention in the literature as the other procedures involved in producing diode lasers. This may be partly because the bulk of research into die bonding seems to be conducted within companies rather than universities or other public research centres. The outcome of this is that research results sometimes remain proprietary. The organization of this thesis was partly meant for it to be a review of the published work.

In Chapter 1 a synopsis of the thesis was laid out. Chapter 2 provided a review of general elasticity. The chapter then described the use of polarization-resolved photoluminescence as a means of making strain-related measurements on diode lasers. In addition, some details of the experimental system used to make such measurements were described.

Chapter 3 was a review of diode laser bonding. It was explained how chips adhere to carriers using some sort of adhesive, such as solder. The importance of wetting by the adhesive was discussed along with the metallizations used with diode lasers. The different types of solders, alloys and their properties were considered; hard versus soft for example. Finally, a table was presented to gather in one place a list of materials relevant to die bonding and some of their material properties.

In Chapter 4 a study into the effect of the cooling rate on the die bonding of diode lasers was described. It was found that measurable differences existed between die bonds which were cooled rapidly or slowly from the solder reflow. Some of the parameters examine were the strain, the thermal impedance, the surface structure of the solder, and the cross-sectional structure and composition of the joint.

Chapter 5 was a look into pre-deposited solder and a few experiments were documented there. The first two considered the effect of reflow time and the effect of reflow temperature on die bonds using carriers which were pre-deposited with solder. The experiments failed to show a difference in strain (viewed as DOP and ROP maps) owing to die bonding between either the three reflow times

or between the three reflow temperatures. However, it was found that the DOP and ROP patterns were interesting and warranted further investigation. This provided motivation for the finite element model that fits to DOP and ROP data, as explained in Chapter 7. Another experiment was detailed in Chapter 5 dealing with the effect of the carrier metallization scheme. It was not found, however, that DOP and ROP data could be used to determine any difference between the three metallization schemes.

In Chapter 6, a study looking into the stress relaxation in die bonds was outlined. The work indirectly observed the stress relaxation in the solder by measuring the DOP at the facets of diode lasers. Using these DOP maps, from lasers which were involved in an accelerated aging experiment, it was found that bonding stress relaxed over a time scale in the hundreds of hours.

Chapters 7 and 8 described a finite element model that iteratively fits to DOP and ROP data from the facets of diode lasers. In Chapter 7 the finite element method was explained in general terms and a derivation specific to the elasticity model used was provided. It was explained how the DOP and ROP data were used to fit a FEM model and extract components of stress and strain from the model. Various improvements to the computational efficiency of the model were also documented in the chapter. A range of examples of FEM fits were provided in Chapter 8. These included some of the chips shown in Chapter 5, which had relatively complex DOP and ROP patterns. In addition, an analysis of the effect of bonding strain on the guiding of a ridge waveguide was detailed in the chapter. Finally, it was explained how DOP measurements, coupled with the FEM fitting routine can be used to detect large voids in the solder of die bonds.

In Chapter 9 an experiment to determine the effect of die bonding strain on distributed feedback lasers was explained. It was found that the spectra of DFB lasers can change upon die bonding. The width of the stopband as well as the modes surrounding the stopband can change after bonding. In addition, it was observed that the lasing mode can flip to the other side of the stopband after bonding. Using a sophisticated model that fits to DFB spectra, it was found that with the imposition of a perturbation in the grating spacing that approximates the effect of bonding strain, the lasing mode can be made to flip across the stopband.

10.3 Suggestions for Future Work

There were a number of things related to this thesis which either were not completed for various reasons, or which would be interesting to explore in the future. An example of this would be the pre-deposited solder experiments in Chapter 5. It would have been desirable to have some samples cross-sectioned and analyzed using scanning electron microscopy and Auger spectroscopy to determine the differences in the solder structure and solder composition. Since it was only possible to take DOP and ROP data, the experiments were limited. Materials related information would have been beneficial. On the same topic, the

fast versus slow cool experiment would have benefited from a greater number of samples and a larger number of cross sectioned devices. Further analysis of more cross sectioned samples would yield more information about the bonds.

It would be interesting to do a complete study of stress relaxation. This would include using a number of different aging temperatures and currents to understand their effect on the relaxation. It could be useful, in studying the long term aging of die bonds, to determine an empirical Arrhenius type of relationship for the rate of change of strain with respect to temperature. As well, some cross sectional analysis at different points in time could conceivably yield more information about the plastic strain in the solder. In addition research that looked at the stress relaxation during aging of epoxy bonded devices could be interesting.

The DOP and ROP measurements provide information related to the bonding strain owing to the CTE mismatch in materials and the difference between the freezing and operating temperatures. In principle, it could be possible to use DOP data, along with the fitting code, to determine the freezing point of the solder (which is the temperature of zero bonding strain). By determining the strain over a range of temperatures it could be possible to extrapolate to the zero strain point. This would give the freezing temperature of the solder and may help indicate the composition. An initial experiment was carried out as a proof of concept, although it was not documented in this thesis. A full analysis would require many more measurements and more sophisticated analysis.

The finite element method fitting code was used with state of the art personal computers as of the writing of this thesis. Even with a significant amount of optimization the limitations of the available computer power limited the possibility of some enhancements. For example, it would be interesting to simultaneously fit to the DOP and ROP data from the front facet and back facet. In addition if DOP measurements could be made of the top of the chip and the bottom of the chip then a more complete FEM model could be determined. Even with the code fully optimized, doing such a multiple fit was not possible using a present-day personal computer. This will change in the future as more memory and processing speed become available. Alternatively, the code could be ported to a system that uses large parallel-connected computers, which are used in many research environments.

The study of distributed feedback lasers would benefit if back facet spectra could be obtained for p-down mounted devices. If a carrier could be designed to enable the back spectra to be measured with a device in such a mounting it would provide greater information for the DFB fitting. The work on the effect of bonding on the spectra of DFB's was the final work done for this thesis. It just touched on what could make for an interesting project itself. For example, it would be interesting to try and predict the changes in the spectra from the bonding. Making DOP measurements on a number of faces of the laser chip and using the FEM fitting code as described in the previous paragraph with a more

powerful computer system could enable the DFB model to predict the spectral changes.

10.4 Summary

This chapter concludes the thesis. It provided an overview of the work presented within the thesis as well as some suggestions for work that could be done in the future. The overall goal of this research was to understand better the die bonding of diode lasers. This has largely been completed and a number of findings were published in respected journals. The project was conducted within the Department of Engineering Physics and the work was somewhat more "engineering" than "physics" research. The die bonding of diode lasers may not be as glamorous as the physics of the laser design but, as has hopefully been shown in this thesis, die bonding is still an important part of producing a functioning diode laser module and it poses a number of difficulties and challenges itself.

REFERENCES

Chapter 1

[1] G.R. Blackwell, *The Electronic Packaging Handbook*, CRC Press (2000)

[2] R. Beach, W.J. Benett, B.L. Freitas, D. Mundinger, B.J. Comaskey, R.W. Solarz, & M.A. Emanuel, "Modular Microchannel Cooled Heatsinks for High Average Power Laser Diode Arrays," IEEE Jour. Quantum Electron. **28**(4), 966-976 (1992)

[3] R. Diehl (editor), *High Power Diode Lasers*, Springer (2000)

[4] D. Lisak, D.T. Cassidy, & A.H. Moore, Bonding stress and reliability of high power GaAs-based lasers, IEEE Trans. Comps., Pack., Manuf. Technol. **24**, 92-98 (2001)

[5] V. Swaminathan, L.A. Koszi, & M.W. Focht, "Effect of Macroscopic Stress on Accelerated Aging of GaInAsP Channeled Substrate Buried Heterostructure Lasers," J. Appl. Phys. **66**, 1849-1854 (1989)

[6] T. Hayakawa, N. Miyauchi, S. Yamamoto, H. Hayashi, S. Yano, & T. Hijikata, "Improved lifetimes of (GaAl)As visible (740 nm) lasers by reducing bonding stress," Appl. Phys. Lett. **42**(2), 23-24 (1983)

[7] R. L. Hartman & A.R. Hartman, "Strain-induced degradation of GaAs injection lasers," Appl. Phys. Lett. **23**(3) 147-149 (1973)

[8] N.K. Dutta & D.C. Craft, "Effect of stress on the polarization of stimulated emission from injection lasers," J. Appl. Phys. **56**(1), 65-70 (1984)

[9] C.S. Adams & D.T. Cassidy, "Effects stress on threshold, wavelength, and polarization of the output of InGaAsP semiconductor diode lasers," J. Appl. Phys. **64**(12) 6631-6638 (1988)

[10] N.K. Dutta, "Effect of uniaxial stress on optical gain in semiconductors," J. Appl. Phys, **55**(2), 285-288 (1984)

[11] J. Yang & D.T. Cassidy, "Strain measurement and estimation of photoelastic effects and strain-induced optical gain change in ridge waveguide lasers," J. Appl. Phys. 77(7), 3382-3387 (1995)

[12] P.D. Colbourne, & D.T. Cassidy, "Imaging of Stresses in GaAs Diode Lasers Using Polarization-Resolved Photoluminescence," IEEE Jour. Quantum Electron. **29**(1), 62-68 (1993)

[13] M. Fukuda, O. Fujita, & G. Iwane, "Failure Modes of InGaAsP/InP Lasers Due to Adhesives," IEEE Trans. Comp. Packag. Hybrid. Manufac. Technol. 7(2) 202-206 (1984)

[14] M.A. Fritz, & D.T. Cassidy, "Cooling Rate in Diode Laser Bonding," accepted for publication (June 13, 2003) in IEEE Trans. Comp. Packag. Technol.

[15] M.A. Fritz, & D.T. Cassidy, "Extraction of Bonding Strain Data in Diode Lasers from Polarization-Resolved Photoluminescence Measurements," accepted for publication (Sept. 12, 2003) in Microelectronics Reliability

[16] M.A. Fritz, & D.T. Cassidy, "Photoelastic Effect from Die Bonding of Diode Lasers," accepted for publication (Sept. 24, 2003) in Applied Optics

Chapter 2

[17] P.C. Chou, & N.J. Pagano, *Elasticity: Tensor, Dyadic, and Engineering Approaches*, Dover Publications (1992)

[18] J.F. Nye, *Physical Properties of Crystals*, Clarendon Press, Oxford (1957)

[19] R.N. Bhargava, & M.I. Nathan, "Stress Dependence of Photoluminescence in GaAs," Phys. Rev. **161**(3), 695-698 (1967)

[20] S.L. Chuang, *Physics of Optoelectronic Devices*, Wiley-Interscience (1995)

[21] D.T. Cassidy, S.K.K. Lam, B. Lakshmi, & D.M.Bruce, "Strain mapping by measurement of degree of polarization of photoluminescence," submitted for publication

[22] P.D. Colbourne, Ph.D. Thesis, McMaster University (1992)

Chapter 3

[23] G.S. Selvaduray, "Die Bond Materials and Bonding Mechanisms in Microelectronic Packaging," Thin Solid Films **153**, 431-445 (1987)

[24] D.H. Kaelble, *Physical Chemistry of Adhesion*, Wiley-Interscience (1971)

[25] M.M. Schwartz, *Fundamentals of Soldering*, ASM Metals Handbook #8 126; Welding, Brazing, and Soldering (1993)

[26] C.O. Smith, *The Science of Engineering Materials*, 3rd Ed. Prentice-Hall (1969)

[27] W.J. Plumbridge, "Solders in Electronics," Jour. Mat. Sci. **31**, 2501-2514 (1996)

[28] T.B. Massalski (editor), *Binary Alloy Phase Diagrams*, ASM, Metals Park Ohio (1986)

[29] G.S. Matijasevic, C.C. Lee, & C.Y. Wang, "Au-Sn alloy phase diagram and properties related to its use as a bonding medium," Thin Solid Films **223**, 276-287 (1993)

[30] A.R. Mickelson, N.R. Basavanhally, & Y-C. Lee, *Optoelectronic Packaging*, John Wiley & Sons (1997)

[31] C.Y. Wang, C.C. Lee, "A Eutectic Bonding Technology at a Temperature Below the Eutectic Point" Proc. 42nd Electronic Components Conference, 502-507 (1992)

[32] C.H. Lee, K.L. Tai, D.D. Bacon, C. Doherty, A. Katz, Y.M. Wong, & E. Lane, "Bonding of InP Laser-Diodes by Au-Sn Solder and Tungsten-Based Barrier Metallization Schemes," Semicond. Sci. Technol. **9** 379-386 (1994)

[33] Charles V. Cagle, *Handbook of Adhesive Bonding*, McGraw-Hill (1973)

[34] K. Suzuki, O. Suzuki, & M. Komagata, "Conductive Adhesive Materials for Lead Solder Replacement," IEEE Trans. Comp. Pack. Manu. Tech. **21**(2), 252-258 (1998)

[35] J.A. King, *Materials Handbook for Hybrid Microelectronics*, Artech House (1988)

[36] S.A. Merritt, P.J.S. Heim, S. H. Cho, & M. Dagenais "Controlled Solder Interdiffusion for High Power Semiconductor Laser Diode Die Bonding" IEEE Comp. Packag. Manufac. Technol. **20**(2), 141-145 (1997)

[37] S. Adachi, *Physical Properties of III-V Semiconductor Compounds*, John Wiley & Sons (1992)

[38] J.F. Lynch, C.G. Ruderer, & W.H. Duckworth, *Engineering Properties of Selected Ceramic Materials*, American Ceramic Society, Columbus, Ohio (1966)

[39] J. Emsley, *The Elements,* 3rd Ed., Clarendon Press, Oxford (1998)

[40] F.G. Yost, M.M. Karnowsky, W.D. Drotning, & J.H. Gieske, "Thermal Expansion and Elastic Properties of High Gold-Tin Alloys," Metallurgical Transactions A 21A 1885-1889 (1990)

[41] EPO-TEK H20E Data Sheet, Epoxy Technology Inc., Billerica, MA, U.S.A.

Chapter 4

[42] B. Chandran, W.F. Schmidt, & M.H. Gordon, "A Novel Bonding Technique to Bond CTE Mismatched Devices," IEEE Electronic Components and Technology Conference, 1151-1158 (1996)

[43] C.C. Lee, C.Y. Wang, & G.S. Matijasevic, "A New Bonding Technology Using Gold and Tin Multilayer Composite Structures," IEEE Trans. Comp., Hybrids, and Manufac. Technol., **14**(2), 407-412 (1991)

[44] T.L. Paoli, "A New Technique for Measuring the Thermal Impedance of Junction Lasers," IEEE J. Quantum Electron., **11**(7), 498-503 (1975)

[45] P.R. Bevington & D.K Robinson, *Data Reduction and Error Analysis for the Physical Sciences*, McGraw-Hill (1992)

[46] J. Sigelko, S. Choi, K.N. Subramanian, J.P. Lucas, & T.R. Bieler, "Effect of Cooling Rate on Microstructure and Mechanical Properties of Eutectic Sn-Ag Solder Joints with and without Intentionally Incorporated Cu_6Sn_5 Reinforcements," J. Electron. Mat., **28**(11), 1186-1188 (1999)

[47] H. Okamoto & T.B. Massalski, *Phase Diagrams of Binary Gold Alloys*, ASM International (1987)

[48] *Metals Handbook*, 10th Ed. Vol. 2, Properties and Selection: Nonferrous Alloys and Special Purpose Materials (1990)

Chapter 5

[49] D.C. Abbott, R.M. Brook, N. McLelland, & J.S. Wiley, "Palladium as a Lead Finish for Surface Mount Integrated Circuit Packages," IEEE Trans. Comp. Hybrid. Manufac. Technol. **14**(3) 567-572 (1991)

[50] A. Fekecs, Bookham Technology, private communication

Chapter 6

[51] E. Baker, "Stress Relaxation in Tin-Lead Solders," Mat. Sci. Eng. **38**, 241-247 (1979)

[52] E. Baker, "Some Effects of Temperature on Material Properties and Device Reliability," IEEE Trans. Part. Hybrid. and Packag. **8**(4), 4-14 (1972)

[53] S. Vaynman, G. Ghosh, & M.E. Fine, "Effects of Palladium and Solder Aging on Mechanical and Fatigue of Tin-Lead Eutectic Solder" J. Elec. Mat. **27**(11), 1223-1228 (1998)

[54] D. Tribula, D. Grivas, & J.W. Morris Jr., "Stress Relaxation in 60Sn-40Pb Solder Joints," J. Elec. Mat, **17**(5), 387-390 (1988)

[55] R.W. Rohde, & J.C. Swearengen, "Deformation Modeling Applied to Stress Relaxation of Four Solder Alloys," J. Eng. Mat. Tech., **102** 207-214 (1980)

[56] E.P. Unksov, *An Engineering Theory of Plasticity*, Butterworth, London (1961)

[57] P.D. Colbourne, & D.T. Cassidy, "Bonding Stress Measurements from the Degree of Polarization of Facet Emission of AlGaAs Superluminescent Diodes," IEEE J.Quantum Electron. **27**(4), 914-920 (1993)

Chapter 7

[58] K.H. Huebner, E.A. Thornton, & T.G. Byrom, *The Finite Element Method for Engineers*, 3rd Ed., John Wiley & Sons Inc. (1995)

[59] O.C. Zienkiewicz & R.L. Taylor, *The Finite Element Method*, 5th Ed., Butterworth-Heinemann (2000)

[60] H. Si, Tetgen 1.0 User Manual, Zhejiang University, PRC (2001)

[61] D. Stolle, *An Introduction to the Finite Element Method*, McMaster University Custom Courseware (2000)

[62] D.W. Marquardt, "An algorithm for least-squares estimation of nonlinear parameters," J. Soc. Indust. Appl. Math. II(2), 431-441 (1963)

[63] W.H Press, S.A. Teulolsky, W.T. Vetterling, & B.P. Flannery, *Numerical Recipes in Fortran* 2nd Ed, Cambridge University Press (1992)

Chapter 8

[64] N. Suzuki & K. Tada, "Elastooptic Properties of InP," Jpn. J, Appl. Phys. **22**, 441-445 (1983)

[65] EMIS Datareviews Series No. 6, *Properties of Indium Phosphide*, Inspec (1991)

[66] G.R. Hadley & R.E. Smith, "Full-Vector Waveguide Modeling Using an Iterative Finite-Difference Method with Transparent Boundary Conditions," Jour. Light. Tech. **13**(3), 465-469 (1995)

[67] J. Yang, & D.T. Cassidy, "Correlation between strain fields on the facet and along the cavity in semiconductor diode lasers," J. Appl. Phys. 77(8), 3762-3765 (1995)

[68] R. Maceijko, J.M. Glinski, A. Champagne, J. Berger, & L. Samson, "Photoelastic Effects on the Emission Patterns of InGaAsP Ridge-Waveguide Lasers," IEEE Jour. Quantum Electron. **25**(4), 651-660 (1989)

[69] R. Maceijko, A. Golebiowski, A. Champagne, & J.M. Glinski, "Selective TE-TM Mode Pumping Efficiencies for Ridge-Waveguide Lasers in Presence of Stress," IEEE Jour. Quantum Electron. **29**(1), 51-60 (1993)

[70] Q.Z. Liu, F. Deng, L.S. Yu, Z.F. Guan, S.A. Pappert, P.K.L. Yu, S.S. Lau, J.M. Redwing, & T.F. Kuech, "Photoelastic waveguides and the controlled introduction of strain in III-V semiconductors by means of thin film technology," J. Appl. Phys. **78**(1), 236-244 (1995)

Chapter 9

[71] H. Ghafouri-Shiraz & B.S.K. Lo, *Distributed Feedback Laser Diodes - Principles and Physical Modelling*, John Wiley & Sons (1996)

[72] G.Morthier & P.Vankwikelberge, *Handbook of Distributed Feedback Laser Diodes*, Artech House Inc. (1997)

[73] H. Kogelnik & C.V. Shank, "Coupled-Wave Theory of Distributed Feedback Lasers," J. Appl. Phys. **43**(5) 2327-2335 (1967)

[74] G.B. Morrison, Ph.D. Thesis, McMaster University, 2002

[75] G.P. Agrawal, & A.H. Bobeck, "Modeling of Distributed Feedback Semiconductor Lasers with Axially-Varying Parameters," IEEE J. Quantum Electron. **24**(12) 2407-2414 (1988)

[76] J.E.A. Whiteaway, G.H.B. Thompson, A.J. Coller, & C.J. Armistead, "The Design and Assessment of $\lambda/4$ Phase-shifted DFB Laser Structures," IEEE J. Quantum Electron. **25**(6) 1261-1279 (1989)

[77] G.B. Morrison, & D.T. Cassidy, "Improving the Ability of a Distributed-Feedback Laser Transfer-Matrix Model to Fit to Spectra from Distributed-Feedback Lasers" IEEE Photon. Technol. Lett. **12**(7), 769-770 (2000)

[78] G.B. Morrison, & D.T. Cassidy, "A Probability-Amplitude Transfer Matrix Model for Distributed-Feedback Laser Structures," IEEE J. Quantum. Electron. **36**(6), 633-640 (2000)

[79] G.B. Morrison, & D.T. Cassidy, "Extraction of Gain Parameters for Truncated-Well Gain-Coupled DFB Lasers," IEEE Photon. Technol. Lett. **11**(12) 1566-1568 (1999)

INDEX

A

adhesion layer 19
atomic force microscope (AFM) 29
Auger electron spectroscopy 29
automated die bonder 41

B

barrier layer 19
body force vector 70
Bragg modes 106
Bragg wavelength 113

C

calibration constants 8
chip 1
chip carrier 21
Cholesky decomposition 77
coefficient of thermal expansion (CTE) 23
compatibility 72
completeness 72
compliance tensor 6
constant strain tetrahedron 71
contact layer 19
convergence 72
cooling rate 25
coupling coefficient 113

D

degree of polarization (DOP) 7
device aging 55
die 1
die bonding 1
die bond 13
die bonder 25
die collet 25
dielectric impermeability tensor 90
diffusion barrier 19
dislocation glide 59
displacement vector 67
distributed feedback laser (DFB) 102

E

elasto-optical coefficients 91
element 64
element displacement field 67
engineering shear strain 6
epoxy 21
eutectic 17

F

Fabry-Perot modes 106
far field 95
finite element method 64
fitting 73
flux 16
forming gas 16

G

global stiffness matrix 71
grating 112
grating perturbation 118
grating pitch 113

H

hard solder 17
homologous temperature 60

I

initial force vector 70
intermetallic compound 18
interpolation functions 66
isotropic 7

K

kinematic matrix 68

L

lasing mode flipping 111
linear operator matrix 68
linear superposition 73
liquidus 17
local stiffness matrix 71
lumped force method 72

M

Marquardt algorithm 74
material properties 23
mathematical shear strain 6
mesh generation 65
metallization strain 81
metallizations 19
minimum potential energy principle 69
mode 106
modulus tensor 7

N
natural coordinates 66
node 64

O
optical spectrum analyzer (OSA) 103
orthotropic 7

P
p-down 14
p-up 14
packaging 1
Paoli method 28
phase-shifted lasers 114
photoelastic effect 90
photoelastic tensor 90
piezo-optical coefficients 91
Poisson's ratio 7
potential energy 69
pre-deposited solder 19
preform solder 19
probability-amplitude
  transfer-matrix model 115

R
reflow profile 42
reflow temperature 41
reflow time 41
rotated degree of polarization (ROP) 8
rotating polarizer 10

S
shearing test machine 30
soft solder 17
solder ball 49
solidus 17
stiffness matrix 170
stopband 104
strain 6
strain-interpolation matrix 68
strain energy 104
stress 5
stress relaxation 55
submount 21
surface tension 14
surface traction vector 70

V
vacuum pickup 49
variational approach 64
voids 98
volume coordinates 66

W
wetting 16
wetting angle 15
work of displacement 69

Y
Young's modulus 7